



UNIVERSITÀ DEGLI STUDI DI TORINO
SCUOLA DI SCIENZE DELLA NATURA
DIPARTIMENTO DI FISICA

Characterization of gaseous detectors at the CERN Gamma Irradiation Facility: GEM performance in presence of high background radiation

Antonio Bianchi

Relatore:

Prof. Ferruccio Balestra

Correlatori:

Dr. Roberto Guida

Dr. Beatrice Mandelli



Contents

Contents	ii
Introduction	1
1 Motivation of ageing tests for High Luminosity-LHC	3
1.1 Muon detectors systems at the Large Hadron Collider	3
1.2 Muon systems upgrade in view of High Luminosity LHC	4
1.3 Current application of Gas Electron Multiplier at CERN	8
2 CERN Gamma Irradiation Facility (GIF++)	9
2.1 Overview of CERN GIF++	9
2.2 The ^{137}Cs irradiator and the gamma irradiation field	11
2.2.1 Duty cycle of irradiator	13
2.3 Beam	16
2.4 Services at CERN GIF++	17
2.4.1 DIP service	19
2.4.2 Beam trigger	21
3 Research and development on GEM detectors for HL-LHC	34
3.1 Gaseous ionization detectors: working principles	34
3.2 Triple-GEM performance in presence of high background radiation . .	37
3.3 Principle of operation of triple-GEM and SWPCs	39
3.4 Experimental setup for R&D at GIF++	43
3.5 Characterization of triple-GEM and SWPCs for ageing test	54
3.6 Performance of detectors at GIF++	60
3.6.1 Interaction of photons with matter	60
3.6.2 Measurements under irradiation of ^{137}Cs source	60
3.6.3 Gas chromatography for gas mixture	66

4	Simulation of triple-GEM detector with different gas mixtures	68
4.1	Implementation of triple-GEM detector with ANSYS and GARFIELD	68
4.1.1	Geometry of triple-GEM detector with ANSYS	69
4.1.2	Calculation of electric field in a GEM detector with GARFIELD	74
4.2	Simulation of electron avalanches in GEM detectors	75
4.2.1	Major processes in electron and gas mixture collisions	75
4.2.2	Simulation of single-GEM and triple-GEM	79
4.3	Choice of the gas mixture for triple-GEM	81
4.4	Effects of pollutants in the gas mixture	84
	Conclusions	91
A	Experimental setup at Gamma Irradiation Facility in details	93
B	Construction and characterization of SWPCs	96
C	Gas chromatography	101
	Bibliography	105

Introduction

The Large Hadron Collider (LHC) at the European Organization for Nuclear Research (CERN) has established a new particle physics program concerning precise measurements of the Standard Model as well as searches of new physics. Muon detection is an efficient tool to recognize interesting physics events over the high background rate expected at the LHC. The muon systems at the CERN experiments are very large apparatus of the order of several thousands square meters and are based on gaseous ionization detectors.

The upgrade of the LHC accelerator performance (HL-LHC), scheduled for 2025, sets new important challenges to all muon systems. The goal of the LHC detector upgrades is to maintain or even improve the current performance in term of efficiency, resolution and background rejection. Indeed the high luminosity in LHC will raise the background radiation involving several effects, as for example high instantaneous particle rate and high radiation damage. Therefore additional studies on the gaseous detectors are required to ensure good conditions for long-term operation in view of HL-LHC. Chapter 1 outlines the foreseen different upgrades for muon detectors and their motivation.

Several studies on gaseous detectors are nowadays performed at the CERN Gamma Irradiation Facility (GIF++), which is a facility where a beam of high-energy charged particles (mainly muons) is combined with a ^{137}Cs source emitting gamma photons. Currently more than ten setups are under test in the facility, including five different gaseous detector technologies. Chapter 2 presents an overview of the GIF++ as well as the characterization and installation of the beam trigger system for the facility.

In presence of a high background radiation, as at GIF++, ageing effects might manifest in gaseous detectors through a progressive degradation of performance. Several processes in gas mixture can lead to ageing phenomena, such as dissociation, polymerization and etching, which can drastically decrease the lifetime of detectors as well

as unwanted pollutants, due to the outgassing of materials, can contaminate the gas mixture. The R&D studies, discussed in chapter 3, are focused on the performance of a triple gas electron multiplier (triple-GEM detector) under gas recirculation in presence of high background radiation at GIF++. Several studies of stability and reliability are on going for different gas mixtures and recirculation fractions.

In a first step, the triple-GEM detector and two single wire proportional chambers, used to monitor the stability of the gas mixture in the recirculation system, have been characterized in laboratory. A data acquisition system was developed to monitor the performance of triple-GEM detector and the environmental parameters of the system, which might affect the detector response. The detectors have been installed at GIF++ and the triple-GEM has been irradiated with the ^{137}Cs source.

In parallel, the effects of common pollutants have been simulated with GARFIELD++ software to evaluate the performance of triple-GEM detector with different gas mixtures (Ar/CO_2 and $\text{Ar}/\text{CO}_2/\text{CF}_4$ in different compositions). Indeed the availability of simulation allows to calculate extensively drift and diffusion properties of gas mixtures in presence of pollutants. Chapter 4 is dedicated to the simulation and its results.

Chapter 1

Motivation of ageing tests for High Luminosity-LHC

1.1 Muon detectors systems at the Large Hadron Collider

The Large Hadron Collider (LHC) at CERN is a 27-km ring of superconducting magnets with accelerating structures to boost the energy of the particles along the way. During most of the year, each proton beam at full intensity consists of 2808 bunches per beam with 10^{11} protons per bunch, while for the remaining time heavy-ions (mainly lead ions) are accelerated. In case of protons, collisions happen 40 million times per second in order to provide proton-proton collisions at a centre-of-mass energy of 14 TeV. Four main experiments have been designed and built for LHC: ATLAS, CMS, ALICE and LHCb. The experiments have different physics programs, detector designs and technologies: ATLAS and CMS are general-purpose experiments capable of exploring all aspects of the LHC program, ALICE is focused on studies of heavy-ion collisions while LHCb is focused on the b-quarks physics.

The design requirements of the LHC detectors are stringent. Most of them need high granularity to reduce the influence of overlapping events, a fast and radiation-tolerant electronics for a proper data acquisition, a good identification of charged particle and momentum resolution over a wide range. The detectors at the LHC experiments can be mainly divided into three main groups:

- inner detectors, which are located close to the collision point and allow tracking of charged particles, momentum measurements and reconstruction of vertices;
- hadronic and electromagnetic calorimeters, which measure the energy of hadrons, electrons, photons;

- muon systems, for the measurement of directions and momenta of muons, which escape from the calorimeters.

The muon detectors systems are usually made up of gaseous ionization detectors. Since muons penetrate more deeply in the matter than most of the other particles, this type of detectors is usually placed in the outermost layers of experiments, covering large areas of them. The muon detectors are essential at LHC because they form a clean and unambiguous signature of several events of interest and they can also provide the trigger for the detection of useful data. Indeed the muon systems have essentially three functions: muon identification, momentum measurements of them and triggering. The LHC gaseous detectors can be divided in two categories: detectors used for precise measurements of muon tracks and the others for triggering on muons. Although the four experiments at LHC have completely different goals, they are similar in their reliance on muon detection and triggering [1]. The current application of muon chambers and the upgrades, foreseen in the future, will be present in the next paragraphs.

1.2 Muon systems upgrade in view of High Luminosity LHC

The luminosity of a collider, as LHC, is one of the most important parameters, because it is proportional to the number of events of interest that can be produced during collisions. The instantaneous luminosity L can be expressed as:

$$L = \gamma \frac{n_b N^2 f_{rev}}{4\pi \beta^* \varepsilon_n} R \quad (1.1)$$

where γ is the proton beam energy in unit of rest mass, n_b the number of bunches in the machine, N is the bunch population, f_{rev} is the revolution frequency, β^* is the beam beta function (focal length) at the collision point, ε_n is the transverse normalized emittance and R is the luminosity geometrical reduction factor.

For physics purposes, the more relevant parameter is the integrated luminosity, which is the instantaneous luminosity integrated over time and is measured in barn ($1 \text{ b} = 10^{-28} \text{ m}^2$) [2].

The collider experiments try to maximize the integrated luminosity to have more available data. All the hadron colliders in the world have produced so far a total integrated luminosity of 10 fb^{-1} [2], while LHC will achieve an integrated luminosity equal to about 300 fb^{-1} by 2023. The run period, foreseen since 2025, is the High

Luminosity LHC (HL-LHC) phase, where the goal is to achieve an integrated luminosity of 3000 fb^{-1} . Indeed the high-luminosity upgrade of the machine foresees to collect ten times more data than the initial design, in 10-12 years.

In view of the HL-LHC program, the goal of the detector upgrades in all experiments is to maintain or even improve the present performance in term of efficiency, resolution and background rejection.

The increasing of luminosity in LHC will raise the background radiation, increasing the effect of the following mechanisms:

- Higher instantaneous particle rate could affect the detector efficiency and reduce the trigger performance;
- The radiation damage could shorten the lifetime of muon detectors due to accumulative effects, which lead to ageing processes.

The increasing of the instantaneous particle rate will cause a high pileup on the detectors: at the nominal luminosity of the HL-LHC, the average number of interactions in a single crossing will be about 140. The forward region ($|\eta| \geq 1.0$) is especially challenging for the muon systems. Indeed the particle rate on the muon chambers can reach 10 kHz/cm^2 or higher in experiments like ATLAS or CMS. For this reason, the high particle rate could cause higher detector occupancies and the increase of fake trigger rate.

As shown in figure 1.1, an analysis of 2012 data in ATLAS demonstrated that approximately 90% of the muon triggers at high luminosity in the end-caps are fake, due to the presence of low energy particles, mainly protons [3].

Furthermore radiation damages, due to the high background radiation, could induce a progressive degradation in the materials of detectors and in the on-board electronics. Figure 1.2 shows the distribution of absorbed dose in the CMS cavern for an integrated luminosity of 3000 fb^{-1} .

In the forward region of CMS, the accumulated dose can reach about 1 C/cm^2 in the next high-luminosity LHC upgrade. Indeed the annual dose per year during HL-LHC will be similar to the total integrated dose from the beginning of LHC operation. Radiation levels for the muon system are much lower than for the inner detectors or calorimeters. However the future upgrade of LHC requires additional studies also on muon systems performance under some conditions. Indeed the muon triggering and identification will continue to be the major discovery drivers at LHC. For these *R&D*

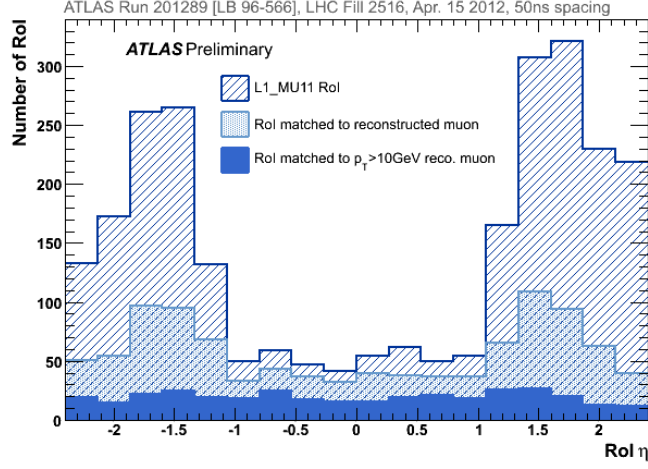


Figure 1.1: Number of muon triggers in ATLAS depending on the Region of Interest η (RoI η). The number of muon triggers is matched to an offline reconstructed distribution of muons with $p_t > 3 \text{ GeV}$ and $p_t > 10 \text{ GeV}$. The Level 1 Muon Trigger in ATLAS is based on RPC and TGC hits and the analysis of 2012 data demonstrates the increase of muon fake triggers at high luminosity, especially in the forward regions [3].

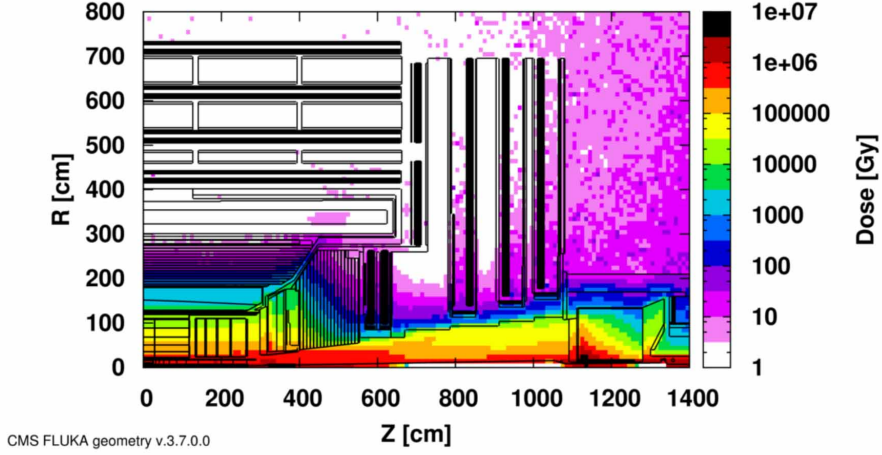


Figure 1.2: Distribution of absorbed dose in the CMS cavern for an integrated luminosity of 3000 fb^{-1} [4].

studies, a dedicated facility has been built at CERN, where the expected background is simulated, to expose the muon detector in a shorter time period (1-2 years) to a radiation level equivalent to the full HL-LHC period [4].

The major muon detectors upgrades are foreseen for ATLAS, CMS and ALICE. In ATLAS, the New Small Wheel (NSW) is proposed to replace the existing Muon Small Wheel (MSW). The NSW should ensure efficient tracking with position res-

olution of about $100 \mu m$ at high $|\eta|$. For these purposes, the NSW will have two chambers technologies, based on gaseous ionization detectors: small-strip Thin Gap Chambers (sTGC) for triggering and Micromegas detectors for precision tracking [5]. In CMS, the muon system in the region $1.5 \leq |\eta| \leq 2.4$ consists currently of four stations of Cathode Strip Chambers (CSC) for the triggering and the tracking. For the future upgrades, additional chambers with higher rate capability have been proposed, as shown in figure 1.3. Gas Electron Multiplier (GEM detectors) will be added in station 2, while in the last two stations low-resistivity Resistive Plate Chambers (RPC) has been proposed given their high timing resolution (i.e. capacity to reduce the effect of background radiation on the trigger). The insertion of triple-GEM detectors in region $GE2/1$ (station 2) is already scheduled in the next long shutdown period of LHC (2018-2019) [6, 7]. Moreover the implementation of a GEM station near the new end-cap calorimeters (about $|\eta| = 3$) is taken into account for Run 3 [7].

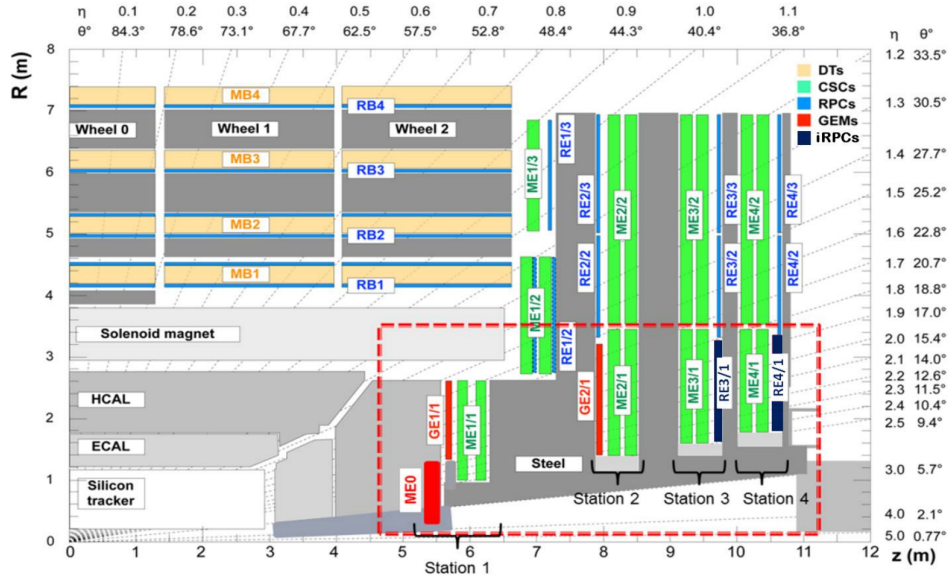


Figure 1.3: Future upgrade of CMS experiment with the use of GEM detectors in the muon system.

In ALICE, GEM detectors will be installed during the next long shutdown (LS2) in the Time Project Chamber (TPC), which is the main tracking system in the central barrel of the experiment.

In addition to the gaseous detector upgrades for the muon systems, a common topics

for the LHC experiments is related to the gas mixtures, in particular to reduce the emissions of greenhouse gases and for cost saving. Indeed some of gas mixtures for the muon detection at LHC involve the presence of one or more greenhouse gas.

Each experiment at LHC requires huge volumes of gas, involving often greenhouse gases. For only the RPC detectors, ATLAS and CMS need 15 m^3 of gas mixture. Currently the three greenhouse gases with the highest impact are: tetrafluoroethane ($C_2H_2F_4$), tetrafluoromethane (CF_4) and sulfur hexafluoride (SF_6). Their global warming potentials (GWP) are higher in comparison with one of carbon dioxide. If the GWP for the carbon oxide is equal to 1, the global warming potential (GWP) for the tetrafluoroethane is 1430 and for the sulfur hexafluoride is even 22200. For example, one of the mixtures used for the GEM detectors is made up of Ar (45%), CO_2 (15%) and CF_4 (40%), whereas for RPC detectors the common mixture is 95.6% of $C_2H_2F_4$, 4.1% of iC_4H_{10} and 0.3% of SF_6 .

1.3 Current application of Gas Electron Multiplier at CERN

The micro-pattern gas detectors (MPGDs) are gaseous detectors with excellent space resolution, high rate capability, good granularity and resistance to radiation damages. Due to these features, the MPGDs are suitable for the charged particle tracking at high-luminosity colliders [8].

The construction of MPGDs exploits generally the photo-lithographic techniques on thin insulating supports. More than twenty different designs of micro-pattern detectors are known, but in general the MPGD structures can be divided in two types:

- GEM: strip and hole-type structures;
- Micromegas: micromesh-based structures.

Nowadays GEM detectors are operational in LHCb, TOTEM and COMPASS experiments. For instance, the COMPASS experiment has commissioned in 2002 a production of $30 \times 30\text{ cm}^2$ triple-GEM detectors for the forward tracker of spectrometer at the Super Proton Synchrotron (SPS), while the innermost region of LHCb muon system is equipped with triple-GEM detectors.

GEM-based detectors find a lot of applications in astrophysics, medical diagnostics and biology, because of their versatility.

Chapter 2

CERN Gamma Irradiation Facility (GIF++)

2.1 Overview of CERN GIF++

The CERN Gamma Irradiation Facility (GIF++) started operation in April 2015 and is a special facility where a beam of high-energy charged particles (mainly muons) is combined with gamma photons from a radioactive source of ^{137}Cs , so studies of performance and stability of the detectors, designed especially for High Luminosity LHC upgrades, can be carried out.

The GIF++ irradiation bunker has a total surface of 100 m^2 divided in two regions: the upstream region has an extension of 30 m^2 and the surface of the downstream region is 70 m^2 . Figure 2.1 shows an inside view of the GIF++ irradiation bunker.



Figure 2.1: Inside view of GIF++ irradiation bunker with the indication of two different regions: upstream and downstream.

Currently (September 2016) more than ten setups are under test in the facility. They include five different gaseous detector technologies:

- Drift Tubes;
- Gas Electron Multiplier;
- Cathode Strip Chambers;
- Micro-Megas;
- Resistive Plate Chambers.

Beyond detector studies, several research groups are testing and validating chambers before the final production and installation on the LHC experiments [4]. The irradiation area is shielded by 1.6 m thick concrete wall. A large access door is made up of two concrete blocks, which can be removed, when needed, to allow an easy installation of large detectors. Also the roof of the bunker can be totally opened for the installation of them. Close to the bunker, there is a two-floor area for hosting the gas system and the electronic services. In addition, a preparation zone with a surface of 80 m² is available for preliminary tests before the installation in the irradiation area. Figure 2.2 shows the external view of the bunker, the preparation zone and the areas for the gas systems and electronic services.



Figure 2.2: External view of GIF++. The preparation zone and the two-floor area for gas-mixing zone and electronic services surround the irradiation bunker [4].

The GIF++ is designed to fulfill the requirements for testing the different types of muon detectors present in the LHC experiments. There is a gas-mixing zone, where all gases needed for the operation of the detectors are essentially available through dedicated primary supply panels. In particular, the most common gases used at GIF++ are: Ar , He , N_2 , CO_2 , SF_6 , CF_4 , iC_4H_{10} , CH_4 , $C_2H_2F_4$.

About fifty gas lines distribute the gas mixture to the irradiation area and the preparation zone; each one includes a supply pipe and a return pipe. A gas analysis system is also present to allow monitoring continuously the flammability level of mixtures containing flammable components and sometimes for measuring the contents of O_2 and H_2O vapour on supply lines and return from the detectors. Furthermore it is possible to analyse the gas mixtures more precisely with a gas chromatograph, which is permanently connected to the gas lines.

2.2 The ^{137}Cs irradiator and the gamma irradiation field

A radioactive source of ^{137}Cs is present in the bunker of the facility. The activity of the source was $13.9\ TBq$ in November 2015 and the energy of primary photons is equal to $662\ keV$. ^{137}Cs is used because the spectrum of primary and scattered photons matches with good approximation the energy spectrum expected for background radiation in LHC. Moreover the thirty years half-life of ^{137}Cs makes the rate of emitted photons stable over the years. The irradiator is a customized version of the model $GI - 02$ developed by the VF company (figure 2.3).

The radioactive source can be moved by a control system from the shielded position to the irradiation position on top of the container. For safety reason, the irradiation position is on the top of the container and the source goes down in the lead container only through the gravity force. In this way, the mechanical system for the movement of the source is really more sure in case of malfunctioning.

The radioactive source in the irradiation position is at $(2.06 \pm 0.01)\ m$ from the floor of building and it is located at the same height of the beam. The wide opening angle of both areas is $\pm 37^\circ$ (shown in figure 2.1) on the horizontal and vertical planes.

Both irradiation windows are equipped with an aluminium angular correction lens for having a uniform flux of gamma photons on a flat surface and depending only

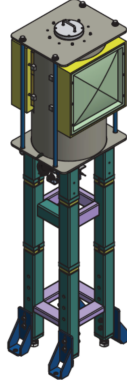


Figure 2.3: Structure of the irradiator at GIF++. The radioactive source of ^{137}Cs has an activity equal to 13.9 TBq . When the source is not in the irradiation position, it is placed inside a lead container [4].

on the distance from the source. This angular correction allows studying the performance of large area detectors even if they are placed far from the source. For each irradiation zone, the gamma flux can be independently modulated using a set of six attenuation lenses that allows an attenuation factor from 1 to $1/46000$. The lenses are made of lead and the corresponding attenuation factors are summarized in table 2.1. This modulation of the intensity of gamma flux allows studying the effects of different background radiations on the detector rate capability [9].

	A	B	C
filter 1	1	1	1
filter 2	10	1.5	2.2
filter 3	100	100	4.6

Table 2.1: Attenuation filter values of the ^{137}Cs source at GIF++. These filters allow decreasing the intensity of the radioactive source. The value 1 means an empty frame, whereas the value 10 refers a decreasing of the intensity by 10 times. It is possible to use only one absorption factor per column (A, B and C), for a total of three filters together

The irradiation field inside the bunker has been simulated and then the dose into the irradiation area has been measured in several positions in order to prove and verify the simulation.

Figure 2.4 shows the simulation of the radiation field in the bunker without any attenuation applied. The dose equivalent rate at 1 m from the source is about 500 mSv/h .

On the left of figure 2.5 the downstream side of irradiator is fully open and the upstream area is shielded with the maximum filter (equal to 46000), while on the right

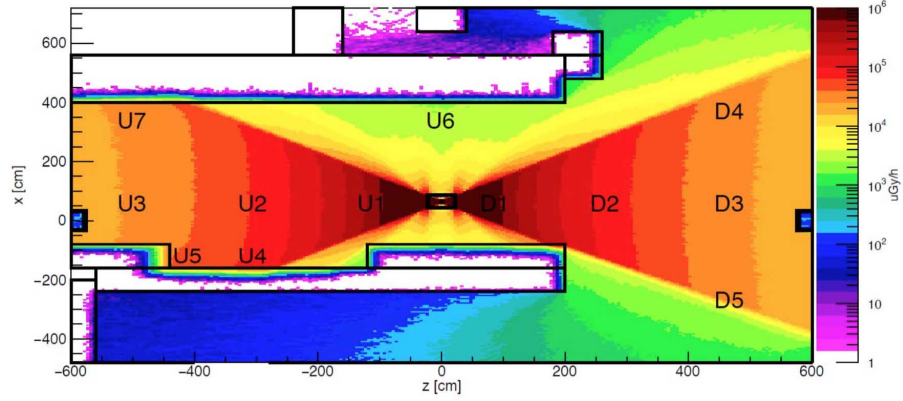


Figure 2.4: Simulation of the radiation field in the GIF++ bunker with upstream filter = 1 and downstream filter = 1 [9].

the situation is opposite. For instance, in figure 2.5 on the left, it is clearly possible to see the presence of scattered radiation with the structure of irradiator and bunker on the upstream region. In any case the radiation is almost a factor 10000 lower than the radiation on the downstream, where the frame is completely open. For this reason, the two areas can be considered independent with good approximation.

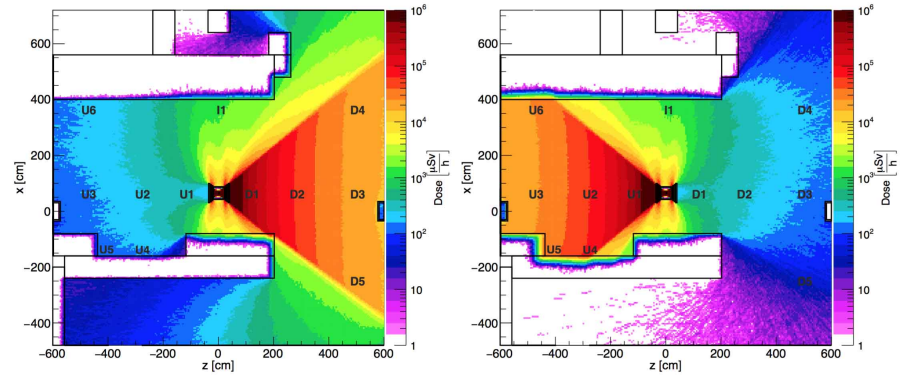


Figure 2.5: On the left, simulation of radiation field in the following settings of irradiator: upstream filter = 46000 and downstream filter = 1. On the right, the situation concerning the attenuation filters is opposite [9].

2.2.1 Duty cycle of irradiator

For safety reasons, two sensors are installed inside the bunker for monitoring continuously the radiation level. The radiation monitoring system, called RAMSES (RA radiation Monitoring System for Environmental and Safety), is used in several

experiments at CERN. The sensors are air-filled plastic ionization chambers for measuring the gamma radiation [10]. Figure 2.6 shows the position of the sensors and one of the two sensors installed inside the bunker.

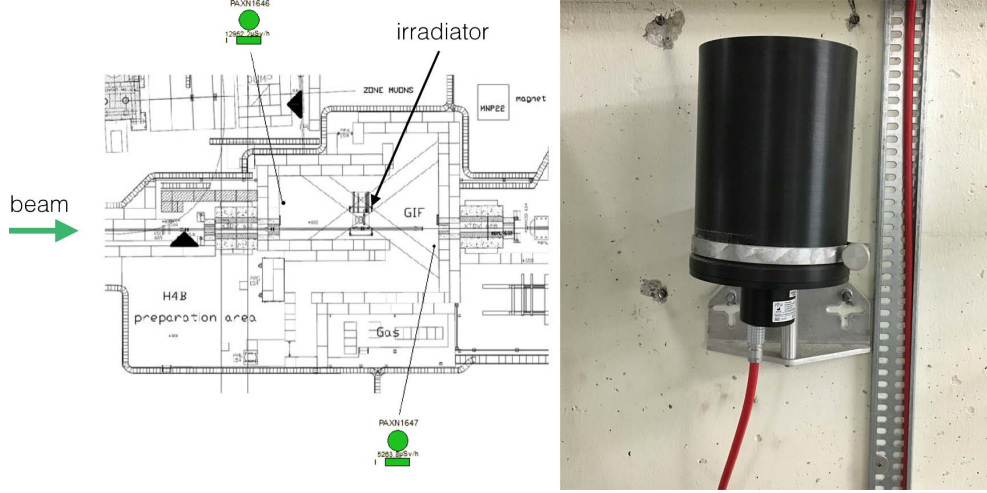


Figure 2.6: On the left, the sketch shows the position of the sensor (PAXN1646) in upstream region and the position of the sensor (PAXN1647) in the downstream area. On the right, there is the photo of an air-filled plastic ionization chamber of RAMSES system for measuring the incoming gamma radiation.

The RAMSES system is installed to fulfill CERN safety requirements. All data of the sensors are acquired by a system of acquisition and control that generate radiation warnings, alarms and potentially operational interlocks.

Moreover the data of the radiation from the RAMSES system can be used to evaluate the duty cycle of the irradiator. The duty cycle is the ratio of how long the source radiates photons in the irradiation area of GIF++ and the total time period. Figure 2.7 shows the irradiation on the upstream and downstream regions, measured by the RAMSES system, from January to July 2016 and in the figure 2.7 the monthly duty cycle of the irradiator is summarized. A threshold of 10^{-4} Sv/h has been selected to evaluate the period when the source is exploited: if the dose equivalent is higher than the threshold, the source is considered in the irradiation position, otherwise it is considered inside the lead container.

The maximum dose equivalent rate measured for upstream and downstream region is different because the distances of sensors from the source are slightly different. In the case of upstream, the distance from the sensor and the center of irradiator is $(6.2 \pm 0.1) \text{ m}$, whereas for the downstream area the distance is $(7.9 \pm 0.1) \text{ m}$. For this reason, the dose equivalent rate measured in upstream region is generally greater than

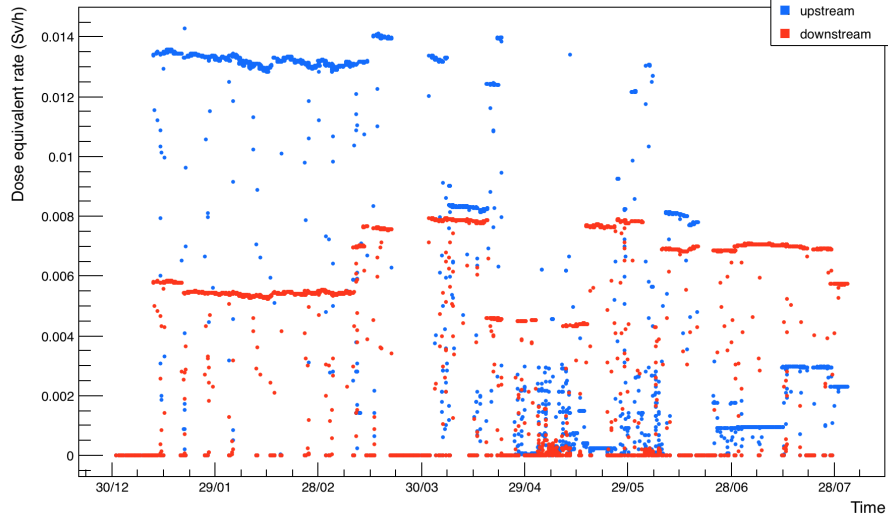


Figure 2.7: Dose equivalent rate in upstream (blue) and downstream (red) region in the bunker area of GIF++ from on 1st January 2016 to 31st July 2016.

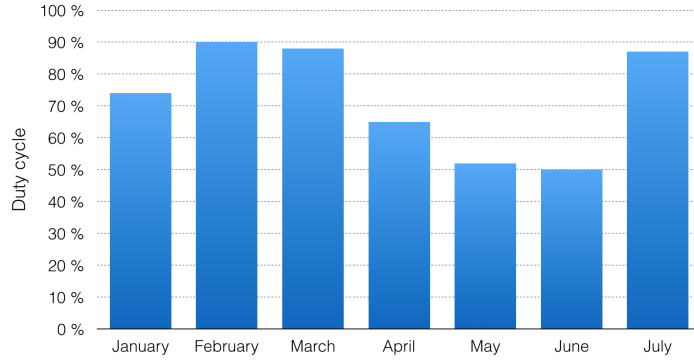


Figure 2.8: Summary about the monthly duty cycle of the irradiator at GIF++.

one in downstream region. Moreover several detectors are present in the area between the ^{137}Cs source and the RAMSES sensors. So the movements of some detectors in the area explain the steps of the dose equivalent rate in figure 2.7.

Finally it is important to underline that users of the facility have decided to concentrate the accesses in the bunker one day per week (usually on Wednesdays) for short intervention on the detectors and tuning of experimental set-up, whereas another day per week (usually on Thursday) is dedicated for filter absorption scans in order to evaluate constantly the performance of detectors. During the beam periods, the requests of access in the bunker are more frequent, for this reason the duty cycle decreases lightly in those periods. In any case, the duty cycle of the irradiator from 1st January 2016 to 31st July 2016 is very good with about 72.4% of the time the source in irradiation position.

Further eight radiation sensors, different from the RAMSES system, are available inside the bunker area for precise measurements of absorbed dose. They can be directly placed in front of the detectors in order to allow continuously monitoring of the accumulated dose in the detector. This system, based on RadFETs (Radiation-sensing Field Effect Transistor), might be really useful when another detector is installed between the irradiator and the detectors under test at any time, otherwise the calculation of accumulation dose could result unrealistic [11].

2.3 Beam

A beam of high-energy charged particles (mainly muons) is available at GIF++ and is used especially for studies of performance during ageing tests. The momentum of the charged particles can range from $10 \text{ GeV}/c$ up to $450 \text{ GeV}/c$, which is the maximum momentum of Super Proton Synchrotron (SPS).

The SPS has a circumference of 6.9 km and can handle different types of particles: protons, antiprotons, electrons, positrons and oxygen nuclei [12]. Secondary beam are produced directly from the impact of the SPS primary beam onto the T2 beryllium target.

Figure 2.9 shows the status of extraction from the ring and the impinging of protons on the targets in the North Area at CERN. The beam is extracted from SPS accelerator and sent to different targets. The GIF++ is placed in the H4 line, which is equipped by target T2. The number of particles (I/E11) sent towards the primary target is expressed in 10^{11} particles per spill. The multiplicity (MUL) is the ratio between the numbers of charged particles detected before and after target: it depends of course on the length of target and on the acceptance of downstream detector. The symmetry (%SYM) of the beam is evaluated and monitored by a system of split foils inside the target box [13].

After the impact of the primary beam on the target, several types of particles are produced. In general the facilities along the H4 line are interested in muons, pions or electrons. A spectrometer of 300 m in length, made up of six dipole magnets with a total bending angle of 42 mrad , is used for the momentum selection. The beam momentum has a precision of maximum $\Delta p/p_{max} = 1.4\%$ [14]. Moreover a complex system of magnets and collimators, called *wobbling station*, is used to bend, focus and optimize the secondary beam. Figure 2.10 shows the beam line from T2 target to

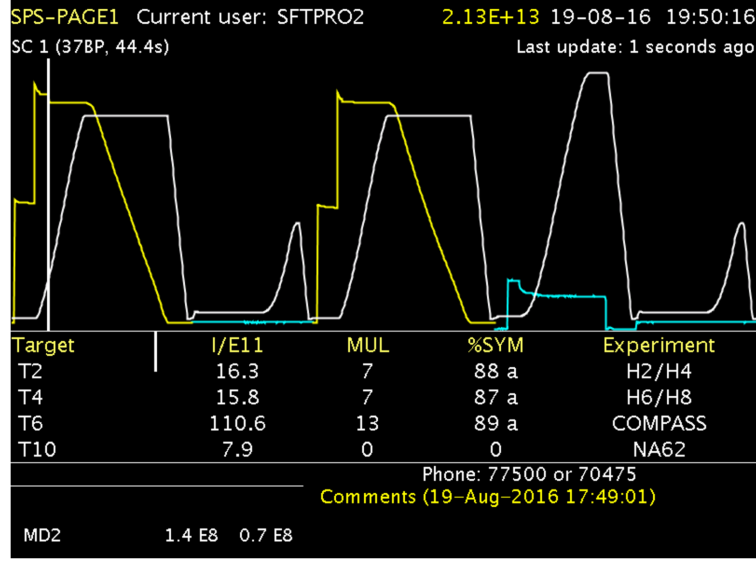


Figure 2.9: The snapshot shows some useful parameters of the extraction from SPS. The yellow and blue curves indicate the intensity of the particles in the SPS machine. The magnetic pulse for the extractions is represented in white. A moving vertical marker shows the present time. All these signals do not have absolute scales because they depend on the SPS operator [13].

GIF++.

The function of dipole magnets (B in the figure 2.10) is to guide the particles through the tunnels towards the experimental areas, as GIF++, and also to introduce dispersion that is necessary for achieving momentum selection. The quadrupoles (Q) focus the beam in order to control the beam size and dispersion along the beam line. Finally the collimators ($COLL$) collimate the beam and sometimes are used for taking out some types of particles. For instance, if one wants a beam with only muons, as the users requests at GIF++, the collimators can take out other different particles from the beam with proper settings [15]. The beam usually delivers a maximum muon flux of about 10^4 muons per spill traversing an area of $10 \times 10 \text{ cm}^2$. The GIF++ facility is main user of the beam line for 6-8 weeks per year.

2.4 Services at CERN GIF++

At the GIF++, several services and infrastructures are available to support the users and facilitate the operation of particle detectors. Among them, the GIF++ provides:

- Availability of real-time data concerning the status of the facility by DIP service;

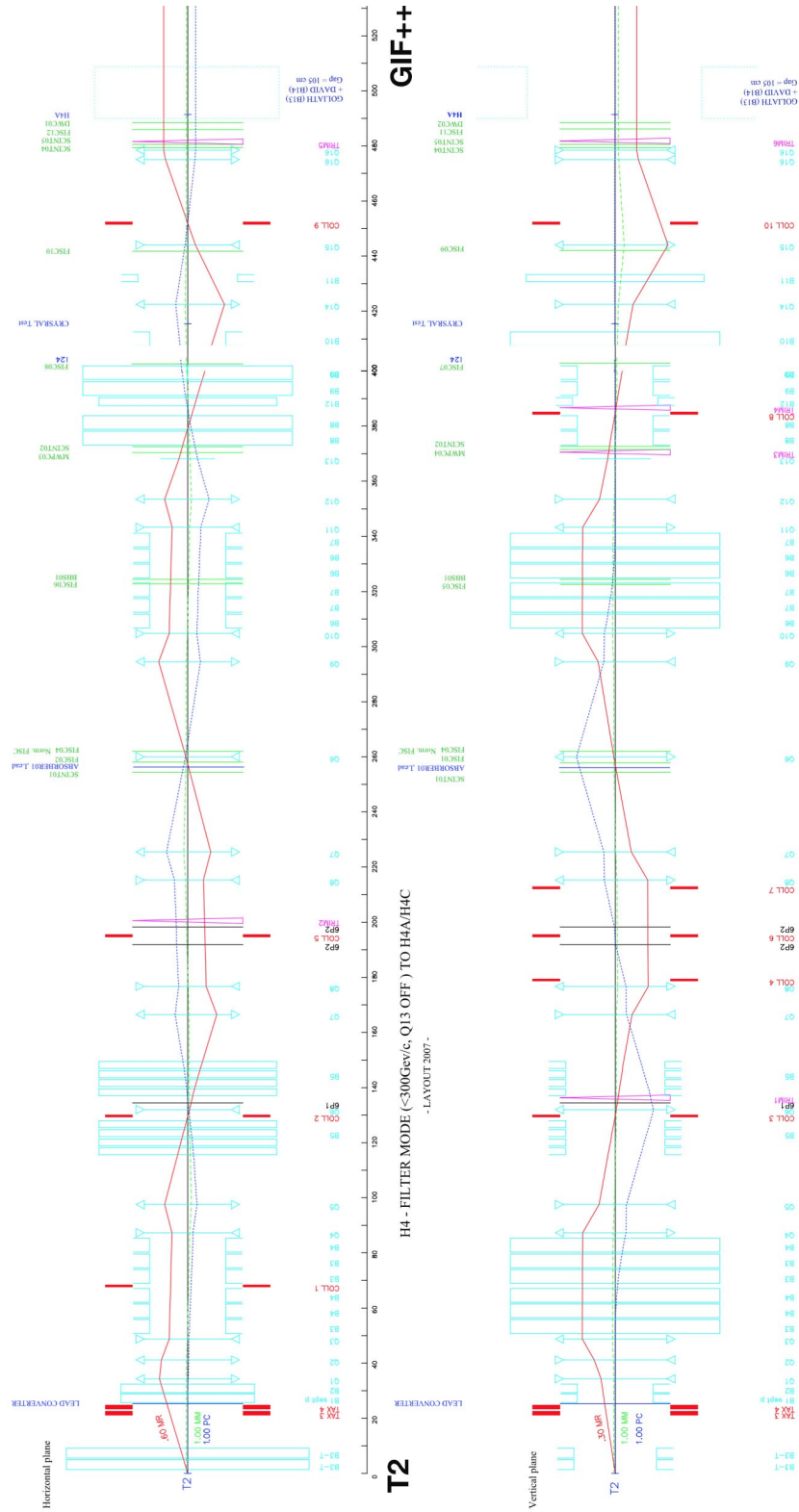


Figure 2.10: The sketch shows the wobbling stations along the H4 beam line from T2 target to GIF++ in the horizontal and vertical view.

- Beam trigger to allow studying the performance, the time and space resolution of detectors under test at GIF++.

2.4.1 DIP service

DIP is an information distribution service, which allows carrying and sharing real-time data among heterogeneous systems [16]. Through this protocol of communication, used also for the experiments of LHC, it is possible to monitor remotely the facility and save all relevant parameters, as irradiator source state, environmental conditions, like temperature and atmospheric pressure inside and outside the bunker area, and the access status in the bunker. Moreover on the DIP platform the real-time composition of gas mixtures in input to the detectors, the pressures of the gas lines and other gas parameters can be easily obtained.

Important components in the DIP architecture are the publishers, for the data publication, and the subscribers, which get the data. In figure 2.11 the structure of DIP is shown.

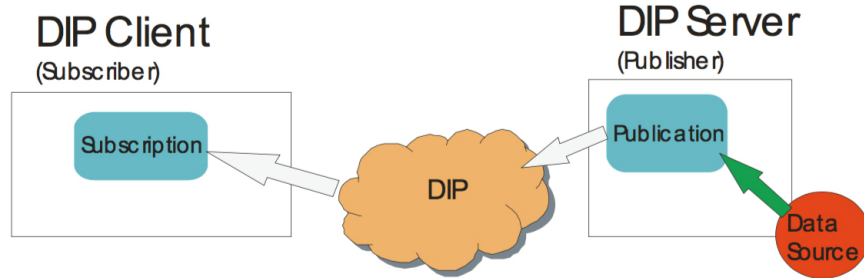


Figure 2.11: The sketch shows the architecture of DIP service, that is made up of a publisher which publish the data of interest and a subscriber to get them

The DIP publisher has full control over data content and timestamp of publication. In figure 2.12, a simple code with only the most important phases for the publication of data is shown. In C++ coding, a publisher has to define a publication with a specific path in the folder *dip/*. For the case of GIF++, the folder *GIFppGPN* is dedicated for all data concerning the facility: that is in the General Purpose Network (GPN)¹, so it is achievable from everyone without specific rights. For the CERN experiments,

¹The Internet network at CERN is divided into Technical Network (TN) and General Purpose Network (GPN). The Technical Network is only dedicated to the experiments, special authorizations for the access are needed and the data transfer rate is about 3 Tbit/s, whereas the General Purpose Network is used for general purposes without any specific protection from external connections inside CERN network and the data transfer rate is about 1 Tbit/s.

a dedicated network (Technical Network) is available. After the definition of the data name (in figure 2.13, the name is *CO2*), the stream of publication is set and the value is published on the DIP platform. Whenever a new value is available, the old value is refreshed with the new one.

```
string pubNameRoot = "dip/GIFFppGPN/gas/";

DipPublication **pub = new DipPublication*[noPubs]();
DipData **pubData = new DipData*[noPubs];

ostringstream oss;
oss << "TGC_CO2";
fieldNames.push_back(oss.str());

pubData[i] = dip->createDipData();
pubData[indexPub]->insert(value_for_publication, fieldNames[i++].c_str());
```

Figure 2.12: Example of DIP publisher in C++ code.

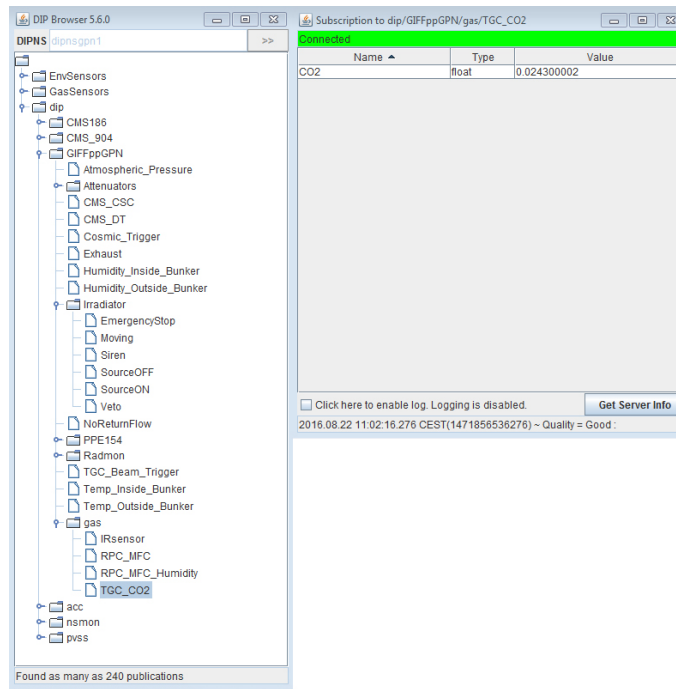


Figure 2.13: On the left, there are all data concerning on the facility GIF++. On the right, the value of *CO₂* (in litres per hour) in the gas mixture for Thin Gap Chambers under test at GIF++.

As it can be seen in the figure 2.13, the most important GIF++ data available on DIP platform are:

- The access status in the bunker area: closed area, access with keys (for safety reason) or free access;
- The status of the source: in the irradiation position (ON) or completely shielded inside the lead container (OFF);
- The absorption filters used in real-time in upstream and downstream positions;
- Environmental parameters, like temperature, humidity and atmosphere pressure inside and outside the bunker;
- Accumulation dose measured by RADMON sensors;
- Composition of gas mixture in input to Resistive Plate Chambers (RPC) and Thin Gap Chambers (TGC);
- Concentration of flammable gases for monitoring if the concentration of them exceeds the threshold, beyond which the mixture might become dangerous. The sensors, used for the concentration measurements, are infrared analysers and evaluate the intensity of infrared light, which is absorbed in presence of some flammable gases, like iC_4H_{10} .

Some of data, available on DIP, are also published in a webpage for a rapid check of facility by the users. Figure 2.14 shows a screenshot of the webpage: <https://test-gif.web.cern.ch>.

2.4.2 Beam trigger

A beam trigger system has been built and installed for providing a trigger signal to the users in order to identify the muons, which pass through the irradiation area, during the beam periods dedicated to GIF++. The system is made up of two scintillators coupled with two photomultipliers (PMT). The signals from the photomultipliers are acquired by a data acquisition system based on NIM standard and provided to the users for their tests.

Figure 2.15 shows the technical drawing of the scintillators and the assembly of the structure of detectors.

The particle, which passes through the scintillator, produces the excitation of atoms and molecules of scintillator and the consequent emission of light. For the detectors, the scintillator is principally made up of polyvinyltoluene (with the name EJ-200 in



Status of source:



Report:

22/08/2016 11:48	Status of source: ON
22/08/2016 11:48	Access mode: CLOSED
22/08/2016 11:48	Temperature inside bunker: 21.1951 degrees
22/08/2016 11:48	Pressure: 974.311 mbar

Atmospheric pressure (mbar):
974.311

Temperature inside bunker (°C):	Temperature outside bunker (°C):
21.1951	22.4836
Humidity inside bunker (%):	Humidity outside bunker (%):
46.5914	44.2127

Figure 2.14: Webpage of GIF++ (<https://test-gif.web.cern.ch>).

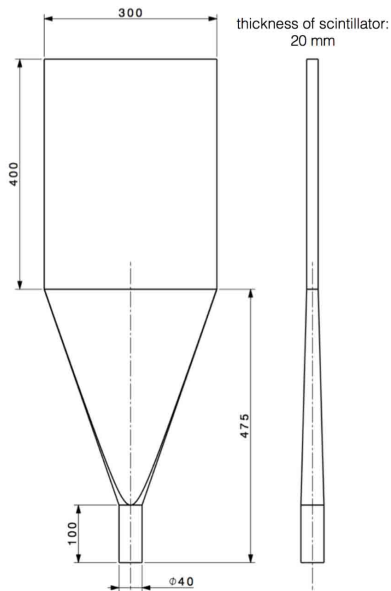


Figure 2.15: On the left, technical drawing of the detector used for the beam trigger system. The distances are in millimeter. A photo of the assembly of scintillators (on the bottom) and light guide (on the top) is present on the right. The optical cement resin (EJ-500) and hardener are used in the interface.

the market) and its emission spectrum has a maximum at about 425 *nm*. The use of plastic scintillator allows exploiting an extremely fast signal with a decay constant of about 3 *ns*. This light is transmitted to the photomultiplier through a light guide with a specific design in order to minimize the loss of light from the scintillator. The light guide works on the principle of internal reflection in order to guide the light to the photomultiplier. The shape of the light guide selected looks like a *fish tail*: it changes slowly from a long rectangular geometry, which is convenient for a good coupling with the scintillator, to a round circular form of the photomultiplier.

The photomultiplier converts light into a measurable electric current; it consists of a cathode made of photosensitive material (called usually photocathode), followed by a dynode string and finally an anode from which the final signal can be taken. All parts are usually assembled in a glass vacuum-sealed tube. The photocathode converts incident light into a current of electrons by the photoelectrons effect:

$$E = h\nu - \phi \quad (2.1)$$

where E is the kinetic energy of emitted electron, $h\nu$ is the energy of the incoming photon (ν is its frequency) and ϕ the work function. The spectral response of photocathode is expressed by the quantum efficiency $\nu(\lambda)$:

$$\nu(\lambda) = \frac{\text{number of photoelectrons released}}{\text{number of incident photons}(\lambda)} \quad (2.2)$$

where λ is the wavelength of the incident photon [17].

The photoelectrons released by photocathode are multiplied along the dynode string. Each of dynodes along the string has a progressive voltage, applied with a voltage divider: the system consists of a chain of resistances chosen such as to provide a well-defined voltage to each of the dynodes. Finally the cascade of electrons is carried and collected at the anode for measuring an electric signal.

In addition of plastic scintillator EJ-200, each detector is made up of a light guide in plexiglass (formula: $(C_5O_2H_8)_n$ and index of reflection: 1.48) and a photomultiplier. For the interface between the scintillator and the light guide a optical cement resin (EJ-500) has been chosen with the adding of a hardener in the ratio 4:1, whereas a silicone optical grease has been applied in the interface between light guide and photomultiplier. An aluminum foil wraps loosely the scintillator and the light guide so as to assure a layer of air in contact with the scintillator. The presence of air in the interface is used to minimize the Brewster angle θ_B .

The Brewster angle is defined as: $\theta_B = \sin^{-1}(\frac{n_{out}}{n_{scint}})$, where n_{scint} is the index of refraction of the scintillator and n_{out} is that of the surrounding medium (in case of air, $n_{out} \approx 1$). At angles smaller than θ_B , partial reflection occurs and the remainder is transmitted. The total internal reflection occurs only if the angle is greater than θ_B , so that the light is turned back into the scintillator. Finally the detector is wrapped by black tape to ensure the lightproof.

Characterization of photomultipliers in laboratory

The specifications of the photomultipliers are unknown because they have been recovered from old detectors out of commission. For this reason, the photomultipliers have been characterized by measurements of the absorbed current depending on the applied voltage. Figure 2.16 shows the current depending on applied voltage for the photomultipliers 1 and 2. The voltage is applied to the detectors by CAEN module A1832. Since the two curves do not have equal trends, it is possible to deduce that the two photomultipliers have different performance; therefore they have different gain at fixed applied voltage.

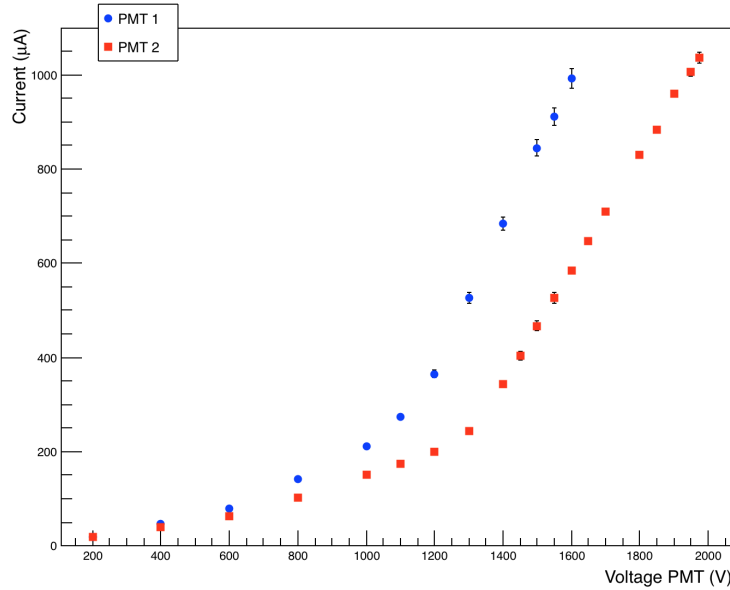


Figure 2.16: Trend of current, absorbed by photomultipliers 1 and 2, depending on applied voltage.

Since the scintillators and light guides for both detectors have the same geometry and the same features, but the photomultipliers have different gains, a characterization and optimization of them was needed. As of now the detector with photomultiplier

1 is called detector 1, whereas the detector 2 has the photomultiplier 2.

At first, the detectors are characterized with measurements of cosmic muons. The working voltages for the photomultipliers have been found by tuning the applied voltage and getting the same amplitude of the average signal for both detectors. Figure 2.17 shows the average signal over 128 samples measured with the oscilloscope TEKTRONIX TDS2024B, used also for all measurements in this paragraph.

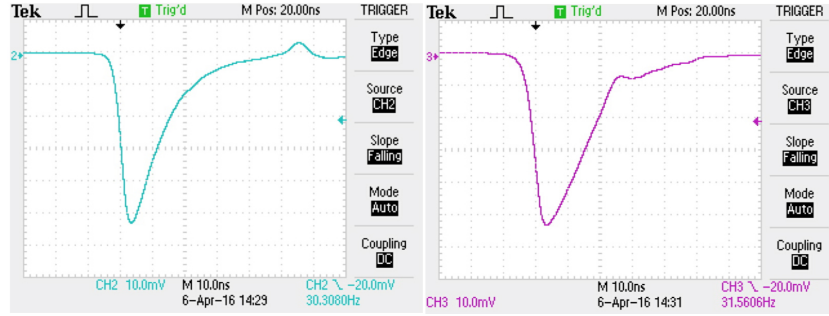


Figure 2.17: Average signal over 128 samples for the detector 1 (in blue) and detector 2 (in purple). Trigger threshold for both signals: -20 mV . The applied voltage to detector 1 is $(1550 \pm 6)\text{ V}$ and to detector 2 is $(1975 \pm 7)\text{ V}$

If the voltage applied for detector 1 is $(1550 \pm 6)\text{ V}$ and for detector 2 is $(1975 \pm 7)\text{ V}$, the amplitude of average signal is equal to $(-52 \pm 2)\text{ mV}$ when the threshold for the trigger of the oscilloscope is set as -20 mV . Therefore the working voltages for detector 1 and detector 2 are respectively selected equal to 1550 V and 1975 V .

For measuring the flux of cosmic muons, the detectors are overlapped with a third smaller detector, taken as reference and called detector 0. The signals of the three detectors are acquired and analyzed by a data acquisition system, based on NIM standard. In particular, the DAQ system is made up of:

- Discriminator LeCroy 4608C: it gives an output only if the input value is greater than a certain threshold value. If this condition is satisfied, the output of discriminator is a logic signal (NIM logic); if not, no response is generated;
- Coincidence unit LeCroy 465: it determines if the signal from detector 1 and detector 2 are in coincidence in time and it generates a logic signal (in this case, time windows is set 25 ns) if *true*, otherwise no output signal. The duration of time windows has been set to 30 ns ;

- Scaler and counter timer CAEN N1145: this unit counts the number of pulses from discriminators and coincident module in a user-defined time window and presents the information on a visual display;
- Fan-out LeCroy 429: it allows reproducing the digital input signal in several identical output signals; the distribution of beam trigger signal is provided by this device.

Figure 2.18 shows the DAQ chain with the NIM modules for both scintillators of the GIF++ beam trigger. The same instrumentation has been also used in laboratory for the characterization of the detectors before the installation at GIF++, except for the CESAR interface. The CESAR interface is a module in NIM standard that allows uploading on the web the counts from the detectors 1 and 2 and the counts in coincidence. The information, recorded with CESAR, is available through the software TIMBER, developed by CERN IT service [18].

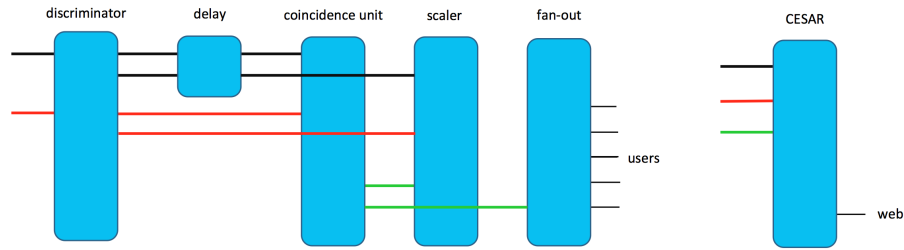


Figure 2.18: The sketch shows the data acquisition, installed at GIF++, in order to count the muons per spill in the beam. The cables concerning the detector 1 are in black, the cables dedicated for the detector 2 are in red and the cables for the signals in coincidence are in green. Every cable is LEMO.

In figure 2.19 it is possible to see as the analog signal from detector 1 arrives before the one from detector 2. The measurement is taken in laboratory with LEMO cables of same length for both detectors, so the signal of detector 1 is delayed for 15 ns in order to have the signal coming from the same cosmic muon at the same moment in both detectors (figure 2.20). The same delay is also taken into account during the operation of beam trigger at GIF++.

The two detectors are overlapped with detector 0, which acts as reference for the trigger (threshold selected for trigger: -20 mV). The overlapping is needed to study

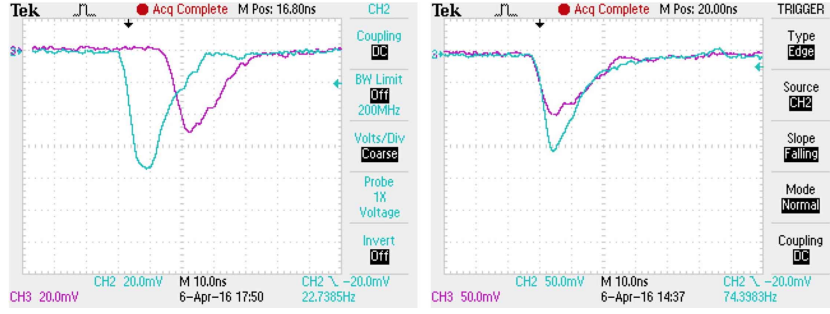


Figure 2.19: Signals from detector 1 (in blue) and detector 2 (in purple) without delay (on the left) and with delay (on the right) of 15 ns. Trigger threshold set for the detector 1 at -20 mV. Measurements have been taken in laboratory with LEMO cables of same length for both detectors.

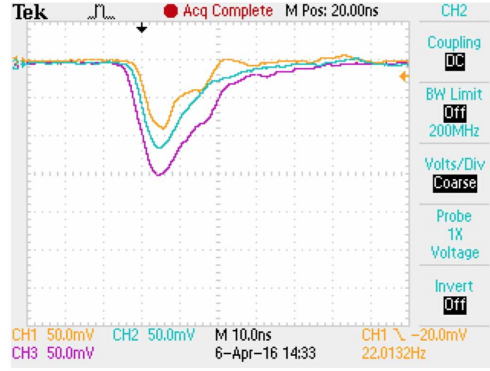


Figure 2.20: Signals coming from the same cosmic muon at the same moment in every detector. The detector 0 is in yellow, the detector 1 is in blue and the detector 2 in purple. Trigger threshold set for the detector 0 (as a reference for the study of the other ones) at -20 mV.

the detectors in coincidence and characterize them with cosmic muons. Figure 2.21 shows that they are placed in order to maximized the overlapping area and at the same time try to avoid damages to their structure.

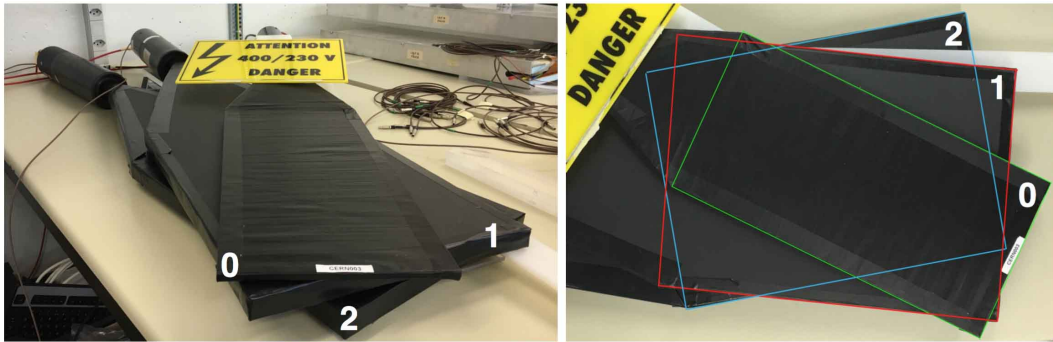


Figure 2.21: The three detectors are overlapped in order to maximized the area and at the same time try to avoid damages to their structure. The characterization is carried out with cosmic muons.

For the performance assessment of detectors 1 and 2, the assumption of cosmic muons to evaluate correctly the flux is taken equal to $1 \frac{\mu\text{uon}}{\text{cm}^2 \cdot 60 \text{ s}}$. This is a good approximation of flux because the expected average value is about $100 - 200 \frac{\mu\text{uons}}{\text{m}^2 \cdot \text{s}}$. All measurements are taken in 100 s. In table 2.2 the overlapping areas and the expected cosmic muons are calculated:

concidence	overlapping area	expected muons
0 and 1	$(751 \pm 6) \text{ cm}^2$	$(1252 \pm 10) \mu\text{uons}$
0 and 2	$(645 \pm 8) \text{ cm}^2$	$(1076 \pm 13) \mu\text{uons}$
1 and 2	$(1083 \pm 7) \text{ cm}^2$	$(1805 \pm 12) \mu\text{uons}$

Table 2.2: Overlapping areas and expected muons calculated in coincidence between detectors 0 and 1, detectors 0 and 2 and finally detectors 1 and 2.

For finding the correct operational settings of DAQ system, the threshold of the discriminator LeCroy 4608C is chosen when the coincidence counts are close to expected values. In figure 2.22 the counts in 100 s in coincidence between detector 0 and 1 are shown, whereas the figure 2.23 shows the counts for the coincidence of detector 0 and 2.

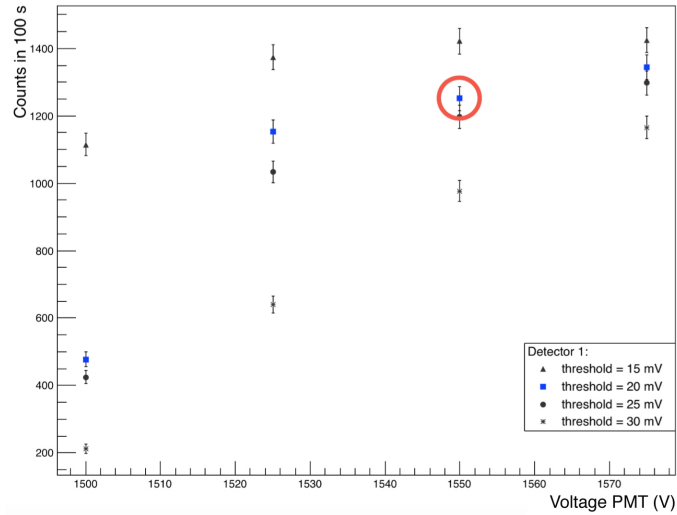


Figure 2.22: Counts of muons in 100 s in coincidence of detectors 0 and 1 depending on trigger threshold of the discriminator for the detector 1. The working point of detector 1 is marked with the red circle.

At the working voltage of detector 1 (1550 V) and threshold of discriminator equal to -20 mV , the count of muons in 100 s is (1250 ± 40) , in comparison with (1252 ± 10)

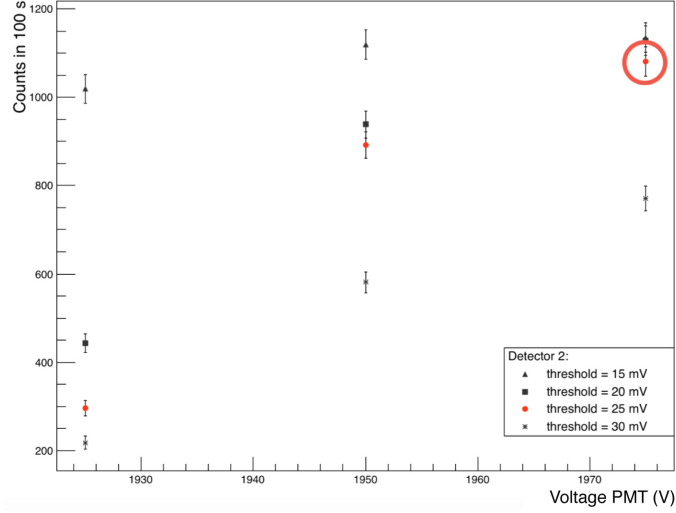


Figure 2.23: Counts of muons in 100 s in coincidence of detectors 0 and 2 depending on trigger threshold of the discriminator for the detector 2. The working point of detector 2 is marked with the red circle.

expected muons. In the case of detector 2, the count of muons in 100 s is (1080 ± 30) when the threshold is set at -25 mV, whereas the expected muons are (1076 ± 13) . The values of expected muons and measured muons are compatible for both detectors.

After five measurements of 100 s long, the average value of counts in coincidence between detector 1 and 2 is (1810 ± 20) and the expected muons are (1805 ± 12) , because the overlapping area is (1083 ± 7) cm². In figure 2.24, the measurements with detectors 1 and 2 in coincidence are presented. Coincidence counts with cosmic muons are fully compatible; so high voltages for detectors and thresholds for DAQ, selected in laboratory, are currently used for the beam trigger system at GIF++.

In table 2.3 the working points of detectors for the beam trigger are summarized.

detector	applied voltage (V)	current (μA)	trigger threshold (mV)	delay (ns)
1	1550 ± 6	910 ± 20	-20.0 ± 0.1	15.0 ± 0.2
2	1975 ± 7	1040 ± 20	-25.0 ± 0.1	0

Table 2.3: Summary of settings for the detectors 1 and 2.

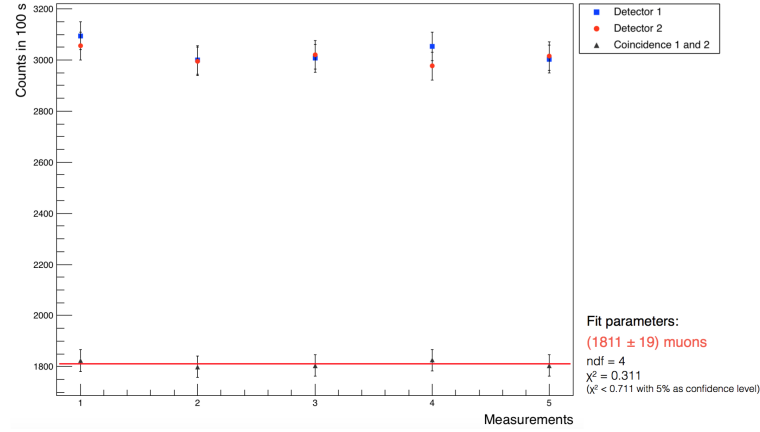


Figure 2.24: Five measurements with detectors 1 and 2 in coincidence. The counts are taken in 100 s.

Installation of beam trigger at the Gamma Irradiation Facility

After the characterization and optimization of the two detectors for the beam trigger in laboratory, they have been installed at GIF++ in correspondence of beam line outside the bunker. The first detector is in the upstream region and the second one is in downstream area. Figure 2.25 shows the position of detectors. The DAQ system is located in the area dedicated for electronic service and the trigger signal is currently provided to users. The position of detectors is outside the bunker to avoid radiation damages.



Figure 2.25: On the left there is the photo of detector 1, placed in the upstream region outside the bunker; whereas the detector 2 (on the right in the figure) is located in downstream region between GIF++ and the facility CMS-ECAL.

During the installation of beam trigger system, it has been necessary to measure the length of coaxial cables (LEMO), which carry the analog signal from the detector to the DAQ system.

For this measurements, the pulse generator Agilent 81180A and the oscilloscope TEKTRONIX TDS2024B have been used. The figure 2.26 shows a sketch of experimental setup for the measurements of cable lengths.

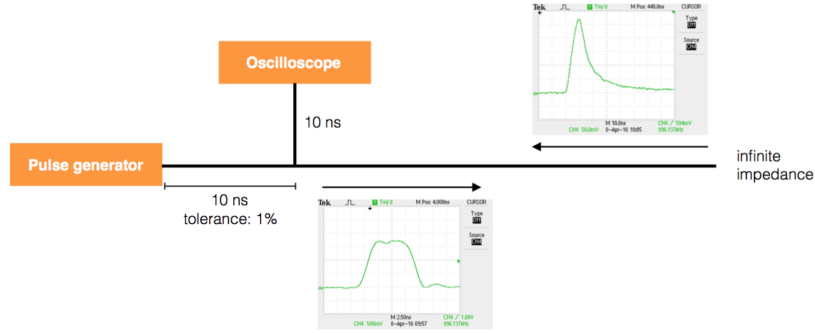


Figure 2.26: Sketch of experimental set-up to measure the length of upstream cable and downstream cable.

The pulse generator generates pulses with a frequency of 1 MHz and the oscilloscope measures the difference in time between the input pulses and the reflected pulses. The LEMO cables for the upstream detector and for the downstream detector have a rated delay of $(5.06 \pm 0.1) \text{ ns/m}$. When the cables are not connected to the detector, the impedance at the end of the cable is infinite and the reflected pulse has the same amplitude of the input pulse, in case of an ideal delay line. In a real delay line, the reflected pulse is attenuated of course. Figure 2.27 shows how quickly the reflected signal arrives to the other end of the delay line for the cable in upstream region and for the one in downstream.

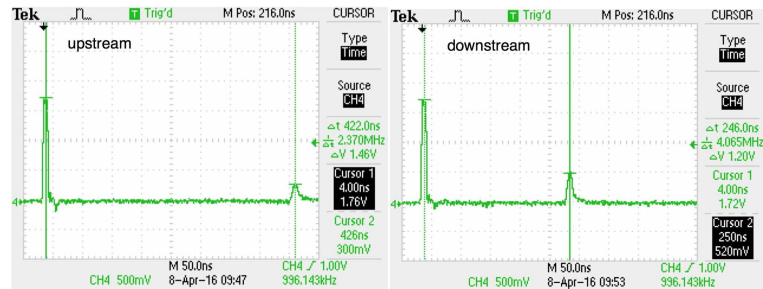


Figure 2.27: The measurements are taken with oscilloscope and show how quickly the reflected pulse arrives to the other end for the upstream cable (on the left) and the downstream cable (on the right).

The measurements of time period with the oscilloscope have to be divided by two in order to take into account that the pulse is reflected at the end of the line and then it is measured at the other end. For the upstream cable, the difference in time between the input pulse and the arriving time of the reflected pulse is (402 ± 20) ns, so the pulse needs (201 ± 10) ns to propagate from one end to the other one. For the downstream cable, the time of propagation in only one direction is (113 ± 10) ns. With a rated delay of (5.06 ± 0.1) ns/m for the LEMO cable, the length of upstream cable is (40 ± 2) m, whereas the downstream cable is (22 ± 2) m long.

In the DAQ system, a delay of 16 ns has been added for having both signals in coincidence. Therefore the time-of-flight of muons from the detector 1 to detector 2 is about 72 ns, that means a distance of about 22 m.

In figure 2.28 the positions of both detectors are marked. The distance, obtained by time-of-light of muons, is reasonably compatible with the distance of detectors in the map. Figure 2.29 shows the counts of the upstream detector (red), the downstream

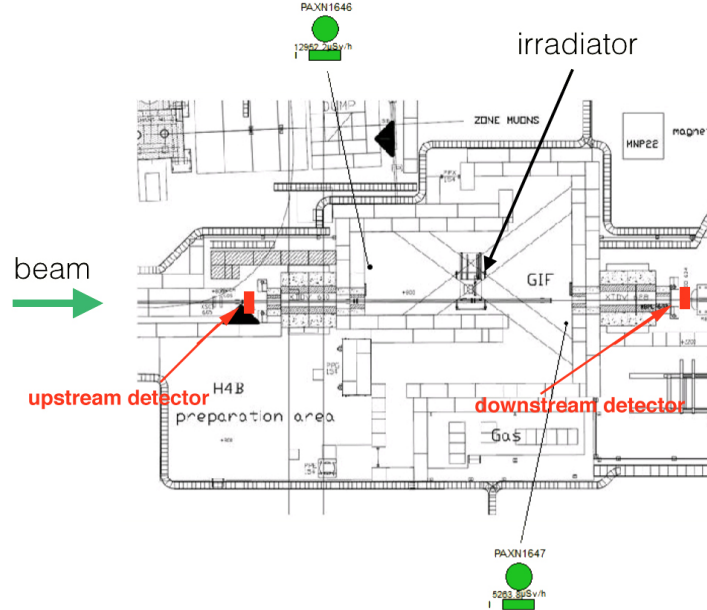


Figure 2.28: Map of GIF++ where the position of detectors (upstream and downstream) is indicated.

detector (blue) and the counts in coincidence (green). The period is from 1st May 2016 to 8th June 2016 and includes two beam periods dedicated only to GIF++ and one shared with another facilities, placed in the same beam line. At GIF++, the order of magnitude of muons is 10^4 per spill: the average number can slightly change

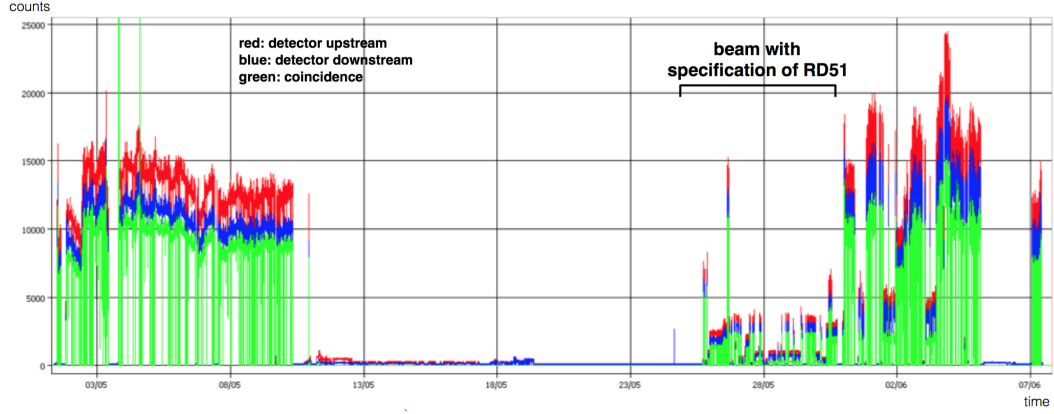


Figure 2.29: Counts of upstream detector (in red), the downstream detector (in blue) and counts in coincidence (in green) from on 1st May to 8th June. The software used for the plot is TIMBER, in which all data (uploaded by CESAR interface) are available.

because of difference settings of magnets and collimators along the beam line.

In the future, when the beam is not available (usually from November to April), there will be the possibility to use the cosmic trigger. The cosmic trigger is based on Resistive Place Chambers (RPC) and it is going to place in the downstream irradiation area. The system for triggering the cosmic muons is made up of one RPC under the bunker floor and the second one on the roof, attached to the ceiling of the bunker. The cosmic trigger is expected to be operational in 2016.

Chapter 3

Research and development on GEM detectors for HL-LHC

3.1 Gaseous ionization detectors: working principles

Gaseous ionization detectors are based on signal produced by electron-ion pairs, which are released in the gas mixture by the radiation passing through it. The gas is a proper medium for the collection of signals from incoming radiation when large surfaces have to be covered. The number and the distribution of the electron-ion pairs created in the gas volume depend on the nature and energy of the incoming radiation and also on the type of gases. The electrons (primary electrons) and ions, released by ionization of the incoming radiation, might neutralize by recombination: however they can be separated by an external electric field, which move them towards the electrodes. The total number of primary ion pairs (N_T), released in a medium can be evaluated from the following formula:

$$N_T = \frac{\Delta E}{W_I} \quad (3.1)$$

where ΔE is the total energy loss in the medium and W_I is the average energy per ion pair, which varies between 20 eV and 40 eV for most gases. In table 3.1, the average energy per ion pair for some gases at normal temperature and pressure (NTP) is shown. In this work, the values of temperature and pressure at NTP conditions are 293.15 K and 101.325 kPa.

For evaluating the total number of ion pairs in a gas mixture, the following formula can be used with good approximation:

$$\frac{\Delta E}{\Delta x} = c_A \left[\frac{\Delta E}{\Delta x} \right]_A + c_B \left[\frac{\Delta E}{\Delta x} \right]_B + \dots \quad (3.2)$$

Gas at NTP	$W_I/(eV)$
<i>Ar</i>	25
<i>Xe</i>	22
<i>CO₂</i>	34
<i>CF₄</i>	54
<i>CH₄</i>	30

Table 3.1: Average energy per ion pair concerning some gases, used in the current gas mixture for gaseous detectors.

where $\frac{\Delta E}{\Delta x}$ is the energy loss per unit length, the parameters A, B, \dots represent the different gases in the mixture and $c_A, c_B \dots$ the relative mass concentrations.

Charge multiplication in gaseous detectors occurs when the primary ionization electrons gain sufficient energy to generate secondary ionization. Indeed when the energy of the electrons, accelerated by electric field, exceeds the ionization potential of the atom or molecule in the gas mixture, bound electrons can be ejected and there is a significant multiplication of the free charges, originally created by the passage of radiation [8]. This mechanism of signal amplification, which occurs in the gas mixture, is the working principle for gaseous detectors. Under the action of electric field, the electrons are accelerated toward the anode and the ions towards the cathode, where they are collected. The current signal in a general gaseous detector depends usually on the electric field strength, applied into the gas volume, and also on the gas mixture used. Figure 3.1 shows the number of ions collected as a function of applied voltage in a single wire gas chamber, that can be considered as the basic configuration of a general gaseous detector.

When the applied voltage is equal to 0 V (so no electric field), no charge is collected and the electron-ion pairs can recombine under mutual electrical attraction. As the voltage is raised, the recombination forces are overcome and the current begins to increase, until all pairs will be collected. At this point, a small increase of the voltage shows no effect and this corresponds to the flat region *II* in figure 3.1. In this region, the electron-ion pairs, released in the gas mixture by the incoming radiation, are just collected, so the signal is very small. The detectors, which operate in this region, are known as *ionization chambers*.

If the voltage is increased beyond region *II*, the electric field is strong enough to accelerate electrons, which can ionize the gas mixture. Then electrons liberated in the secondary ionization can produce more ionization and keep doing this process. The result is the formation of an avalanche. Therefore the number of electron-ion pairs

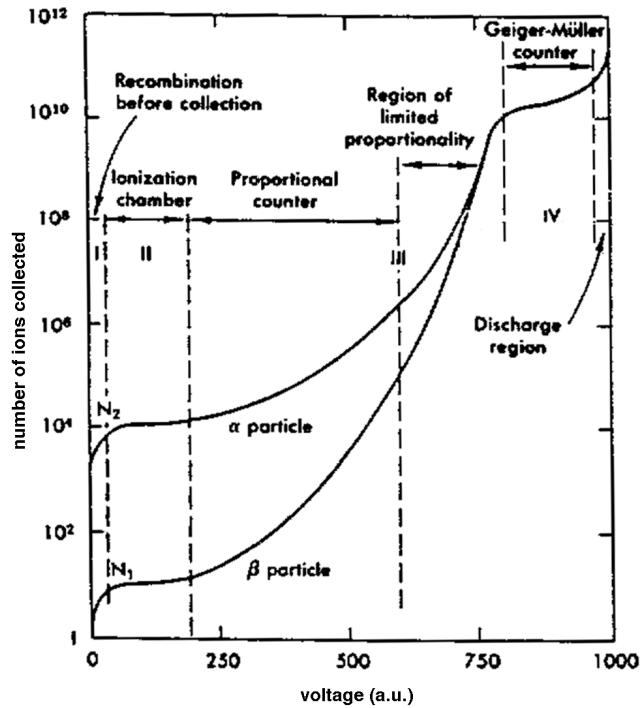


Figure 3.1: The number of electron-ion pairs when a charged particle goes through a single wire gas chamber as function of applied voltage. Curve N_1 is for a minimum ionizing particle, whereas curve N_2 refers to a heavily ionizing particle [19].

in the avalanche is directly proportional to the number of primary electrons. Detectors, which work in this region, are called *proportional chambers* and it is usually the working region for gaseous detectors. Since the electrons are more mobile than the ions, the avalanche has the form of a liquid-drop, as shown in figure 3.2.

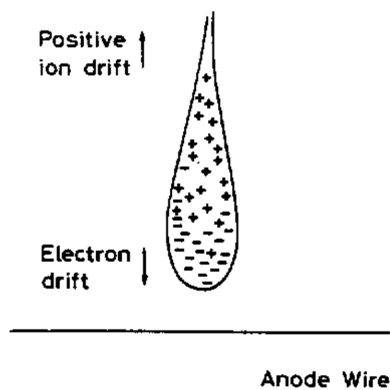


Figure 3.2: Drop-like shape of an avalanche with the electrons at the head, due to the greater mobility of them [17].

The first Townsend coefficient is equal to the inverse of the mean free path of electrons for a secondary ionizing collision and corresponds to the probability of ionization per unit length. Indeed in a region where the electric field is uniform, one electron-ion pair is created after a mean free path $1/\alpha$. If n is the number of electrons in a given position, the increase of their number after a path dx is:

$$dn = n \alpha dx \quad (3.3)$$

Integrating over a path length equal to x , the expression becomes:

$$n = n_0 e^{\alpha x} \quad (3.4)$$

where n_0 is the number of electrons before the drifting along the path x . The charge multiplication factor is then:

$$M = \frac{n}{n_0} = e^{\alpha x} \quad (3.5)$$

Since α is a function of x , in the more general case of non-uniform electric field, the expression becomes:

$$M = e^{\int_{x_1}^{x_2} \alpha(x) dx} \quad (3.6)$$

After the proportional region, if the voltage is increased again, the charge multiplication becomes so large that it can start distorting the electric field, so the proportionality of the signal is lost.

At higher voltage, the electric field becomes so high that discharges occur in the gas mixture. Indeed the high density of charges (electrons and ions) in the avalanches modify the original electric field: it increases in front of and behind the avalanche, as shown in figure 3.3.

Photons emitted by de-exciting molecules produce further ionizing events and the initial avalanche spreads out in many avalanches, so a transition from avalanche to streamer occurs. Detectors, which are in this operational region, are usually called Geiger-Müller counters.

3.2 Triple-GEM performance in presence of high background radiation

The ageing effects on gain, materials and gas composition for different gaseous detectors have been studied for decades, but the high radiation background foreseen at LHC requires additional studies because it will exceed the levels previously tested.

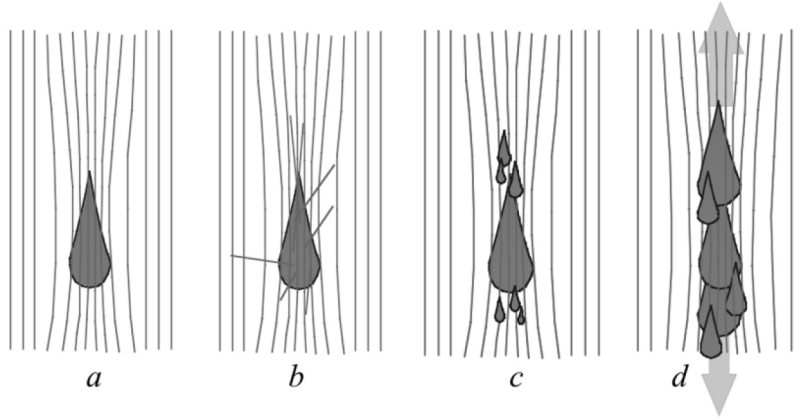


Figure 3.3: Schematic representation of the transition from avalanche to streamer in a gaseous detector at high electric field. Due to the high density of charges (electrons and ions), the original electric field is modified, increasing in front of and behind the avalanche (a). The emission of photons creates secondary electrons by photo-ionizations of the gas mixture (b), so they can produce secondary avalanches in the regions of higher field (c). The process continues with the propagation of further avalanches, starting a streamer (d) [8].

Indeed the background radiation could affect the detector response in term of decreasing the rate capability and shortening the lifetime through ageing. The R&D studies, conducted in this thesis, at CERN GIF++ are mainly focused on understanding performance of triple-GEM detectors for future experiments and application at HL-LHC.

Several processes in the gaseous detectors can lead to ageing phenomena. In a typical avalanche, electrons and photons have enough energy that can produce molecular fragments in the gas mixture, which can interact with materials and components of detector, causing ageing effects through processes of polymerization or etching. Polymers have an excellent adhesion to the surfaces and their deposition can cause a deformation of the electric field. Also the presence of unwanted pollutants in the gas mixture, for example due to the outgassing of detector components or contamination from external, can affect performance of gaseous detectors.

In particular the R&D studies at GIF++, to which I participated, are focused on the study of GEM performance under gas recirculation with different gas mixtures and recirculation fractions.

3.3 Principle of operation of triple-GEM and SW-PCs

A triple-GEM detector and two Single Wire Proportional Chambers (SWPCs) have been installed at CERN GIF++. The present study is focused on the GEM detector, whereas SWPCs are used for monitoring the stability of the gas mixture.

Triple-GEM detector

The gas electron multiplier is a thin polymer foil, metal-coated on both sides and pierced with a high density of holes, typically 50-100 per square millimeter [8]. The foil is generally perforated by a chemical processes or by laser drilling.

A detector with three piled-up GEM foils (usually named triple-GEM detector) is more convenient than a single-GEM detector. Indeed in a triple-GEM detector low voltages are sufficient to get the same gain of a single-GEM detector.

In the experimental set-up under test at GIF++, the foils of the triple-GEM detector have a $50\ \mu\text{m}$ thick insulating structure in Kapton, coated with a thin copper layer ($5\ \mu\text{m}$) on each side. The holes have a double-conical shape, due to the particular chemical process for the perforation of the foil, with an external diameter of $70\ \mu\text{m}$ and internal of $50\ \mu\text{m}$. The pitch of the holes is $140\ \mu\text{m}$. Figure 3.4 shows a microscope view of a GEM electrode, whereas figure 3.5 shows the characteristic double-conical shape of the holes in a GEM foil.

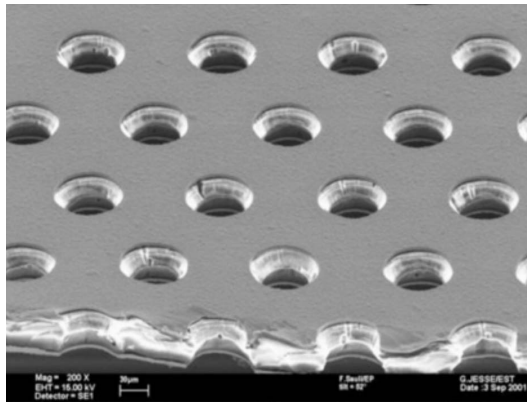


Figure 3.4: View of a GEM electrode with holes diameter of $70\ \mu\text{m}$ and pitch equal to $140\ \mu\text{m}$.

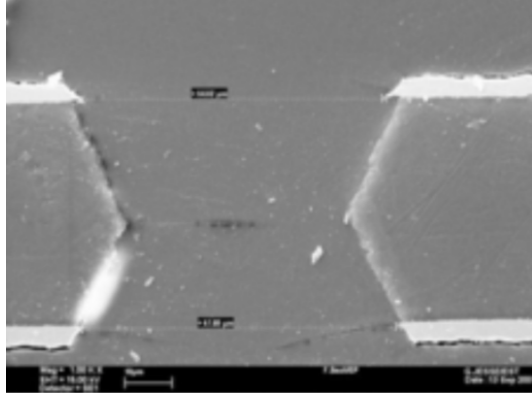


Figure 3.5: Typical bi-conical shape of a hole in a GEM foil.

A photo-lithographic technique is usually used to get the desired pattern of the holes. The copper-clad Kapton foil is laminated with a photosensitive coating (photo resist) in both sides and exposed to the UV light through a mask with the pattern of the holes. After hardening, the photo resist is removed with a chemical solution in the exposed areas and the copper layers are etched. Then the foil is immersed in a polymer solvent to open the holes in the regions not protected by metal. The last process causes the bi-conical structure of the holes, with a smaller diameter in the centre.

A suitable voltage is applied between the two copper layers in order to generate a high electric field inside the holes (the order of magnitude is about $10 - 100 \text{ kV/cm}$), which act as multiplication channels. Figure 3.6 shows a qualitative scheme of the multiplication of electrons and ions through the holes of a single GEM foil.

Figure 3.7 shows the multiplication of an avalanche in a triple-GEM detector: the number of electrons increases usually going through each foil to reach a final gain of about $10^4 - 10^5$.

In order to power on the detector, a voltage divider is used; it is optimized for gas mixture containing CF_4 . In our specific application, the voltage divider is shown in figure 3.8.

Using the figure 3.8 notation, the drift gap (d_{drift}) of the triple-GEM detector installed at GIF++ is equal to 3 mm , the first transfer gap (d_{gap1}) and the induction gap (d_{gap3}) are 1 mm and finally the second transfer gap (d_{gap2}) is 2 mm thick. The total size of GEM foils is $10 \times 10 \text{ cm}^2$.

The gas mixture for triple-GEM detector operation is usually based on Ar and CO_2 , the latter acting as quencher gas, with the possibility to add CF_4 for increasing the

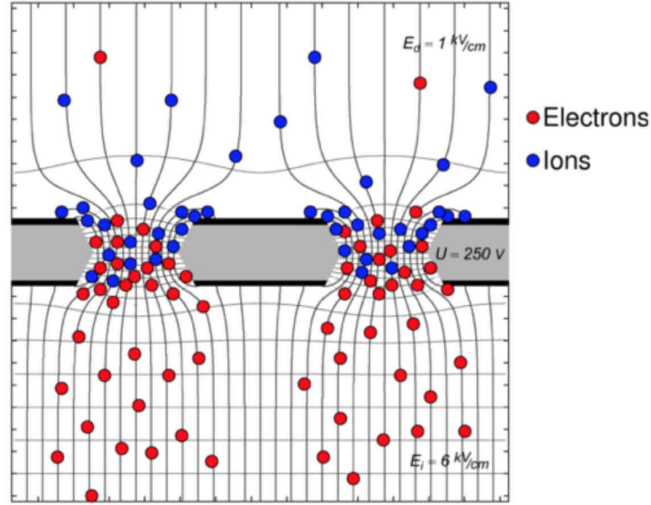


Figure 3.6: Qualitative scheme of the multiplication of electrons and ions in a single GEM foil. In the figure, the electric field lines and equipotential lines are drawn in proximity of the GEM foil. Most of the electrons, generated in the avalanches, are transferred into the lower region where an electrode, patterned with strips or pads of arbitrary geometry, collects them.

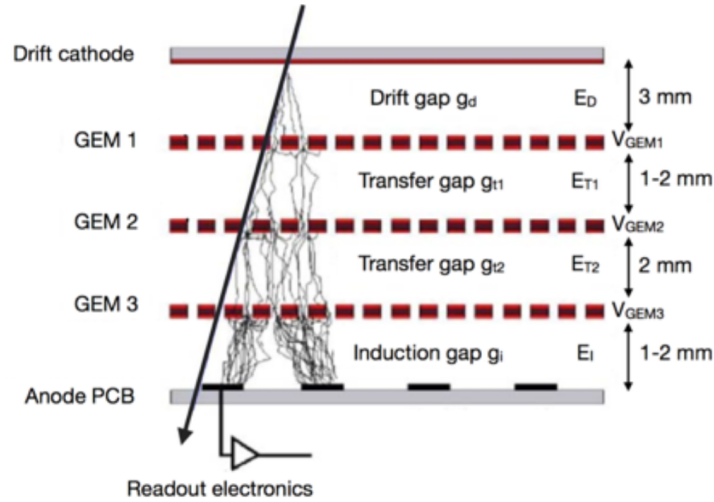


Figure 3.7: Schematic view of electron multiplication through three GEM foils in cascade.

time resolution of detector.

Single wire proportional chambers

A SWPC has usually a cylindrical coaxial geometry in conducting material. A thin metal wire is stretched along the axis of the cylinder and insulated from it with high voltage feedthrough. A difference of potential is applied between the central wire (the

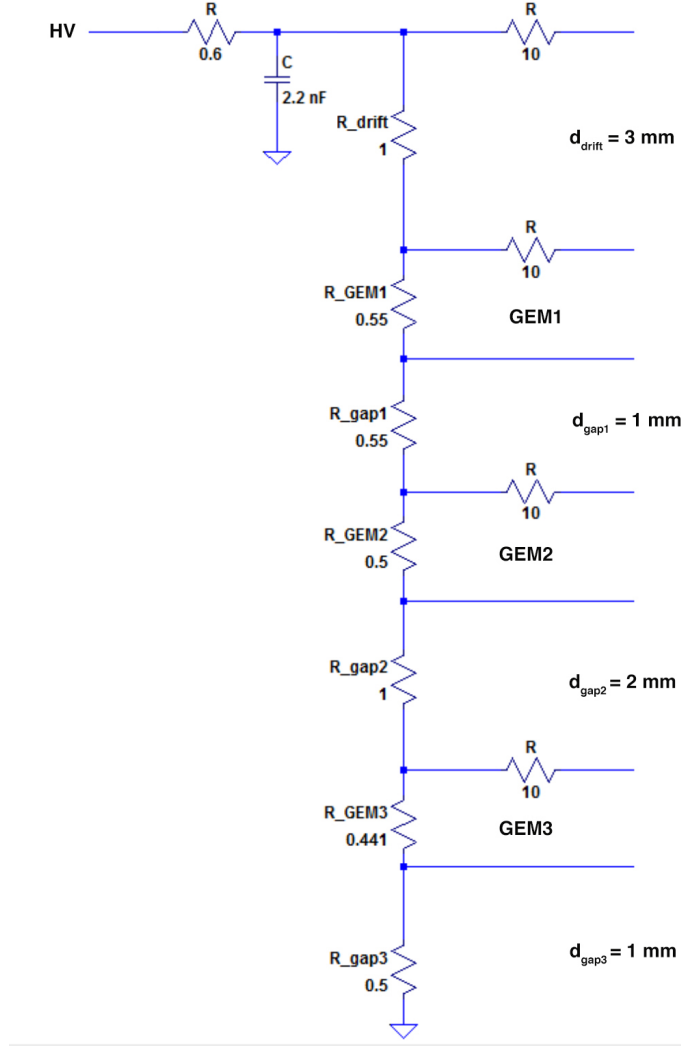


Figure 3.8: Voltage divider used for the triple-GEM detector under test at GIF++. All of resistors' values are in $M\Omega$. The resistors R , equal to $10 M\Omega$, are used as protection from short circuit. In the input of the voltage divider, there is a low-pass filter with a resistor of $0.6 M\Omega$ and a capacitor of $2.2 nF$ to attenuate high frequency ripple in HV.

anode) and the outer cylinder (the cathode) to get an electric field inside the tube. For a cylindrical geometry, the electric field is given by:

$$E(r) = \frac{V_0}{\log \frac{b}{a}} \frac{1}{r} \quad (3.7)$$

where V_0 is the applied voltage, a is the radius of the anode, b is the inner radius of the cathode and r is the distance from the centre of the wire. The electric field is highest at the surface of the wire and decreases rapidly towards the cathode, so the multiplication region is a very small volume close to the anode (less than a few wire radii). Figure 3.9 shows the cross-section of a SWPC and its electric field.

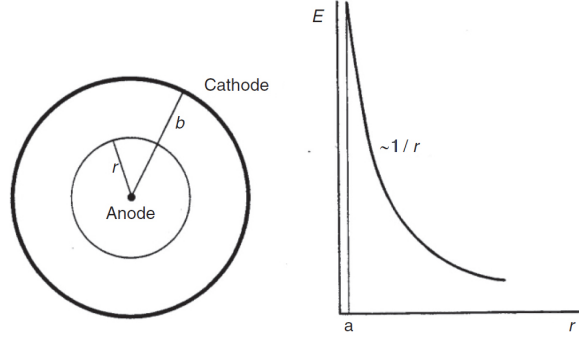


Figure 3.9: Cross-section of a SWPC and its electric field. The electric field is highest at the surface of the wire and decreases rapidly towards the cathode, for this reason the multiplication region is small and close to the anode [8].

The primary electrons, released by the passage of particles, drift towards the anode wire under the effect of the electric field. Near the anode wire, the electric field is strong enough to allow primary electrons to start the charge multiplication; indeed, they can get enough energy to produce secondary ionization up to the formation of an avalanche. Figure 3.10 shows the growth of an avalanche around the anode wire.

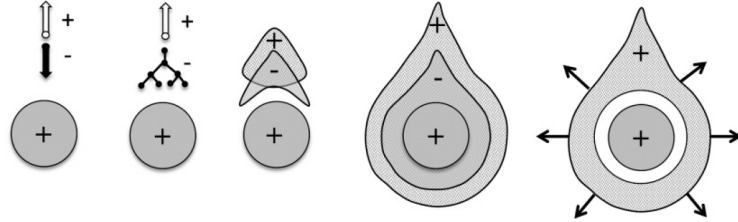


Figure 3.10: Avalanche growth around the anode wire [8].

The SWPCs are usually used as proportional counters, so the detected signal is proportional to the primary ionization.

3.4 Experimental setup for R&D at GIF++

Data acquisition

A data acquisition system has been set-up for the characterization of a GEM detector under irradiation at GIF++. The system is located partly inside the irradiation bunker and partly outside. For the test, three detectors are used:

- one triple-GEM is irradiated by the GIF++ ^{137}Cs source and at the same time by a radioactive source of ^{55}Fe , with activity of 1.2 MBq ;

- two SWPCs (each detector is irradiated by a radioactive source of ^{55}Fe).

Figure 3.11 shows a schematic view of the data acquisition system installed at GIF++.

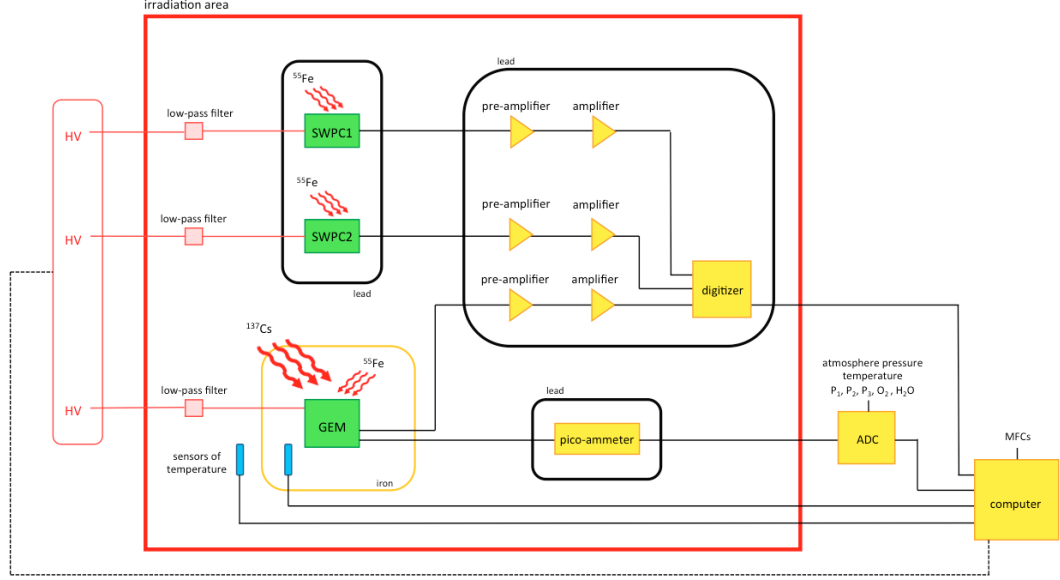


Figure 3.11: Schematic view of the data acquisition, used during the test. Some devices are installed inside the irradiation bunker (surrounded by red square) and some ones outside, for constant checks and tunings.

The detector voltages are controlled and monitored with the CAEN mainframe SY1527. The voltage for the GEM detector is applied by the CAEN module A1833N (negative polarity) and for the SWPCs the CAEN module A1832P (positive polarity) is used. Each high voltage line has a low-pass filter to attenuate high frequency ripple in the HV.

The SWPCs, installed in the GIF++ bunker, are located inside a box in order to be shielded by the photons emitted by ^{137}Cs source. The GEM detector is placed in an iron box, which acts as Faraday cage and also as container of N_2 to avoid or at least limit an excessive contamination of air in the gas mixture: indeed the GEM frame is permeable to the air. In figure 3.12, there is an inside view of the box where the SWPCs are located while figure 3.13 shows a picture of the GEM detector in the iron box.

The amplification of GEM and SWPC signals is obtained with a custom-made pre-amplifier and the ORTEC 474 amplifier:

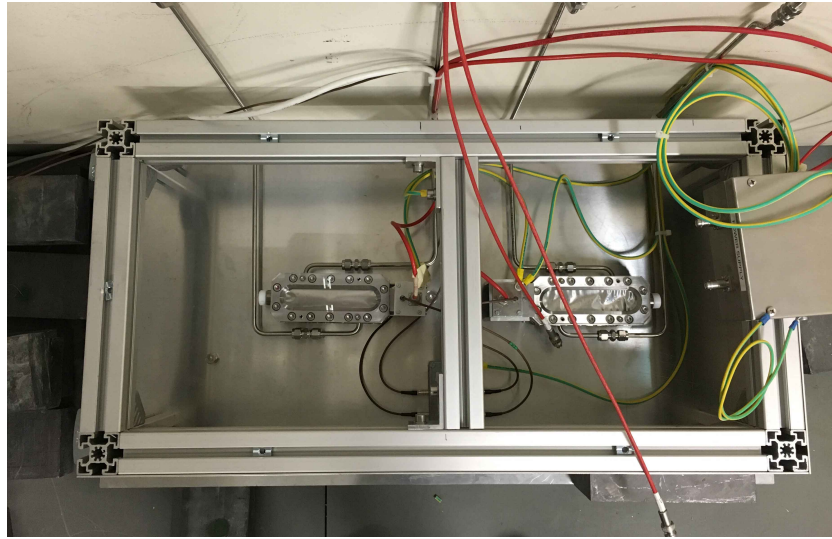


Figure 3.12: Inside view of the box where the SWPCs are located. The walls of the box are shielded by lead bricks $10\text{ cm} \times 20\text{ cm} \times 5\text{ cm}$. Two lead plates cover the upper surface of the box with a total thickness of 3 cm .

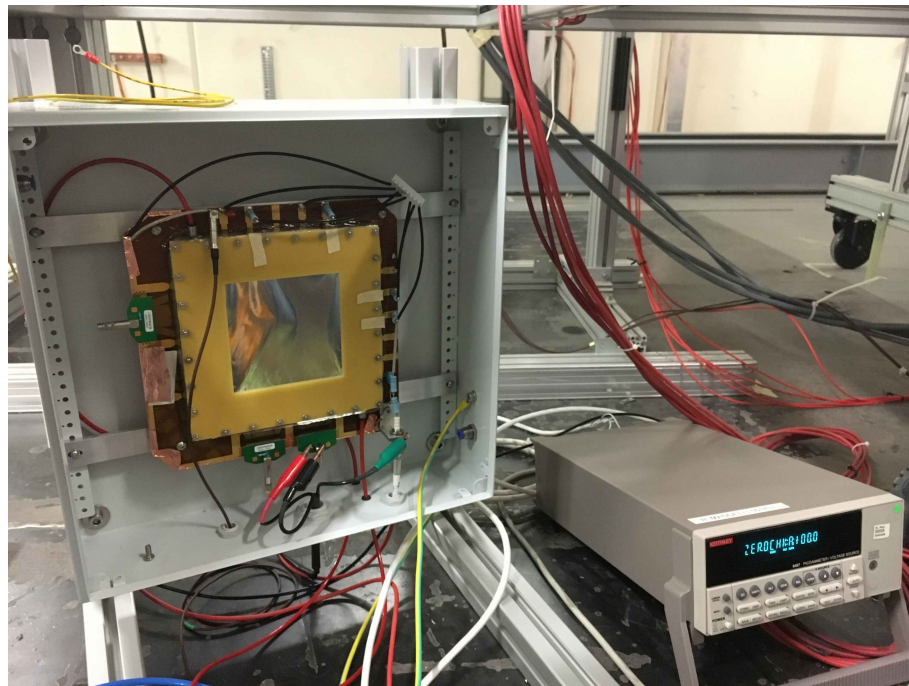


Figure 3.13: GEM detector inside the iron box, which acts as Faraday cage. Inside the box, a radioactive source of ^{55}Fe is placed in the middle of the aluminium window. Close to the box, there is a pico-ammeter to measure the current of the GEM detector during the irradiation of ^{137}Cs source. A lead cage shields the device from radiation damages. The ^{55}Fe source and the lead cage are not visible in the photo, because they were added only at the end of the installation.

- The output of the pre-amplifier is an inverting voltage pulse, which is proportional in peak amplitude to the integrated charge of the input signal;
- The ORTEC 474 amplifies the signal coming from the pre-amplifier and allows optimizing the signal-to-noise ratio.

The amplified signals are then acquired with the CAEN digitizer DT5724, which has 14 *bits* resolution and an acquisition rate of 100 *MS/s*. The full dynamic range of the digitizer is 2.25 V_{pp} . For the three channels in use (one channel per detector) a threshold is set: if the analog signal in input is above the selected threshold, it is digitalized and saved.

The analog signal from the GEM is measured directly from the third GEM foil, while the current is recorded from the anode read-out strips through a pico-ammeter Keithley 6487, which is placed close to the GEM, as shown in figure 3.13. An analog-digital converter (PicoLog ADC-24), outside the irradiation bunker, is used to record the current of the detectors.

The ADC is also used to record the gas and environmental parameters with a software based on C++ and developed specifically for this application. In particular, the ADC digitalizes the output signal of:

- temperature and atmospheric pressure sensors;
- three pressure sensors of the gas system;
- O_2 and H_2O vapour sensors in order to measure the concentration in the gas mixture.

In particular, it has been decided to install at GIF++ a sensor of atmospheric pressure (NESA BAR A10SS2) in the rack and three sensors of temperature (Electrotherm DTM 5080 with Pt100): the first one inside the iron box of the GEM detector, the second one in the irradiation area outside the box and the last one has been placed in the gas recirculation rack for monitoring the temperature outside the irradiation area.

At the end of the data acquisition, a computer records and analyses the data; moreover it controls the high voltage of the detectors and it is used for a real-time monitoring of the facility, like the environmental parameters and the status of the source, available on the DIP platform.

The GEM detector is placed in the downstream area of GIF++. The distance between the radioactive source and the detector is 2.7 m. Figure 3.14 shows the positions of triple-GEM, pico-ammeter and DAQ devices in the bunker.

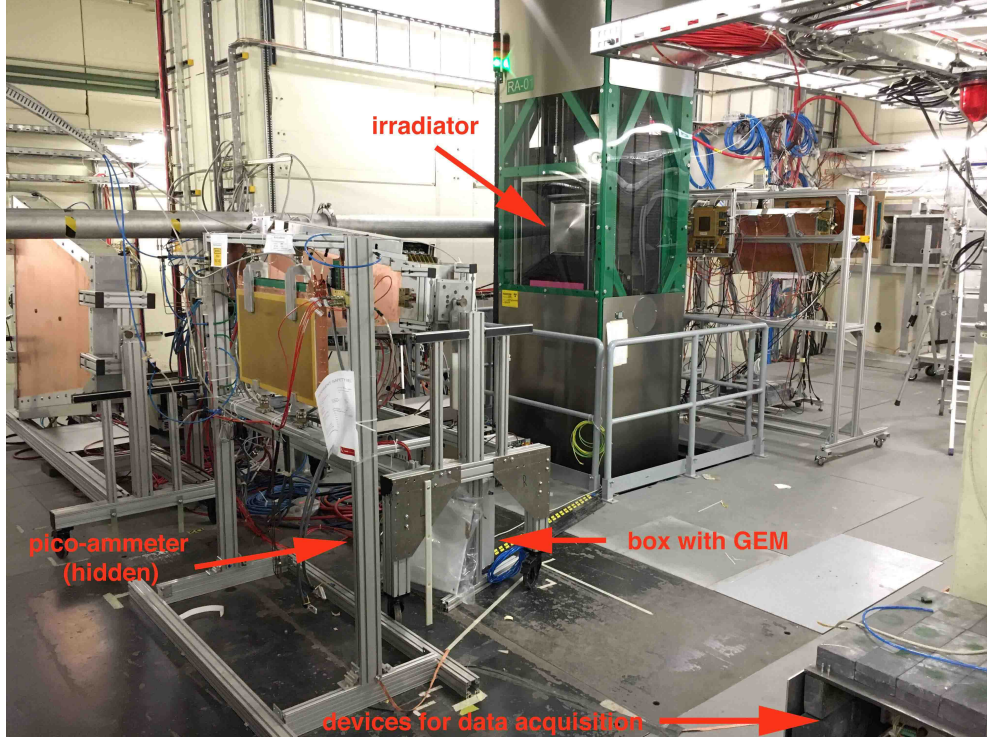


Figure 3.14: Position of some devices in the irradiation area of GIF++.

The equivalent dose has been measured with a dosimeter (Automess 6150AD6/H) placed in front of the GEM. The equivalent dose rate on the GEM detector is $(17 \pm 2) \mu\text{Sv/s}$. The dose due to the ^{55}Fe source irradiation is not relevant because the activity of it is much lower than the activity of ^{137}Cs source.

The use of both sources on the GEM detector has a crucial relevance to understand the performance during the test. Indeed the source of ^{137}Cs is used for ageing while the ^{55}Fe source is needed to check the performance. The ^{55}Fe peak is well-defined in the pulse-height distribution of the triple-GEM detector under test at GIF++.

Software for data acquisition

Custom-made DAQ software has been developed and implemented to control and monitor the high voltages of the detectors, to monitor the environmental conditions of the facility and to store and analyse the data from detectors and different devices of measuring.

Software for mass flow controllers (MFCs)

Gaseous detectors are usually sensitive to variations in composition of gas mixture. Mass flow controllers are generally used to control the composition of the fresh gas mixture. Indeed three mass flow controllers F-210CM, provided by Bronkhorst [20], have been calibrated for Ar , CO_2 and CF_4 and they are now in use to regulate the precise concentration of each component in the fresh mixture (see *appendix A*). Figure 3.15 shows the three panels of software to control and monitor the Ar , CO_2 and CF_4 flows.

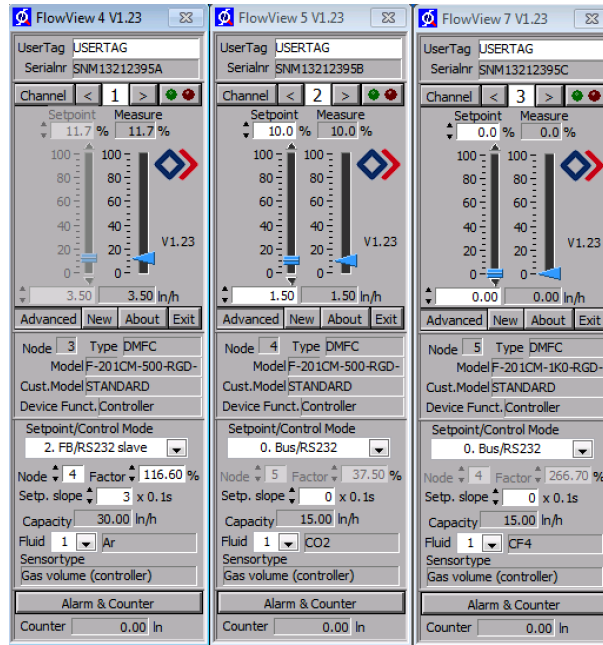


Figure 3.15: The Ar flow is set to 3.5 l/h, the CO_2 flow is 1.5 l/h, whereas the CF_4 flow is equal to 0 l/h in this case; so the total gas mixture has a composition of 70% Ar and 30% CO_2 .

DIP client

A DIP client has been developed to download the environmental parameters of the facility in real-time from the DIP platform, available at CERN. In particular, the atmospheric pressure, the temperature inside the irradiation area and the humidity of the bunker are handled. Indeed these parameters can affect the detector performance. Moreover the status of the source and the attenuation factors for the downstream area are monitored through this software. The interface of DIP client is shown in figure 3.16.

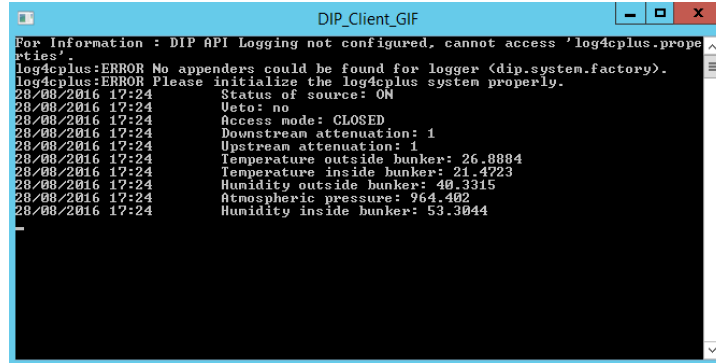


Figure 3.16: A DIP client has been developed to monitor and store the environmental parameters of the GIF++ in the downstream region (temperature, atmospheric pressure and humidity) and the status of source with possible attenuation factors.

CAEN Wrapper

The CAEN Wrapper is a program, provided by CAEN, that consists in several functions, based on C and bundled in a library. It is used to set and monitor the high voltages for the detectors. The software is also provided with a basic interface for an easy monitoring.

The CAEN Wrapper has been adopted to control the high voltages and monitor the currents of detectors under test. Indeed anomalies and unexpected situations in the recirculation system or in the composition of the filling mixture (for example a gas component is missing because the gas supply bottle is empty) can damage the detectors. Moreover if users at GIF++ set the ^{137}Cs source in the irradiation position and the GEM detector is already at the operating voltage, the current of detectors grows so rapidly that some damages may occur.

The software CAEN Wrapper has been modified to:

- decrease automatically the high voltage of the GEM detector from the operational voltage (usually greater than 3000 V) to a low voltage when the irradiation of the source is interrupted. The status of the source is read from the DIP platform and few seconds later the voltage is decreased automatically to a low voltage (in this case, 2500 V) ¹;
- increase gradually the voltage applied to the GEM detector up to the operational voltage, after few minutes that the radioactive source goes into the irradiation

¹It is better to avoid a complete switching off detectors, otherwise the stable operation conditions of them are achieved again after a time period of some days. The same strategy is also implemented in the experiments at LHC, preventing several days in which the data acquisition should be stopped.

position;

- monitor the current every second. If the current is higher than a specified threshold, the high voltage is decreased as fast as possible (the voltage drop is about 500 V/s) up to 0 V.

Figure 3.17 shows the software interface, developed to get the parameters of the GEM detector in channel 0 and the SWPCs, in channels 1 and 2 respectively. For each channel, the measured voltage (V_{Mon}) and the current (I_{MonH}) are monitored as well.

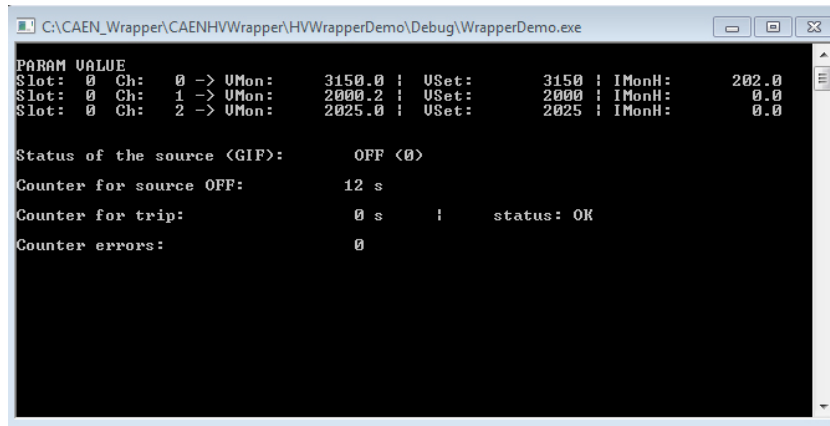


Figure 3.17: The CAEN Wrapper interface to control and monitor the high voltages of detectors. The software has been developed to avoid damages to GEM detectors during unexpected situations.

Acquisition data from ADC and digitizer

A software program has been implemented for the ADC in order to take ten different measurements every minute and calculate the average value. Moreover the ADC has also a logic TTL output, used to control the devices: indeed the software sends a trip signal to the high voltage module when the current of GEM is too high (threshold set to 100 nA), protecting it from damages.

In addition a further software program has been developed for the acquisition of signals from all detectors. Indeed every hour the signals from each channel of digitizer are acquired for a proper time period and saved. In particular, when the GEM detector is irradiated by both sources, the acquisition time is 10 s and the acquisition rate is about 10^3 Hz: in this condition, the internal buffer of digitizer is saturated, so only a part of incoming signals is acquired. On the contrary, the acquisition time is set to 120 s under irradiation of ^{55}Fe source only, because of a lower acquisition rate

(the order of magnitude is about 10^2 Hz). For both SWPCs, the acquisition time is 15 s and the acquisition rate is usually 10^3 Hz .

After the acquisition, the data are automatically analysed with a ROOT script. The analysis is focused on the conversion of the signals from the detectors into a pulse-height distribution. In this way the gain of the three detectors is evaluated with specific fits, as will be seen later.

Gas system

A sketch of the gas system used for the test at GIF++ is shown in figure 3.18. Three

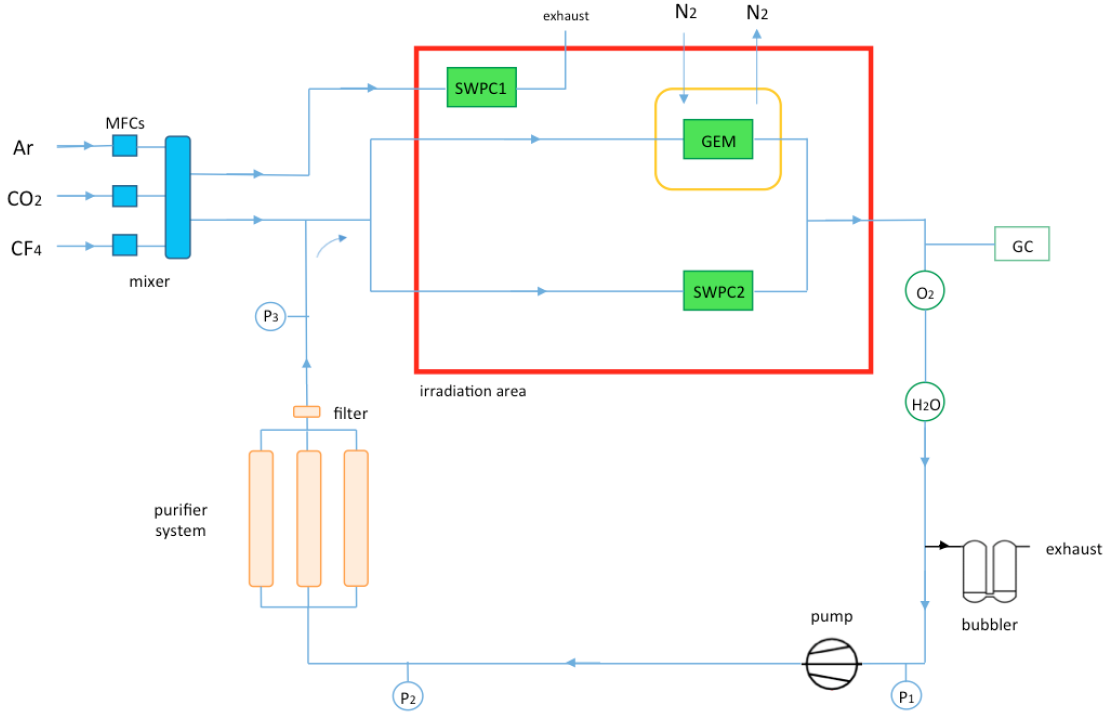


Figure 3.18: Sketch of the gas system used during the test at GIF++. The SWPC1 is in open mode, whereas the GEM detector and the SWPC2 are in closed-loop circulation. A purifier module, which can host up to three independent cartridges, cleans the gas mixture, coming out from the detectors.

mass flow controllers (MFCs) adjust the proportion of each component (Ar , CO_2 and eventually CF_4) to inject a constant and fresh gas mixture into the closed loop. An interlock system, based on *Siemens LOGO!*, has been developed to switch off the high voltages of the detectors in case one of the input gas flow becomes equal to zero.

The SWPC1 monitors constantly the gas mixture from the mixer. An addition of

fresh gases is constantly injected in the closed loop to avoid the excessive degradation of mixture. In the recirculation gas system, the triple-GEM detector and the SWPC2 are placed in two parallel lines, so that the SWPC2 monitors the gas mixture, which comes into the GEM detector.

The gas mixture coming from the GEM detector and SWPC2 is analysed by O_2 and H_2O sensors. It is also possible to connect directly the gas chromatograph when precise concentration measurements of each component and pollutant are needed. After the O_2 and H_2O vapour sensors, the desired recirculation fraction of gas mixture is sent to the purifier module (see *appendix A*) for removing the impurities and the pollutants, while the remaining fraction is sent to the exhaust through a bubbler, filled with water. The presence of a pump in the system ensures the gas circulation. Finally three sensors measure the pressure along the circuit: in figure 3.18 they are tagged in P_1 , P_2 and P_3 .

Behaviour of SWPC with variations in gas mixture concentration and in presence of pollutants

The SWPCs are used to get an instantaneous feedback on the quality of gas mixture, because they result to be very sensitive to the variations of it. Indeed previous studies have been carried out to understand the sensibility of SWPCs to small changes in the gas composition and also to the presence of pollutants, as O_2 or N_2 [21]. In any case the change of the SWPC performance should be always proved by a gas chromatography analysis for being sure that is not due to the behaviour of the detector.

Some results of previous studies on the response of SWPC are shown in figure 3.19 and 3.20. Figure 3.19 shows the amplitude variation of the signal and the energy resolution in a SWPC when the gas mixture is made up of $Ar/CO_2/CF_4$ (45/15/40) and the electric field is constant.

Figure 3.20 shows how the amplitude variation of the signal and the energy resolution change when a contamination of O_2 occurs in the gas mixture $Ar/CO_2/CF_4$ (55/40/5).

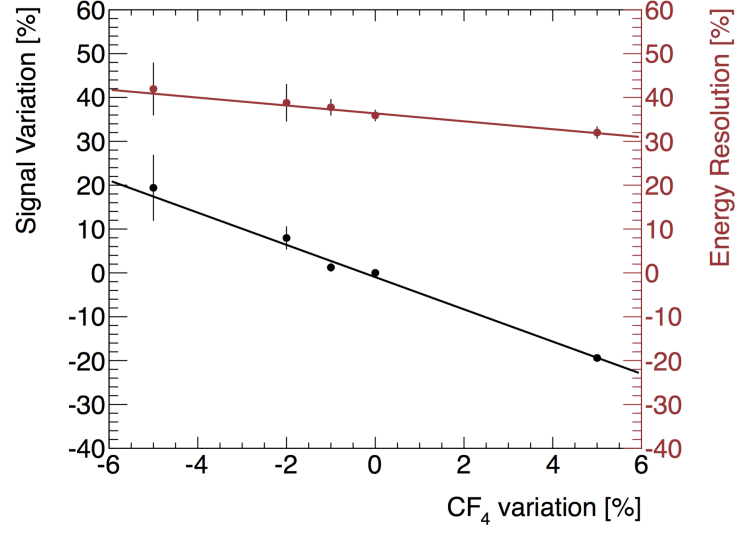


Figure 3.19: The amplitude variation of the signal and energy resolution in a SWPC depending on the CF_4 variation in $Ar/CO_2/CF_4$ (45/15/40). The electric field during the test was kept constant [21].

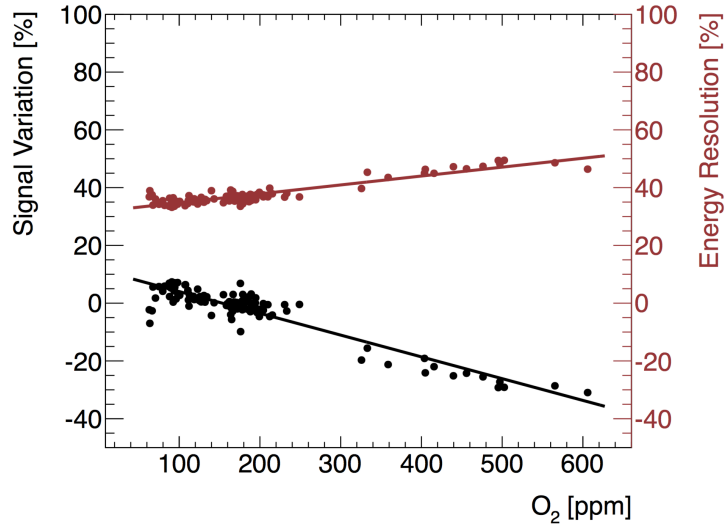


Figure 3.20: The amplitude variation of the signal and the energy resolution in a SWPC depend on the concentration of O_2 in $Ar/CO_2/CF_4$ (55/40/5). The electric field during the test was kept constant [21].

3.5 Characterization of triple-GEM and SWPCs for ageing test

Single wire proportional chambers

Two SWPCs have been made and assembled in a clean room at CERN (see *appendix B*), and then a characterization of them has been carried out before the installation at GIF++.

Two radioactive sources of ^{55}Fe with activity of about 1 *MBq* are used to identify the working voltage of both SWPCs and verify the stability of performance in time. The gas mixture for the characterization is *Ar/CO₂* (70/30). During the test in laboratory, the gas flow in each SWPC has been set at 1.0 *l/h*, equivalent to about 6 *volume/h*. The signals of SWPCs are amplified in two different stages (preamplifier and amplifier) and digitalized. The same instrumentation for the DAQ, used for the characterization, has been installed at GIF++ and described in details above.

A ROOT script was developed for the data analysis; in particular, for every triggered waveform, the signal amplitude is evaluated as the difference between the maximum of the waveform and the mean value of the baseline, evaluated in the first 200th samples. The pulse-height distribution is useful to quantify the detector performance; indeed the mean of the main peak is proportional to the effective gain of the SWPC. Figure 3.21 shows as example the pulse-height distribution of SWPC2.

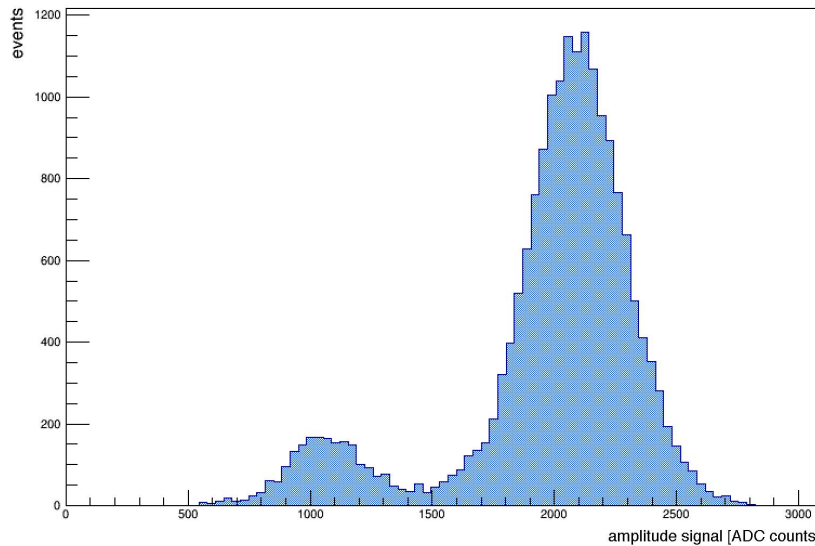


Figure 3.21: Pulse-height distribution of SWPC2 with a gas mixture of *Ar/CO₂* (70/30) and a gas flow equal to (1.0 ± 0.3) *l/h*, equivalent to about 6 *volume/h*. The applied voltage is (2025 ± 7) V.

The ^{55}Fe decays into ^{55}Mg emitting photons with energy of about 5.9 keV , so the photoelectric effect with the matter is predominant. In the pulse-height distribution of SWPCs, shown in figure 3.21, the main peak is caused by the 5.9 keV photons whereas the smaller one is due to the de-excitation of argon atoms (also called argon escape peak ²). The measured mean value of the ^{55}Fe peak (in ADC counts) is proportional to the detector gain.

Before the installation at GIF++, the SWPCs were monitored for about one month in the laboratory to be sure that no ageing phenomena occurred. Figure 3.22 shows the normalized gain of the SWPC1 and SWPC2 from 11th May 2016 to 7th June 2016. The gain is normalized with respect to the first value. Error bars are not plotted in order to distinguish the fluctuations of gain of both detectors. In any case, the order of magnitude of the errors for all measurements in figure 3.22 is 10^{-1} . The measurements in figure 3.22 are not corrected for temperature and pressure variations.

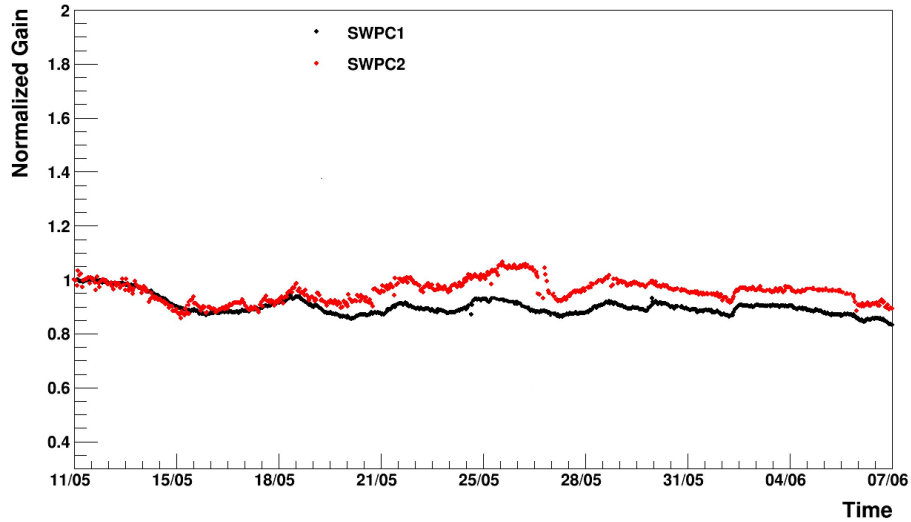


Figure 3.22: Normalized gain for SWPC1 and SWPC2 measured for about one month. The measurements are not corrected for temperature and pressure variations. The order of magnitude of the errors for all measurements is 10^{-1} , but the error bars are not plotted in order to distinguish the fluctuations of gain for both detectors.

The temperature of the laboratory, where the test has been carried out, was at about $21\text{ }^{\circ}\text{C}$ ³, whereas the internal pressure is affected by variations of the atmospheric

²When the incoming photon has an energy greater than the absorption edge of argon, the atom can be ionized. After the ionization of the argon atom, the photon emitted by the de-excitation has energy equal to about 3 keV [22]. If the photon interacts with another argon atom, a further electron from an outer shell is extracted. The escape peak in the pulse-height distribution is due to this secondary process. In case the photon, emitted by de-excitation, does not interact with a second argon atom, only the electron of first ionization will produce a proportional signal in the detector: this fact explains why the height of the argon escape peak is lower than the main peak.

³Maximum fluctuation of $3\text{ }^{\circ}\text{C}$ occurred during the measurements.

pressure. A correlation between the gain of SWPC1 and the atmospheric pressure is shown in figure 3.23: the increasing of the atmospheric pressure involves a decreasing of the gain. The same correlation has been observed also in the SWPC2. Indeed at constant temperature, a 1% pressure increase results generally in a gain reduction of about 5-10% [8]. In figure 3.23 measurements of atmospheric pressure are taken by a

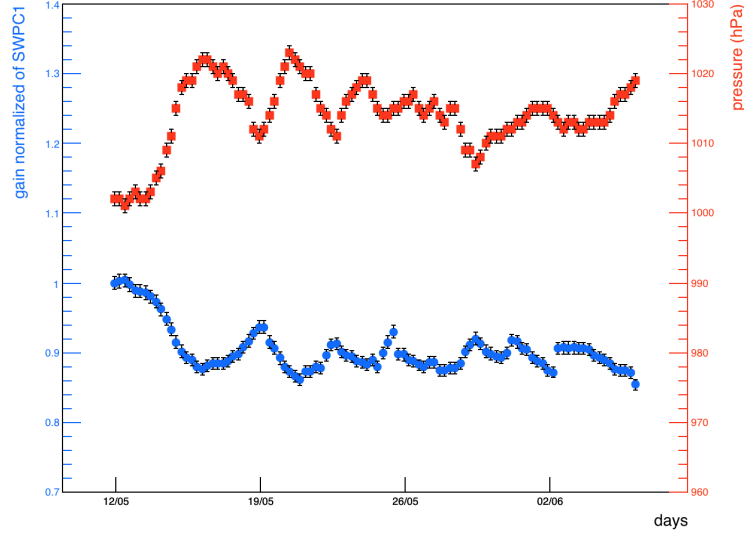


Figure 3.23: Measurements of the gain and atmospheric pressure every six hours. The error of normalized gain is calculated through the standard error of the mean. A correlation between the performance of SWPC1 and the pressure can be observed.

weather station.

The dependence of the gain of gaseous detectors on the temperature and atmosphere pressure is well known [17]. Figure 3.24 shows the dependence of gain on temperature and pressure for the SWPC1, which is in open mode at GIF++.

The experimental data are fitted by an exponential function, in order to deduce the parameters for the correction. The correction formula is:

$$G_c \left(\frac{T}{P} \right) = G \left(\frac{T}{P} \right) e^{A \left(\frac{T_0}{P_0} - \frac{T}{P} \right)} \quad (3.8)$$

where G is the gain of the detector, which depends on temperature (T) and atmospheric pressure (P), G_c is the corrected gain, T_0 and P_0 are assumed to be an average value of temperature and pressure respectively (in this case, $T_0 = 294.5 \text{ K}$ and $P_0 = 970 \text{ hPa}$) and A is the slope of the fitting exponential function in hPa/K . The exponential dependence in the correction is deduced by assuming the inverse

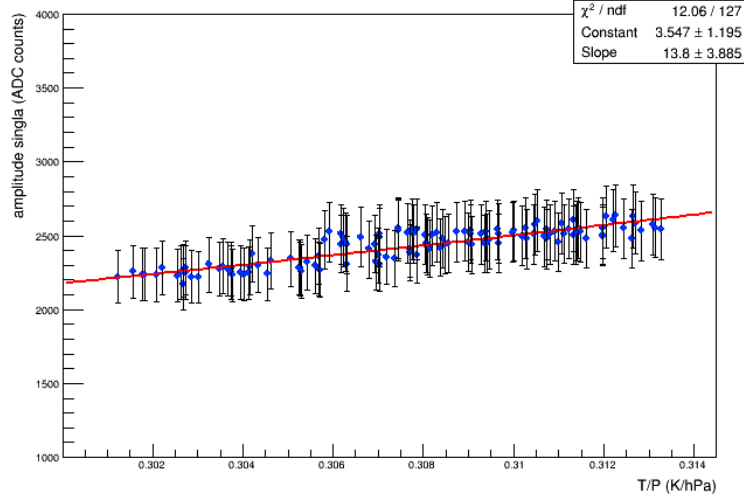


Figure 3.24: Dependence of gain on temperature and pressure in Ar/CO_2 (70/30) for SWPC1, installed at GIF++.

proportionality of the first Townsend coefficient (α) to the mass density (ρ) of the gas [23]:

$$\alpha \propto \frac{1}{\rho} \propto \frac{T}{P} \quad (3.9)$$

Figure 3.25 shows the corrected and not corrected gain of SWPC1. The gain has been corrected for temperature and pressure variations using the parameter of the fit, shown in figure 3.24; indeed the correction is carried out in order to remove this dependence. Corrected values of gain result to be flat as function of the ratio between temperature and atmospheric pressure.

Triple-GEM detector

The GEM detector has been characterized in laboratory in Ar/CO_2 (70/30) before the installation at GIF++. The characterization is done with a radioactive source of ^{55}Fe and activity of about 1.2 MBq.

Figure 3.26 shows the pulse-height distribution when the radioactive source is placed on the middle of the window, the applied voltage is 3525 V and the gas flow is about 1 l/h (equivalent to about 4 volume/h).

The pulse-height distribution presents a main peak, due to the photons emitted by ^{55}Fe , and an argon escape peak, as seen in the previous paragraph. The same data analysis for the SWPCs concerning the waveforms and pulse-height distribution is

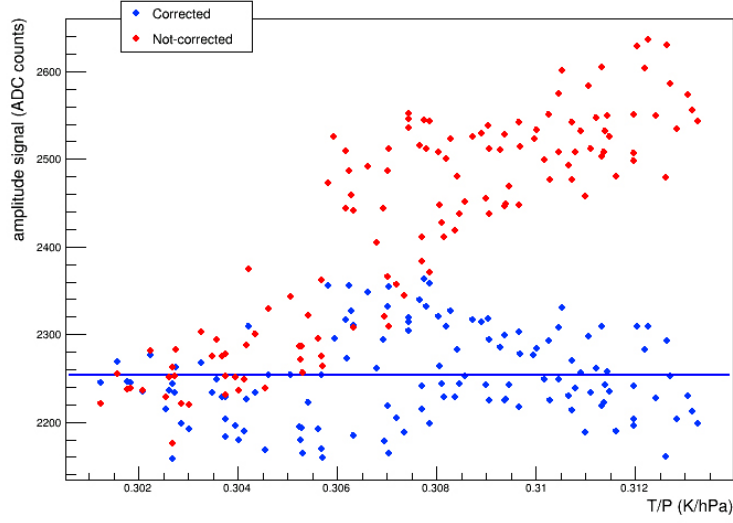


Figure 3.25: Amplitude signal without correction (in red) and with correction (in blue) of temperature (in the gas rack) and atmosphere pressure for SWPC1. On the contrary the figure 3.24, in this plot the error bars are not shown in order to see better the effect of correction. The average value of corrected gain is (2254 ± 5) ADC counts.

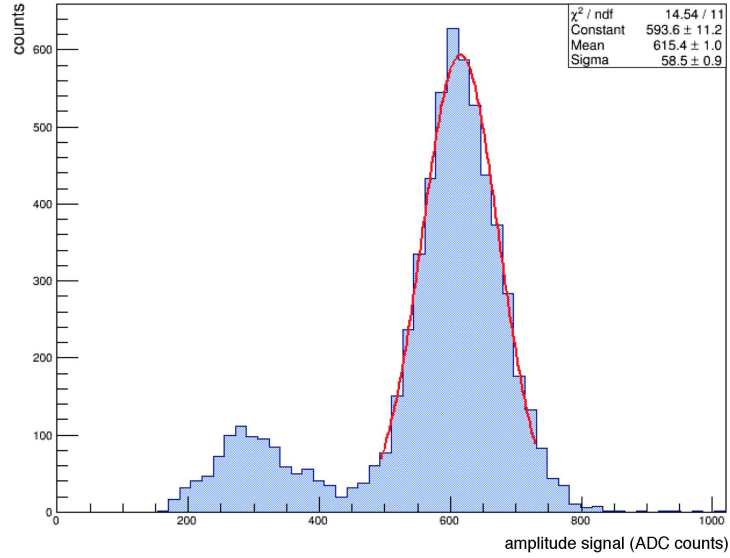


Figure 3.26: Pulse-height distribution when the ^{55}Fe source is placed on the middle of the GEM window and the applied voltage is set to 3525 V. The gas mixture is Ar/CO_2 (70/30). The output signals are acquired for 120 s. The fit is done with a Gaussian function and the value of chi-squared test is equal to 14.54 with eleven degrees of freedom.

also used for the GEM detector.

Figure 3.27 shows the dependence of the gain and the acquisition rate as function of the applied voltage.

The gain is an exponential function of the applied voltage. The rate of acquisition

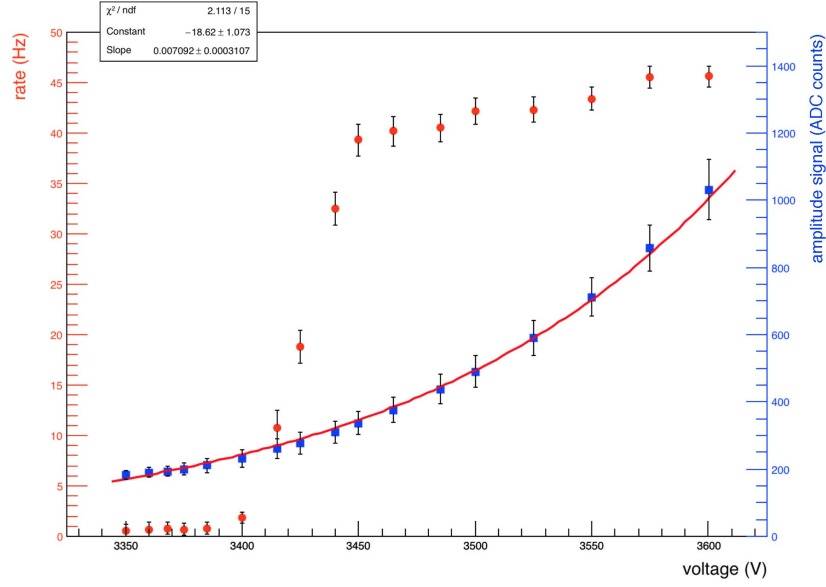


Figure 3.27: The gain of the triple-GEM detector and the acquisition rate as function of applied voltage. The gain of the detector is an exponential function depending on the applied voltage. The data for each measurement is taken for 120 s and the trigger threshold is set to 8300 ADC counts.

goes up rapidly from 3400 V to 3450 V, then it becomes flat with values between 40 Hz and 45 Hz. The plateau in the acquisition rate is caused by the achievement of the total efficiency of GEM detector to the incoming photons. The working point should not be selected close to the knee in order to avoid a decreasing of the performance, due to possible fluctuations of applied voltage. Whereas a value of applied voltage too high involves larger avalanches in the detector, which might shorten the lifetime. Therefore the selected voltage for the operational of the GEM detector is 3500 V.

The radioactive source was moved over the surface for a uniformity scan of GEM detector. Figure 3.28 shows the mean value of ^{55}Fe peak in the pulse-height distribution for the sixteen squares, in which the surface of the detector has been divided. The GEM detector has a uniform gain on the total surface with fluctuations smaller than 30%.

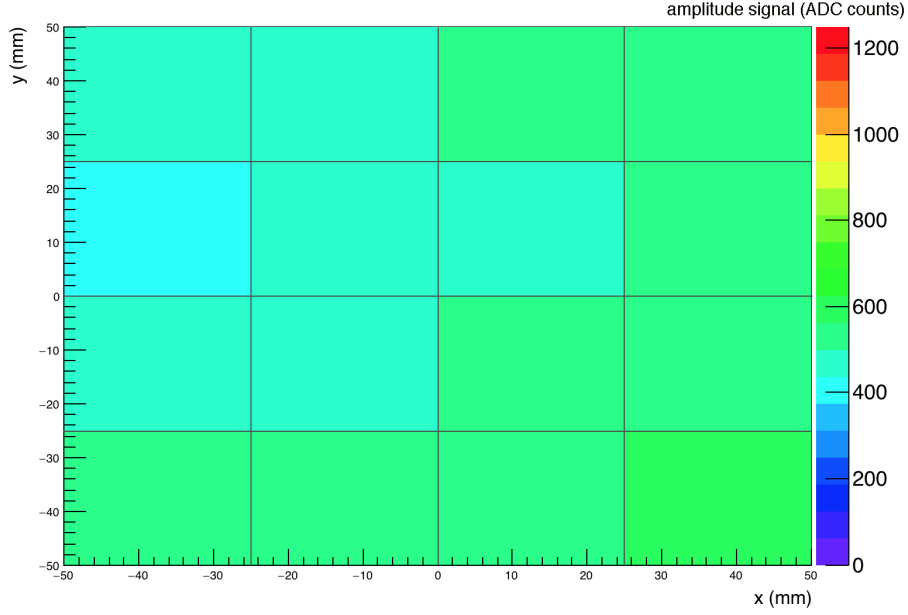


Figure 3.28: The plot shows the mean value of ^{55}Fe peak in the pulse-height distribution for sixteen different positions over the detector surface. The applied voltage has been set equal to 3500 V during the scan, while the data for each square is taken for 120 s.

3.6 Performance of detectors at GIF++

3.6.1 Interaction of photons with matter

From low photon energies up to a few tens of keV, the dominant interaction process of photons in the detector is the photoelectric effect, resulting in the release of a free electron. The gas mixture and the materials of detector become gradually more transparent at photon energies greater than a few tens of keV [8]. Indeed, towards higher energies, the photon absorption is gradually dominated by Compton scattering, up to energy equal to 1.02 MeV; when the photon energy is twice the mass of the electron, the process of pair production becomes the dominant one. For instance, figure 3.29 shows the photon absorption cross section for argon [22].

Photons, emitted by ^{55}Fe source, interact mainly with the GEM detector through photoelectric process, whereas the photons from ^{137}Cs source have an energy greater than about two orders of magnitude, so the dominant process is the Compton scattering.

3.6.2 Measurements under irradiation of ^{137}Cs source

After the installation of experimental setup at GIF++, the characterization of triple-GEM has been carried out under irradiation of ^{137}Cs and ^{55}Fe sources. The gas

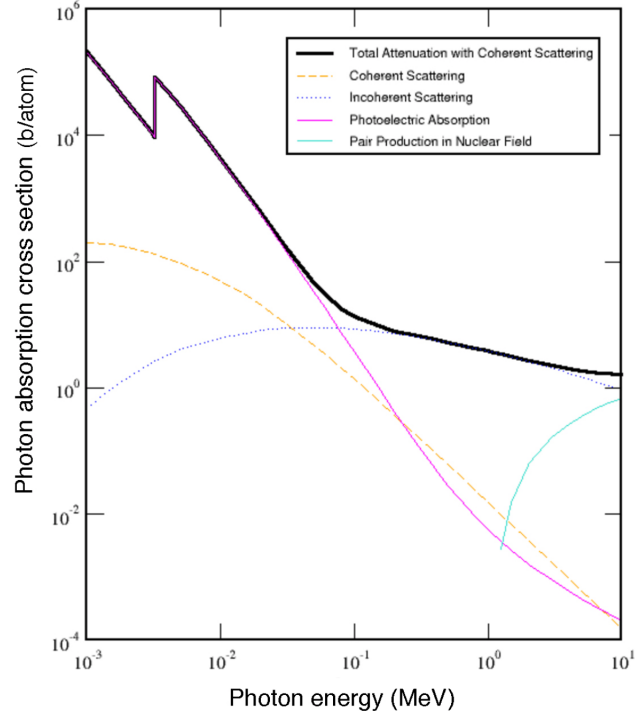


Figure 3.29: Total photon absorption cross section in argon. In figure there are also shown the cross sections of photoelectric absorption, Compton scattering and pair production process [22].

mixture is Ar/CO_2 (70/30) and the detectors are in open mode.

The current of triple-GEM detector depending on voltage has been measured, as shown in figure 3.30. The measurements have been taken with two different attenuation factors. The value of voltage equal to 3500 V has been selected for the operation of triple-GEM in Ar/CO_2 .

The installation of purifier module requires the regeneration of cartridges, as first step. After the regeneration, the cartridges are usually filled up with Ar or CO_2 , in order to avoid infiltrations of air. In this case, the cartridges were filled up with Ar . After the installation (on 21st July 2016) and the opening of cartridges, a contamination in the gas mixture occurred into the gas system. Indeed in figure 3.31 the current-voltage curve of triple-GEM is shifted as result of this contamination. The measurements have been taken at the same environmental conditions: temperature equal to about 21 °C ⁴ and atmospheric pressure equal to about 1026 hPa ⁵.

After eight days from the installation (with a flow equal to 5.5 l/h in input and 3.5 l/h

⁴The maximum fluctuation has been equal to 1 °C.

⁵The maximum fluctuation was equal to 2 hPa.

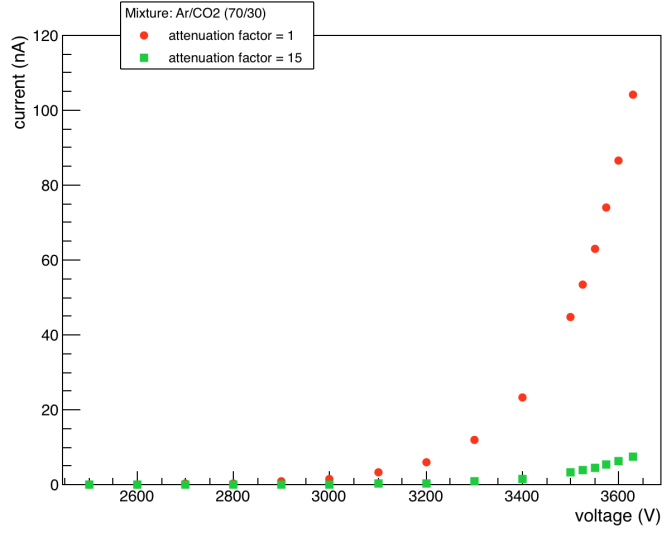


Figure 3.30: Values of current depending on voltage under irradiation of ^{137}Cs source and ^{55}Fe source at different attenuation factors. The error bars are hidden by markers.

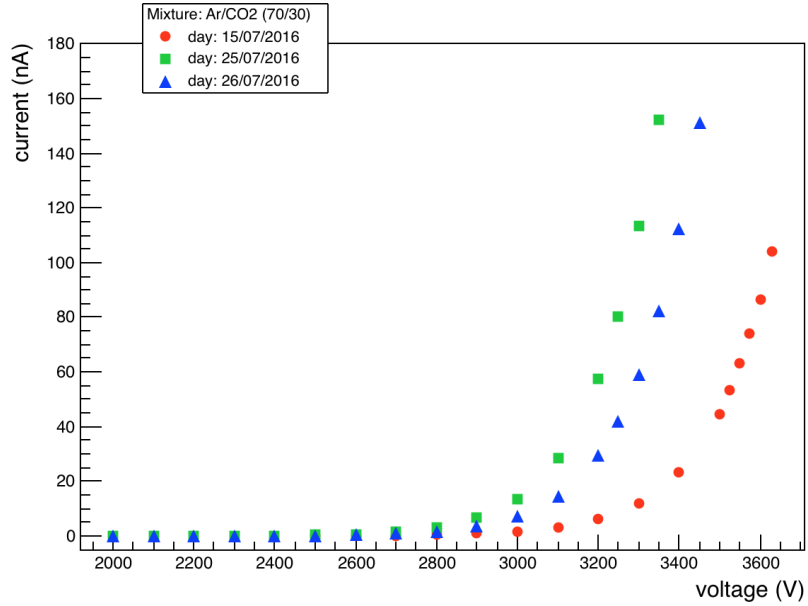


Figure 3.31: Current of triple-GEM depending on voltage under irradiation of ^{137}Cs source. The shift of the current-voltage curve occurred after the installation of cartridges in the gas system, due to a contamination in the gas system. Every measurement has been taken at the same environmental conditions: temperature equal to $21\text{ }^{\circ}\text{C}$ and atmosphere pressure equal to 1026 hPa .

for GEM detector and SWPC2, equivalent to about 14 volume/h and 20 volume/h respectively), the current-voltage curve is returned to the values, measured before the installation of cartridges, with good approximation.

The pulse-height distribution of signals from triple-GEM is shown in figure 3.32 when no filter is used to shield the ^{137}Cs source.

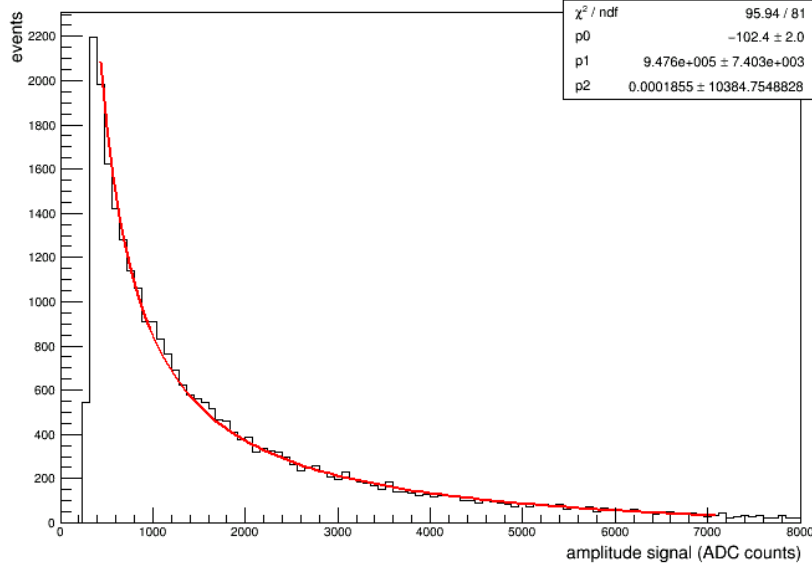


Figure 3.32: The pulse-height distribution of signals from triple-GEM, when it is under irradiation of ^{55}Fe and ^{137}Cs sources with no attenuation factor. The distribution can be properly fitted by a function with three coefficients.

Due to the much higher activity of ^{137}Cs source in comparison to the ^{55}Fe source, the ^{55}Fe peak is not visible in the pulse-height distribution. The pulse-height distribution can be properly fitted by the following formula:

$$y = p_0 + \frac{p_1}{x} + \frac{p_2}{x^2} \quad (3.10)$$

where x is the value in abscissa concerning the amplitude signal and y is the number of events.

For a complete characterization of the experimental setup at GIF++, a filter scan has been carried out. During the filter scan, the measurements have been taken in a short time period in order to have the possibility to compare the data at the same environmental conditions. Indeed a variation of environmental parameters, such as atmosphere pressure, temperature, humidity and so on, may induce variations in the measurements. Figure 3.33 shows the pulse-height distribution when the ^{137}Cs source is not shielded (attenuation filter equal to 1) and when it is shielded by an attenuation filter equal to 46000.

When the filter is equal to 46000, the reduction of photon flux, coming from the

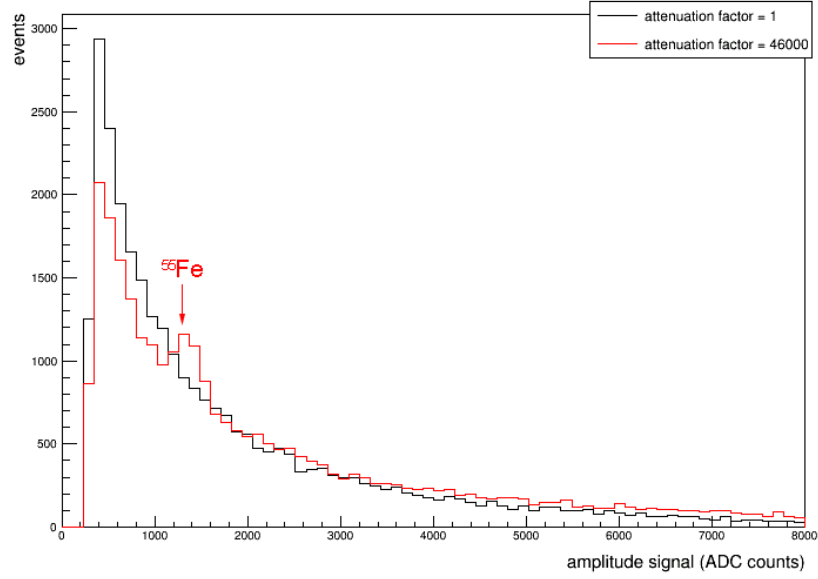


Figure 3.33: The pulse-height distribution when the ^{137}Cs source is not shielded (attenuation factor equal to 1) and when it is shielded by an attenuation factor equal to 46000. The data acquisitions to get the pulse-height distributions are lasted 10 seconds, while the acquisition rate was about 10^3 Hz for both attenuation factors.

irradiator, allows the individuation of ^{55}Fe peak at about 1350 ADC counts in the pulse-height distribution. Just after the acquisition of pulse-height distribution under irradiation, a second data acquisition was carried out with only the ^{55}Fe source in order to check if the peak is effectively produced by photons at 5.9 keV . Figure 3.34 shows the ^{55}Fe peak at (1280 ± 140) ADC counts when the ^{137}Cs source is completely shielded.

As shown in figure 3.32, there is no peak in the pulse-height distribution of triple-GEM detector induced by ^{137}Cs source in the normal operation conditions of GIF++, so the monitoring of gain for the GEM detector is performed with:

- the measurement of current from detector when it is under irradiation of ^{137}Cs source (every hour);
- the acquisition of the signals, induced by ^{55}Fe source in the detector, when the ^{137}Cs is completely shielded (2-3 times for week).

The procedure of test on triple-GEM detectors has been validated for the long-term operation.

During the characterization of triple-GEM detector at GIF++, a fluctuation of the current has been observed: this variation is strongly depended on the performance of the gas recirculation system, in particular the temperature outside the bunker has

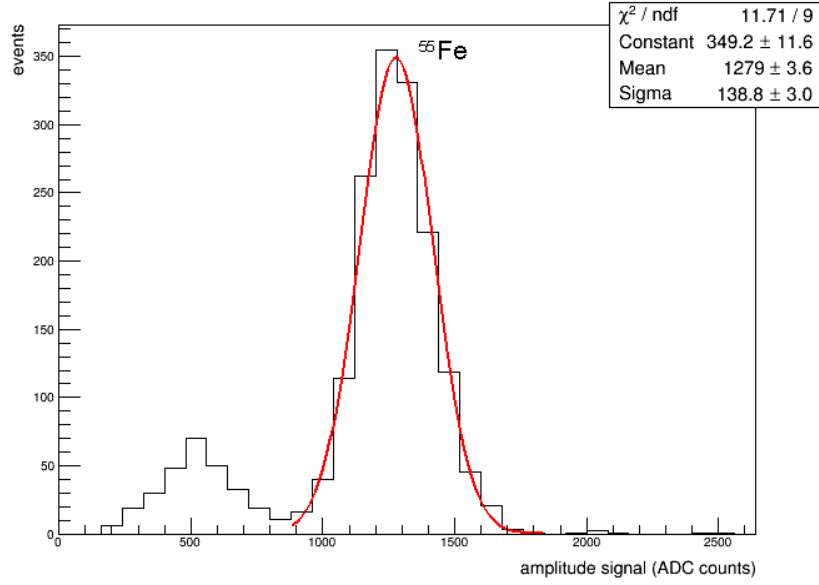


Figure 3.34: The pulse-height distribution when the ^{137}Cs source is completely shielded, so the peak is only due to the presence of ^{55}Fe source. The data acquisition of the pulse-height distribution is lasted 120 seconds.

been identified as main responsible. The temperature inside the bunker is constant and equal to $(21.5 \pm 0.5) ^\circ\text{C}$, thanks to air conditioning system, while the temperature outside bunker depends on the environmental temperature. Figure 3.35 shows the current of triple-GEM detector together with the ambient temperature outside bunker.

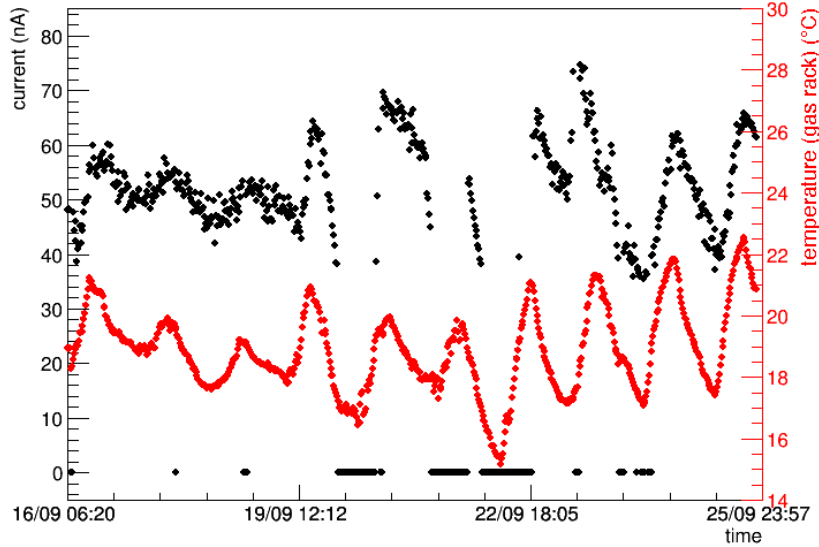


Figure 3.35: Current of triple-GEM detector under irradiation with ^{137}Cs source depends on the environmental temperature. If the temperature of gas rack changes, the current follows the same trend as well.

The trend of current could be caused by the fact that the gas mixture with same temperature of the gas rack, coming into the bunker, has not enough time to exchange heat and reach the constant temperature inside bunker; so the different conditions of gas mixture during the day induces different performance in the triple-GEM. The correction for the temperature and pressure variations of the current from triple-GEM is not sufficient for a precise monitoring of the gain, especially when the gradient of temperature is larger.

3.6.3 Gas chromatography for gas mixture

The working principles of the gas chromatograph at GIF++ and the tuning of parameters with air sample are presented in *appendix C*. After the calibration for each gas of interest, some analysis of Ar/CO_2 (70/30) has been carried out to check if the concentration of CO_2 is equal to the one selected by MFCs. Moreover the concentrations of pollutants have been evaluated in the gas mixture at about 85% as recirculation fraction.

Figure 3.36 shows the gas chromatogram of Ar and CO_2 in the PPU column. The concentration of Ar is so high that the response of TCD devices is not reliable, while the concentration of CO_2 is $(30.0 \pm 0.4)\%$.

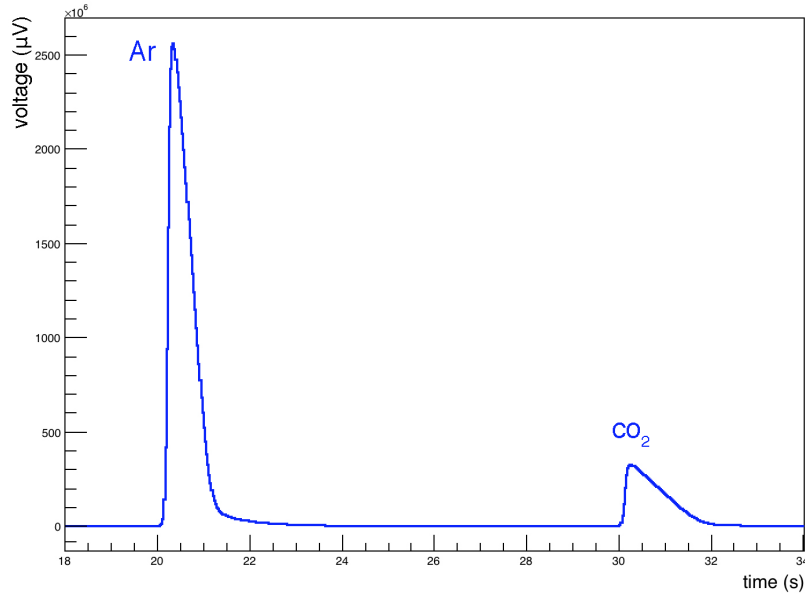


Figure 3.36: Gas chromatogram of Ar and CO_2 in the PPU column at $75\text{ }^{\circ}C$. The concentration of CO_2 is equal to $(30.0 \pm 0.4)\%$

Figure 3.37 shows the gas chromatogram of air in the MolSieve column. The concentration of O_2 is $(490 \pm 60)\text{ ppm}$, while the N_2 is equal to $(2700 \pm 300)\text{ ppm}$.

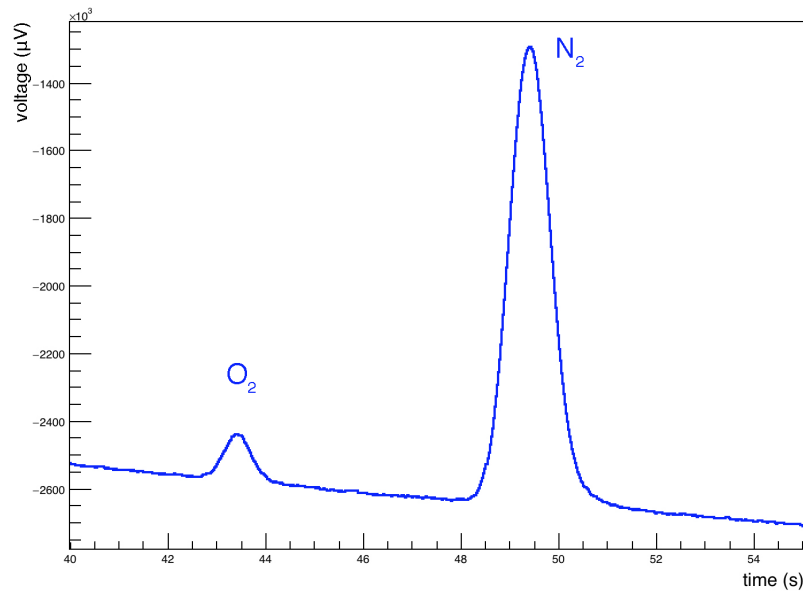


Figure 3.37: Gas chromatogram of air pollutants in the MolSieve column at 115 °C. The concentration of O_2 is (490 ± 60) ppm, while the N_2 is equal to (2700 ± 300) ppm.

During the ageing test at GIF++, the gas chromatography could represent a powerful technique of analysis to check the quality of gas mixture purification, achieved by the purifier module. Since concentrations of pollutants and impurities can be monitored.

Chapter 4

Simulation of triple-GEM detector with different gas mixtures

4.1 Implementation of triple-GEM detector with ANSYS and GARFIELD

A simulation of the triple-GEM detector under test at GIF++ has been carried out with software ANSYS and GARFIELD++. The simulation is focused on the understanding of drift and diffusion of electrons in two different gas mixtures (Ar/CO_2 and $Ar/CO_2/CF_4$) under the effect of electric field in a triple-GEM detector. Moreover the simulation has been performed in order to try to understand the contribution of typical pollutants in the gas mixture and compute triple-GEM performance for different concentrations of pollutants. The simulation data have been compared with experimental results.

The ANSYS software (version APDL) is a powerful simulation tool for finite element analysis: it is usually used for electromagnetic studies, stability and deformation of structures, fluid dynamics, heat transfer, etc. For the simulation of a triple-GEM, ANSYS is used to design the geometry of detector, set the boundary conditions and optimize the mesh of the structure for the calculation of potential in each finite element.

The simulation of drift and diffusion proprieties in gas mixtures and the computation of electron avalanches in the detector are carried out with GARFIELD++ software, since it is optimized for detailed simulations of particle detectors, which use a gas mixture as sensitive medium.

4.1.1 Geometry of triple-GEM detector with ANSYS

The calculation of the electric field inside a triple-GEM is a complicated problem, due to the complex structure of the detector and the high number of boundary conditions. ANSYS exploits the finite element method (FEM) to subdivide the geometry into small elements in order to simplify the problem and find approximate solutions. There are several techniques to divide the structure of the detector in finite elements: the method *SOLID123* with 10 nodes per element has been used for the simulation. With this method, each element is made up of a quadric curved tetrahedron, which adapts well to round surfaces. Indeed the bi-conical shape of holes, shown in figure 4.1, in a GEM foil is a complex problem for a proper mesh and the feature of ANSYS to divide the total structure in elements with ten nodes represents a good solution.

The drawing of the geometry is based on the repetition of a single hole for a GEM foil. Figure 4.1 shows the vertical cross section of the hole. The main part is in Kapton with thickness of $50\ \mu\text{m}$, while the upper and lower parts are in copper. The dimensions are the same of the triple-GEM under test at GIF++.

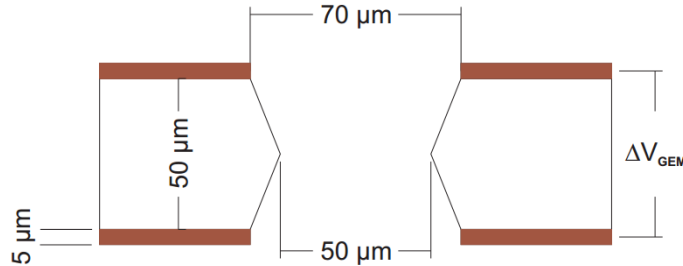


Figure 4.1: Vertical cross section of a single hole. The dimensions, used to draw the geometry in ANSYS, are the same of the triple-GEM under test at GIF++.

Since the structure of a GEM foil is periodic, only the basic cell of the geometry has been drawn and then its repetition is applied to cover the whole problem domain. This simulation takes into account GEM foils with fixed thickness and infinite dimensions in the other two axes. Figure 4.2 shows a 3D view of the basic cell for a single GEM foil. The arrangement of the holes follows a rectangular pattern with a pitch of $140\ \mu\text{m}$.

The basic cell is repeated three times along the z-axis and two electrodes in copper are added to create the complete vertical cell of a triple-GEM detector. The

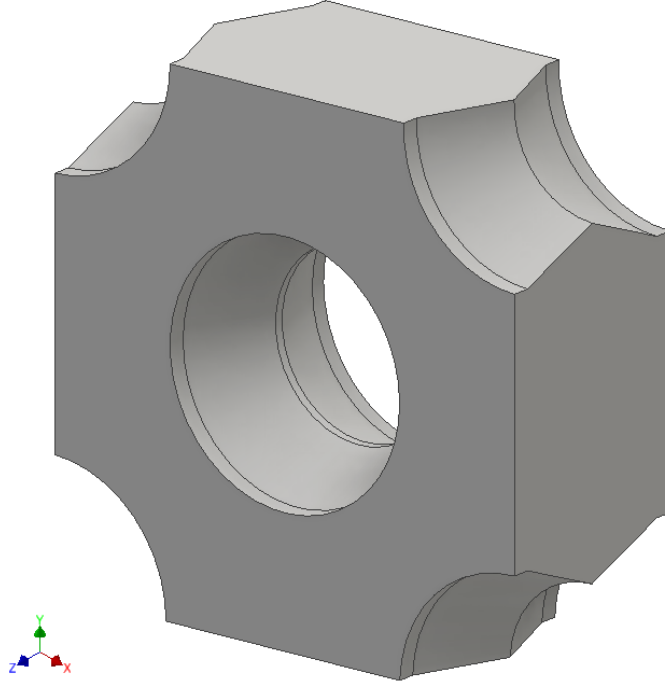


Figure 4.2: 3D view of the basic cell for a single GEM foil. The rectangular pattern of the holes is achieved with the repetition of the basic cell along x-axis and y-axis. The length of the diagonal from corner to corner is $280\ \mu m$, in order to have a pitch of holes equal to $140\ \mu m$.

electrodes in copper are the anode and cathode of the detector, whereas the repetition of basic cell, shown in figure 4.2, lets to draw the three GEM foils and space out them with the drift region (placed from $-4.065\ mm$ to $-1.065\ mm$ on z-axis), the two gap regions (from $-1.005\ mm$ to $-0.005\ mm$ and from $0.055\ mm$ to $2.055\ mm$ respectively) and the induction region (from $2.115\ mm$ to $3.115\ mm$ on z-axis). The thicknesses of each region, filled by the gas mixture, are the same of the triple-GEM at GIF++:

- drift region: $3\ mm$;
- first gap region: $1\ mm$;
- second gap region: $2\ mm$;
- induction region: $1\ mm$.

Figure 4.3 shows a schematic view of the structure of triple-GEM detector under test at GIF++. The only differences in the geometry between the drawing and the real detector are:

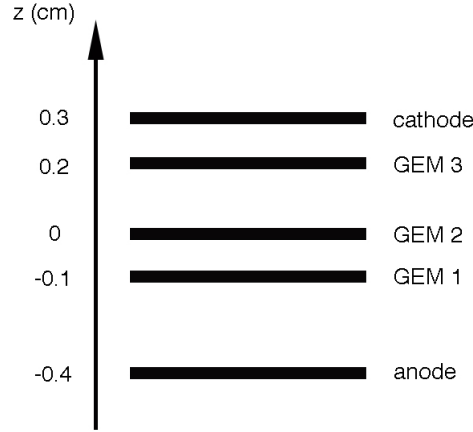


Figure 4.3: Schematic view of the structure of triple-GEM detector under test at GIF++.

- The alignment of the symmetric axis of the holes in the drawing, even though it is not guaranteed in the real geometry of course. Due to the big dimensions of regions for the gas volume in comparison to the dimensions of the holes, this particular alignment does not affect the truthfulness of simulation;
- The effects of the edges are not taken into account during the simulation because the vertical cell in ANSYS is repeated to infinity. The dimensions of the triple-GEM detector ($10\text{ cm} \times 10\text{ cm}$) are bigger in comparison to the extension of the electron avalanches that possible effects can be considered negligible.

After the implementation of the geometry, the materials for each volume are chosen and the boundary conditions have been set. The working high voltage for a triple-GEM operated with Ar/CO_2 (70/30) is -3500 V , while the operational voltage for the gas mixture $Ar/CO_2/CF_4$ (45/15/40) is selected equal to -4500 V . The values of voltages have been obtained by previous experimental studies in laboratory and used for the simulation in this thesis as well [21]. In accordance with resistors' values of the voltage divider, described in the paragraph 3.2.1, the voltages for each conducting component in copper, placed on the extremities of single GEM foils, are set. Figure 4.4 shows the commands in ANSYS to set the voltage boundary conditions in presence of 70% Ar and 30% CO_2 .

After drawing the geometry of the detector in ANSYS and setting the voltage boundary conditions, particular attention has been paid to the mesh, because there is a order of magnitude between the extension along x-axis and y-axis of the vertical cell

```

! Electrode placed at - 4.065 mm
! select volume 8
VSEL, S, VOLU, , 8
! select all surfaces of selected volume 8
ASLV, S
! set voltage equal to - 3092 V to selection
DA, ALL, VOLT, -3092

! GEM-1 foil: up
VSEL, S, VOLU, , 3
ASLV, S
DA, ALL, VOLT, -2411

! GEM-1 foil: down
VSEL, S, VOLU, , 7
ASLV, S
DA, ALL, VOLT, -2037

! GEM-2 foil: up
VSEL, S, VOLU, , 1
ASLV, S
DA, ALL, VOLT, -1662

! GEM-2 foil: down
VSEL, S, VOLU, , 5
ASLV, S
DA, ALL, VOLT, -1322

! GEM-3 foil: up
VSEL, S, VOLU, , 2
ASLV, S
DA, ALL, VOLT, -641

! GEM-3 foil: down
VSEL, S, VOLU, , 6
ASLV, S
DA, ALL, VOLT, -341

! ground: electrode placed at + 3.115 mm
VSEL, S, VOLU, , 9
ASLV, S
DA, ALL, VOLT, 0

```

Figure 4.4: Commands for ANSYS (APDL version) to set the voltage boundary conditions for the simulation of a triple-GEM when the gas mixture is 70% *Ar* and 30% *CO₂*.

and the one along z-axis are different: the vertical cell has size equal to 140 μm in the x-axis and y-axis, while the total thickness is about 7 mm. Indeed it is important to select a fine meshing close to the GEM foils to be sure that surfaces are correctly modelled. Figure 4.5 shows the mesh of the vertical unit in ANSYS, whereas figure 4.6 is a zoom on the mesh close to the holes.

The outputs of ANSYS are four files (.lis) with the following information:

- list of elements, which contains the list of nodes belonging to each element and the material contained in it;

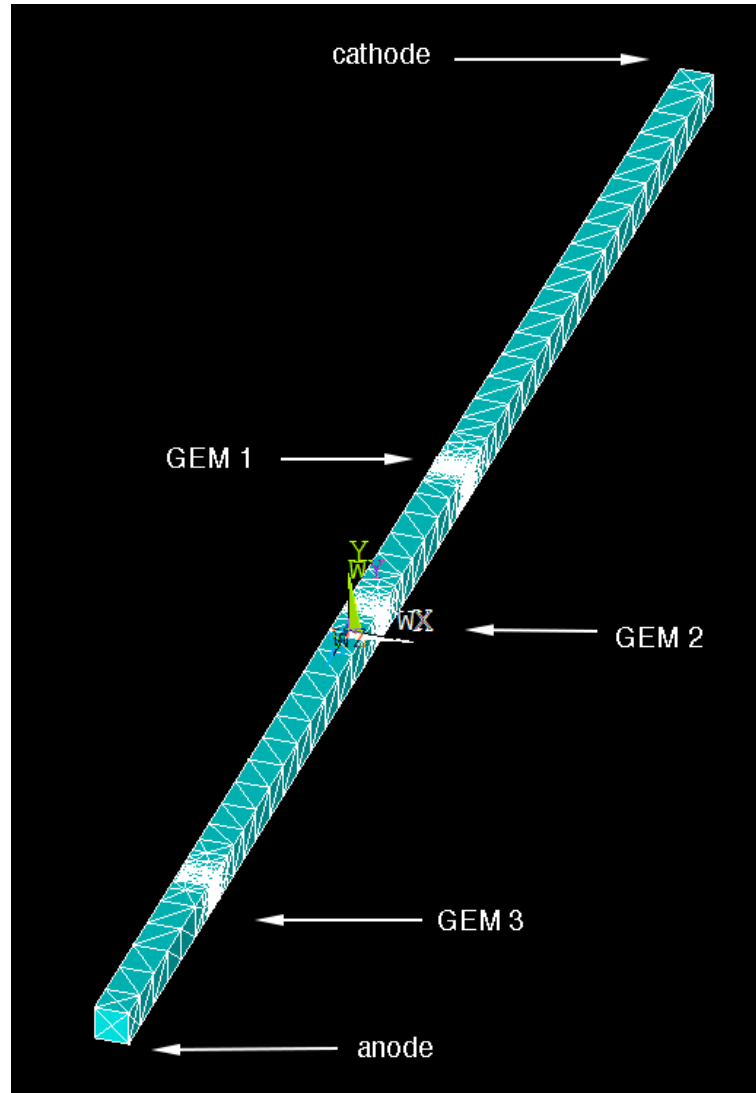


Figure 4.5: Mesh of the vertical unit performed by ANSYS. The method selected for the mesh is SOLID123, so each element is made up of ten nodes and it is optimized to model correctly round shapes, like the holes of a GEM foil.

- list of nodes with the coordinates;
- list of materials, with the value of dielectric constant and conductivity;
- list of node potentials.

These four files are usually the input for GARFIELD software in order to calculate the electric field inside the detector and then the drift and diffusion of electrons in the gas mixture.

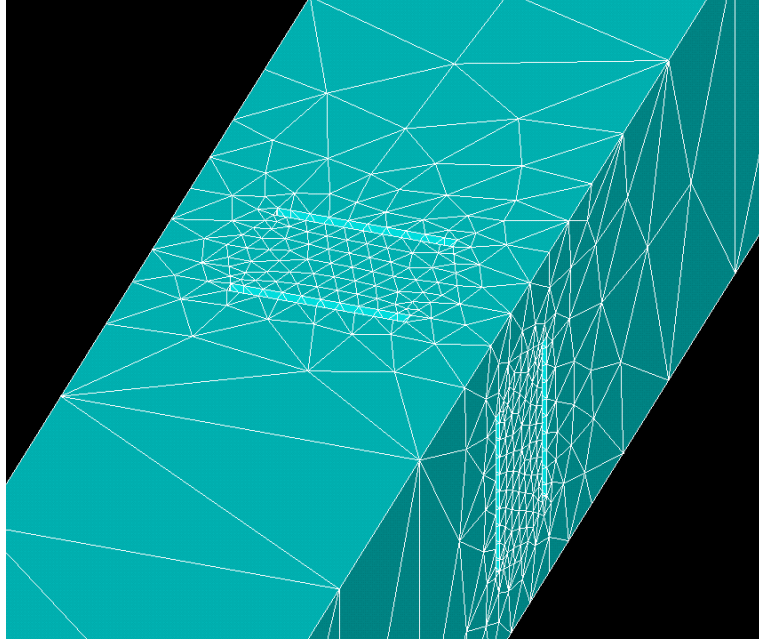


Figure 4.6: Zoom on the external edges of the vertical unit, where the mesh of a single GEM foil is finer. Since the dimensions along x-axis and y-axis are much smaller than the thickness of triple-GEM, it is necessary to decrease the sizes of each element close to the GEM foils for modelling correctly the surface of the holes and the components in copper.

4.1.2 Calculation of electric field in a GEM detector with GARFIELD

The calculation of electric field is performed with the GARFIELD software and the output of finite element analysis from ANSYS is used to compute the electric field map in the three-dimensional structure of the triple-GEM. In the code, based on C++, it is necessary to load the files with the mesh, the nodal solution and the material properties, through the initialisation of function *ComponentAnsys123*. Afterwards the periodicity of the pattern is specified: in this case, the functions *EnableMirrorPeriodicityX* and *EnableMirrorPeriodicityY* have been used. Finally the electric field map can be calculated. For instance, figure 4.7 shows the electric field map in a single-GEM, calculated by GARFIELD. Results of the simulation, presented in this work, do not take into account the magnetic field. Every gas mixture has been simulated at normal temperature and pressure (NTP).

Most of the field lines from the upper side of GEM foil enter into the hole and exit on the lower side, while some of them end on the Kapton surface. These electric field lines lead to a deposition of electrons on the insulator material. This process, named charging up, finishes when the Kapton surface is saturated and lasts about

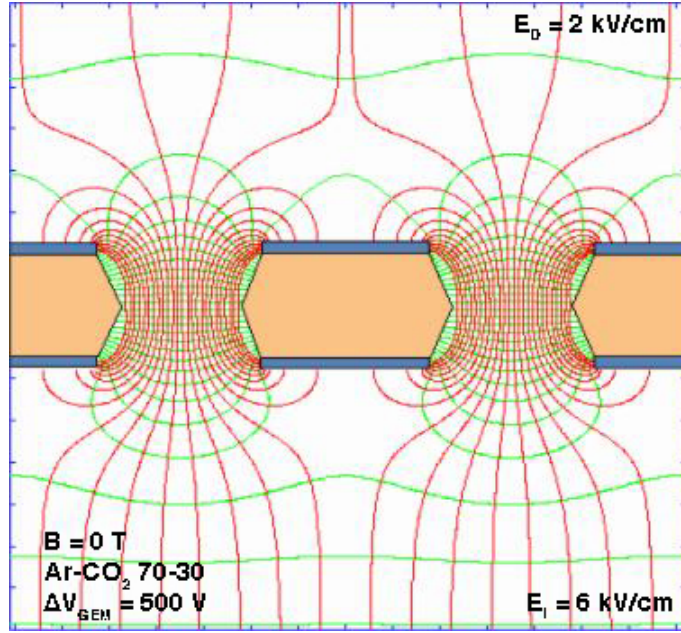


Figure 4.7: Electric field map in a single-GEM calculated by GARFIELD. The field lines are in red and equipotential lines in green. The magnetic field is equal to 0 T and the difference of voltages between the upper electrode and the lower one is 500 V [24].

few minutes since the voltage is applied to the foil. This deposit of negative charges on the inner surfaces increases the electric field inside holes and the gain of the GEM detector grows up to about 30%.

In this work, GARFIELD is used to simulate the electrons drifting and the growth of avalanches along the specific geometry of the triple-GEM. In general GARFIELD is also used for the tuning of parameters to increase the performance of the gaseous detectors or for the optimization of some specific features of detectors, as for example charge multiplication, cluster size and time resolution.

4.2 Simulation of electron avalanches in GEM detectors

4.2.1 Major processes in electron and gas mixture collisions

The physical processes in a gaseous detector begin with the release in the gas mixture of one or more electron-ion pairs, as explained in details above. The number and the distribution of the electron-ion pairs depend on the nature and energy of the incoming radiation. For a photon of energy 1 keV , the number of primary electron-ion pairs realised in *Ar* at NTP is equal to 1. For an electron of energy 100 keV the primary

pairs are about 1000 per centimeter, while a proton of energy 1 *GeV* releases about 25 *pairs/cm*.

When the electrons and ions are released in the gas mixture, they might neutralize by recombination or by collisions with the walls of detector, so it is necessary to apply an external electric field to separate and drift them towards the electrodes. The strength of electric field for separation depends on several parameters, like the primary ionization density and gases, but it is typically about a few tens of *V/cm* in *Ar* at NTP [8]. When a primary pair is separated, the electron and the ion diffuse locally in the gas volume, due to the effect of multiple collisions with surrounding molecules, and acquire the thermal energy of distribution of the medium, but this energy is not sufficient to produce an avalanche in the detector. In addition the charges move through the medium under the action of the external electric field. The motion of charges in the direction of the field is named as drift velocity.

Since the mass of electrons and ions is different, the drift velocity of ions increases almost linearly with the field, whereas for the electrons the dependence is more complex. Indeed at values of electric field greater than a few hundred *V/cm*, the drift velocity of electrons does not increase linearly with the field, but starts to saturate or decrease [8, 25]. By increasing the field strength, the electrons can acquire enough energy between two collisions to produce inelastic phenomena. Table 4.1 shows the major processes in electron and ion-molecule collisions.

Process	<i>initial state</i> \rightarrow <i>final state</i>
ionization	$A + e \rightarrow A^+ + e + e$
excitation	$A + e \rightarrow A^* + e$
de-excitation	$A^* + e \rightarrow A + e$
radiative recombination	$A^+ + e \rightarrow A + h\nu$
electron capture	$A + e \rightarrow A^-$
photo-emission	$A^* \rightarrow A + h\nu$
photo-ionization	$A + h\nu \rightarrow A^+ + e$
photo-excitation	$A + h\nu \rightarrow A^*$

Table 4.1: Major processes in electron and ion-molecule collisions. *A* indicates atom or molecule, *A** is their excited states and *A*⁺ or *A*[−] the corresponding ion. The noble gas atoms de-excite through photon emission, whereas polyatomic molecules have rotational and vibrational radiationless transitions [8].

At higher field (about tens of *kV/cm*), the probability of ionizing collisions increases and becomes greater than the probability of excitations. As shown in table 4.1, the ionization process produces an electron-ion pair, so the two electrons (the first electron

before the ionizing collision and the second one from the electron-ion pair) acquire sufficient energy from the high electric field to ionize further. Therefore, if the mean free path of ionizing collisions is smaller than the thickness of the gas layer, the ionization processes lead to a rapid growth of electron-ion avalanches. This mechanism is the base of signal amplification in the gaseous detectors.

With GARFIELD software, it is possible to reproduce the major processes between electrons and gas molecules, in order to simulate the growth of electron avalanches in the detectors. Moreover, in the GARFIELD software, the program MAGBOLTZ is used for the calculation of transport properties of electrons in gas mixtures. MAGBOLTZ includes a database of electron-molecule cross sections for a wide list of gases obtained by experimental results. The electron-molecule cross sections depend strongly on the energy of electrons. Moreover high values of the cross sections reduce the electron diffusion in the gas volume and increase the drift velocity. Figure 4.8 shows the electron-molecule cross sections for *Ar*. For noble gases, the cross section is elastic until the electrons reach the first excitation and ionization energy (above 10 eV).

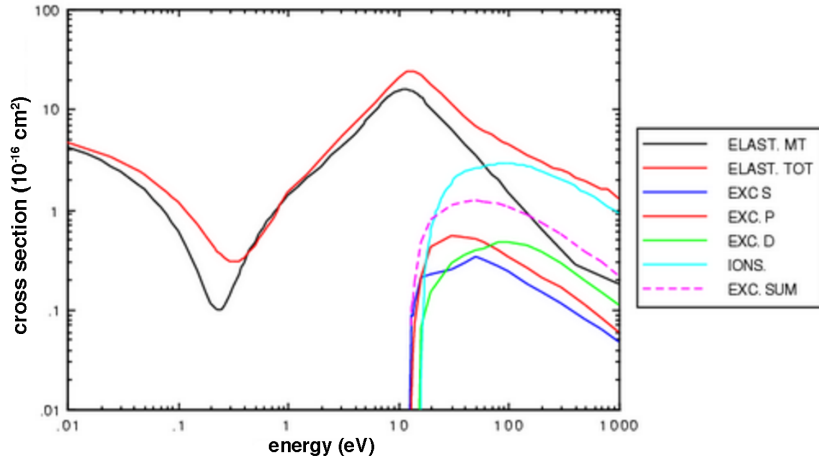


Figure 4.8: Electron-molecule cross sections for *Ar* at NTP (data from MAGBOLTZ database).

Whereas for the molecular gases, the vibrational and rotational cross sections are present at energies above 0.1 eV. As example, figure 4.9 shows the electron-molecule cross section for *CO*₂.

For electronegative gases, like *O*₂ and *CF*₄, the attachment cross section is really

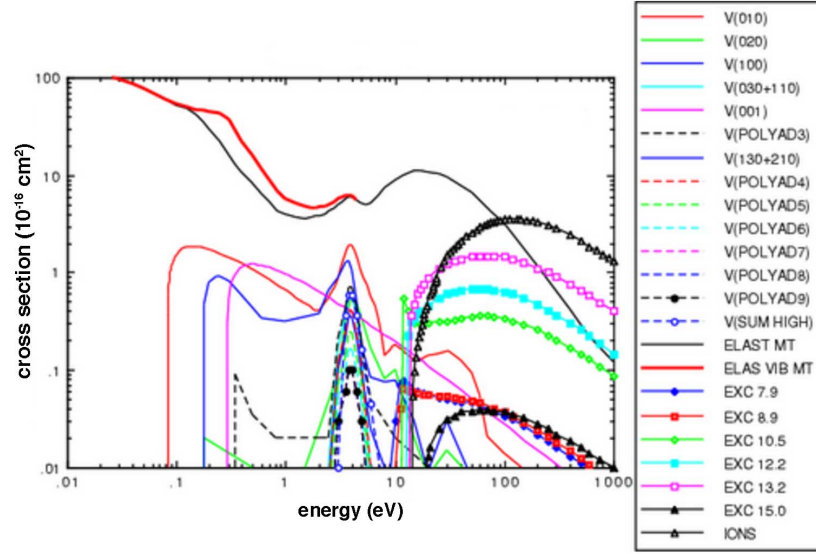


Figure 4.9: Electron-molecule cross sections for CO_2 at NTP (data from MAGBOLTZ database).

important to evaluate the capture of electrons drifting in the gas mixture. In the case of O_2 molecule, the peak of attachment cross section is between 0.05 eV and 0.1 eV (figure 4.10), while for the CF_4 the peak is at about 10 eV (figure 4.11). The large electron capture probability for the O_2 is at low values of electric field, while the electron losses for the CF_4 is only at high electric field.

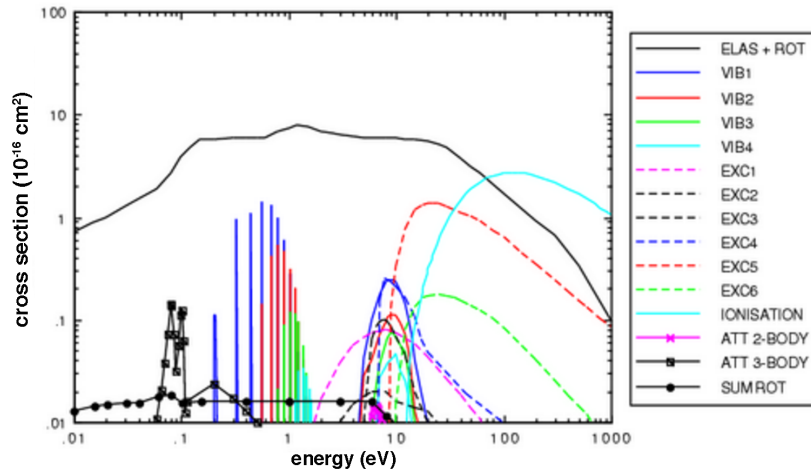


Figure 4.10: Electron-molecule cross section for O_2 at NTP (data from MAGBOLTZ database).

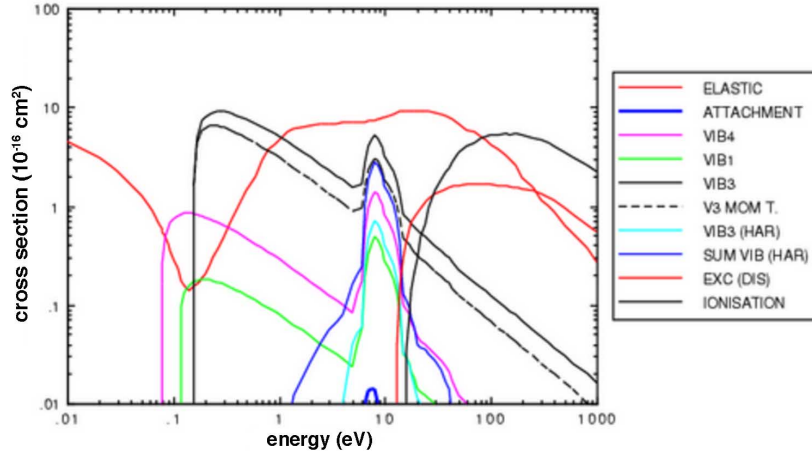


Figure 4.11: Electron-molecule cross section for CF_4 at NTP (data from MAGBOLTZ database).

The GARFIELD software allows also to use the program HEED to simulate the ionization pattern produced along the track of relativistic charged particles. Data analysis and graphic visualization of the results are obtained by the ROOT framework implemented in GARFIELD.

4.2.2 Simulation of single-GEM and triple-GEM

GARFIELD software has been used to simulate the electron avalanches in the GEM detectors.

Figure 4.12 shows the cross section of a hole in a single-GEM filled with 70% Ar and 30% CO_2 . Few electrons enter into the hole from the top where they gain enough energy, due to the high electric field, for several charge multiplication processes. The drift lines of electrons are in yellow while the drift lines of ions are in brown: some of them reach the upper electrode of GEM foil, generating the typical ion backflow. In GARFIELD the interactions of electrons with the gas mixture are plotted with dots in different colours: in case a process of ionization occurs, the atom of gas is marked in brown, for the excitation the colour is green and for the attachment it is blue.

Figure 4.13 shows the growth of an electron avalanche generated by a primary electron with initial position $(0, 0, -0.3)$ cm and energy of 0.1 eV, in the triple-GEM drawn in ANSYS. In this case, the gas mixture taken into account for the simulation is 45% Ar , 15% CO_2 and 40% CF_4 . The simulation has been carried out with the same boundary conditions shown in figure 4.4. As shown in figure 4.13, each GEM foil multiplies the number of incoming electrons, so the electron avalanche grows foil

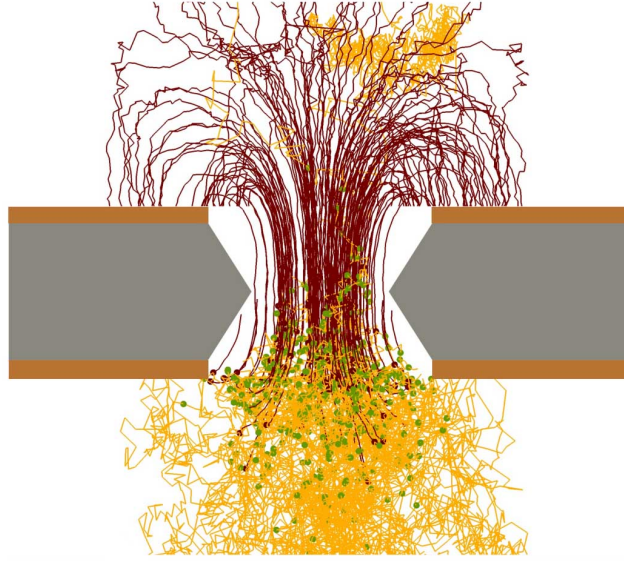


Figure 4.12: Cross section of a hole in a single-GEM with 70% Ar and 30% CO_2 . The voltage different between the extremities of GEM foil is 500 V. The drift lines of electrons are marked in yellow, while for the ions in brown. The processes of electrons with the gas mixture are shown by dots (brown for ionization and green for excitation) [26].

by foil and involves an increasing number of holes along the thickness of triple-GEM.

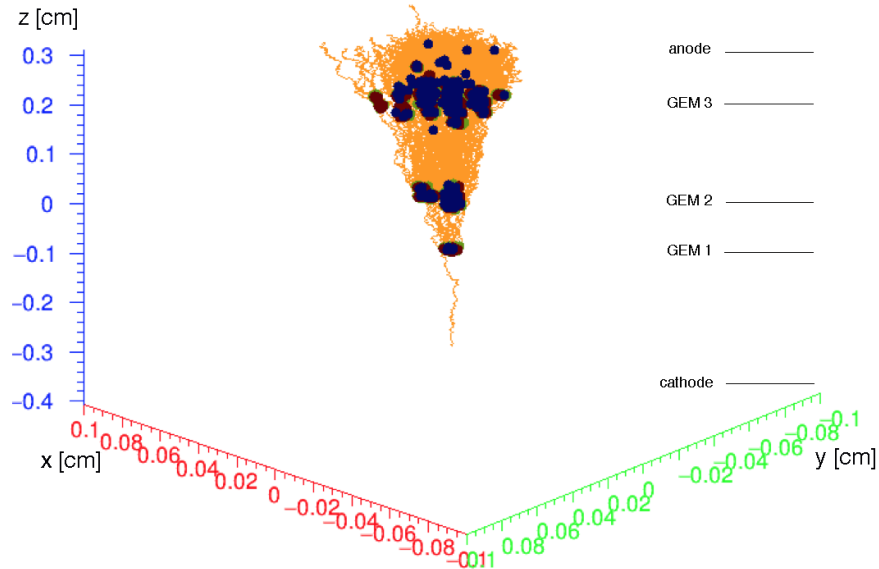


Figure 4.13: Simulation of an electron avalanche produced by a primary electron, placed in the drift region. Each GEM foil multiplies the number of incoming electrons, so the electron avalanche grows and involves a greater number of holes along the triple-GEM.

4.3 Choice of the gas mixture for triple-GEM

The choice of a proper gas mixture for a generic gaseous detector depends on several factors: allowed working voltage, good proportionality and energy resolution, high gain, high rate capability, time resolution, aging effects, etc.

Avalanche multiplication occurs in all gases, but for low working voltage operation, noble gases are usually chosen because they request the lowest electric field strength for avalanche formation. *Ar* is often used in the gas mixture because of its low cost. However the use of pure *Ar* as a filling gas cannot allow to achieve a gain greater than about 10^3 without occurring in continuous discharges. Indeed the excited noble gases return to the ground state only through radiative process: for *Ar* the minimum energy of emitted photon is 11.6 eV, which is above the ionization potential of several metals, constituting some parts of detectors. For instance, the copper, which has an ionization potential equal to 7.7 eV, is used in two layers to cover the inner part in Kapton in common GEM foil. Therefore photons, emitted by de-excitation of *Ar* atoms, can extract photoelectrons from copper and generate avalanche just after the ones produced by first electrons in the gas volume.

For solving this problem and achieving higher gain, the addition of a polyatomic gas is necessary. Polyatomic molecules, such as CO_2 , CF_4 , freons, CH_4 and others, can absorb photons in a wide energy range. This type of gases, called quencher gases, presents non-radiative excited states (rotational and vibrational) that allows the dissipation of absorbed energy by dissociation or elastic collisions. A proper concentration of a quencher gas in the mixture allows achieving high gains (up to 10^5 - 10^6) before discharges [8]. The quenching efficiency of a polyatomic gas increases generally with the number of atoms in the molecule. For triple-GEM detector usually the CO_2 is used as quencher gas.

The addition of small quantities of electro-negative gases, like freons, SF_6 , CF_4 , allows reaching saturated mode of operation. Indeed electro-negative gases can capture free electrons, by electron capture, in order to avoid the induction of further avalanches in the gas volume.

Several gas mixtures are currently used for different gaseous detectors. In this simulation the gas mixtures used for the triple-GEM at GIF++ have been considered.

The charge multiplication factor (or gas gain) of specific gas mixtures has been evaluated through the simulation of the first Townsend coefficient in a gas volume with uniform electric field. Figure 4.14 shows the first Townsend coefficient for a mixture

of pure Ar , Ar/CO_2 (70/30) and $Ar/CO_2/CF_4$ (45/15/40). When the mixture is pure Ar , the Townsend coefficient is much higher at low values of electric field in comparison to other two mixtures. The addition of a quencher gas, as CO_2 , decreases the Townsend coefficient, lowering the gas gain but making possible to achieve higher gain without permanent discharges in the detector. Since CF_4 is an electro-negative gas, the addition of it in the mixture decreases further the Townsend coefficient; so a higher electric field is needed to have the same performance in the triple-GEM with Ar/CO_2 (70/30) and $Ar/CO_2/CF_4$ (45/15/40). This is the reason why the working voltage of triple-GEM with Ar/CO_2 (70/30) is -3500 V , whereas it is -4500 V with $Ar/CO_2/CF_4$ (45/15/40): the two values have been evaluated in previous studies [21]. In any case, the addition of CF_4 in the gas mixture increases the time resolution of detector, as will be seen later.

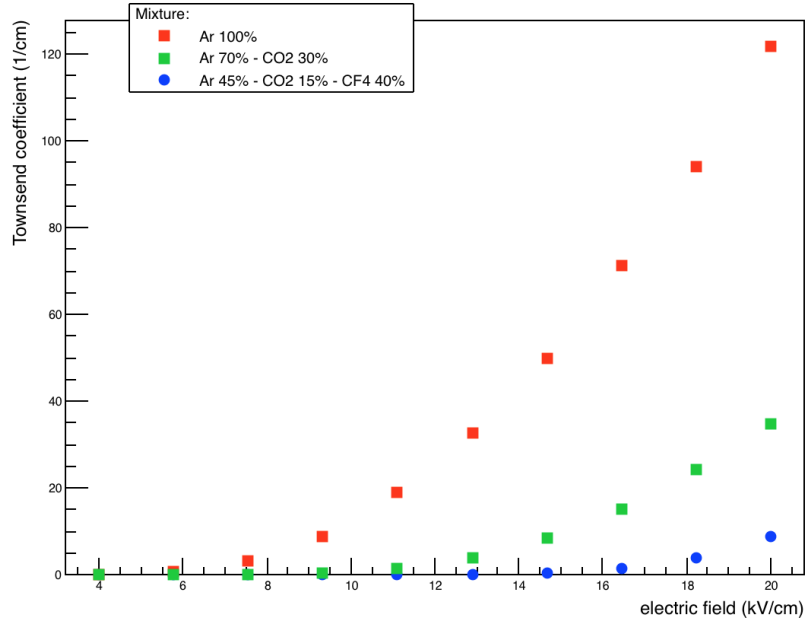


Figure 4.14: The first Townsend coefficient as function of electric field for a mixture of pure Ar , Ar/CO_2 (70/30) and $Ar/CO_2/CF_4$ (45/15/40). The simulation has been done with GARFIELD in a gas volume where the electric field is uniform.

As shown in figure 4.15, the addition of CO_2 and CF_4 decreases the multiplication factor of gas mixture, but the drift velocity of electrons for the triple-GEM is improved.

Usually the CF_4 is used in the GEM detectors for increasing the time resolution; indeed in Ar/CO_2 mixture, the time resolution of usual triple-GEM detectors is about

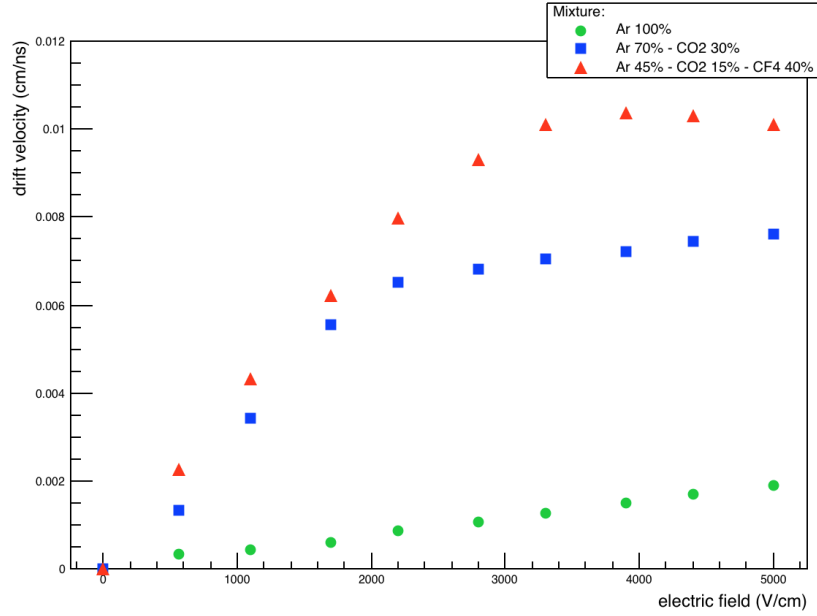


Figure 4.15: Drift velocity of electrons as function of electric field with different gas mixtures. The addition of CO_2 and CF_4 increases the drift velocity of electrons in the gas volume.

10 ns, but it becomes lower than 5 ns with the addition of CF_4 . However the use of CF_4 requires special precautions, because the reactivity of fluorine with H_2O can generate hydrofluoric acid (HF). This acid is corrosive for the GEM foil. Figure 4.16 shows a microscopic view of holes in a triple-GEM before and after the etching induced by hydrofluoric acid.

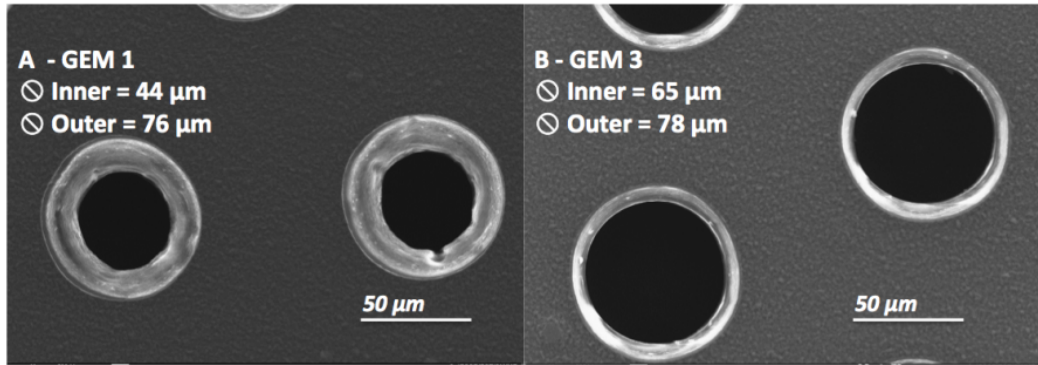


Figure 4.16: Microscopic view of holes in a triple-GEM before and after the etching induced by hydrofluoric acid, very corrosive for many materials [27].

4.4 Effects of pollutants in the gas mixture

The presence of pollutants in the gas mixture could affect the operation of gaseous detectors depending on the type of gas and concentration. Major effects concerning the gas mixture are the modification of transport parameters and the increasing of electron attachment due to the presence of pollutants with electronic affinity. Indeed the molecules of some gases capture the electron during the collision, forming heavy negative ions.

The basic processes are:

- Dissociative capture: $AB + e \rightarrow A^- + B$, so a molecule made up of two atoms (A and B) captures an electron (e) and dissociates in an ion and in an atom.
- Non-dissociative capture: $AB + e \rightarrow AB^-$, so a molecule captures an electron without dissociation.

Most of the gases attach electrons by both processes, depending on the electron energy. The number of surviving electrons after a drift length s is:

$$n = n_0 e^{-h \frac{eE}{mv^2} s} \quad (4.1)$$

where n_0 is the number of electron before drifting, h is the probability of attachment per collision, e the elementary charge, m the electron mass, v the drift velocity and E the electric field.

Previous studies, carried out in laboratory on the same triple-GEM detector under test at GIF++, have demonstrated that the gain decreases (by keeping constant the high voltage) when the recirculation fraction of gas mixture increases [21].

Figure 4.17 shows the normalized gain of the triple-GEM as a function of integrated charge in different operation periods. If the recirculation fraction is set to 50%, the detector gain is almost the same of open mode operation: this can be explained by the low quantities of impurities present with a low recirculation fraction. The decreasing of gain depends on the recirculation fraction and the integrated charge (4.5 mC/cm^2) can be considered too low to see any possible ageing effects.

Indeed when the recirculation fraction increases, the concentrations of some pollutants increase as well. Common pollutants in the gas system are air or gas products

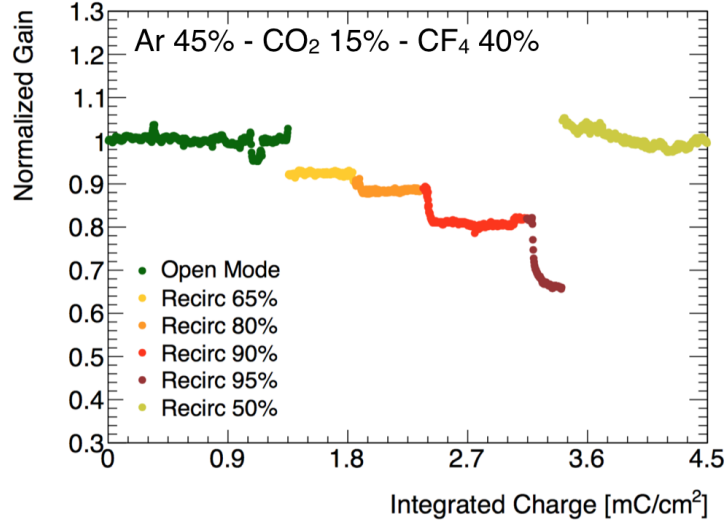


Figure 4.17: Normalized gain of the triple-GEM as function of integrated charge when the gas mixture is $Ar/CO_2/CF_4$ (45/15/40). The gain decreases if the recirculation fraction goes up [21].

created from molecule dissociation. Figure 4.18 shows the normalized gain of triple-GEM in $Ar/CO_2/CF_4$ (45/15/40) and the concentration of N_2 , O_2 and H_2O vapour at different recirculation fraction. When the GEM detector is in open mode, the gas mixture presents of course contamination of N_2 , due to the permeability of detector frame, and some pollutants due to leaks and gas supply quality. As shown in figure 4.17, the concentrations of each pollutants increase at higher recirculation fraction.

A simulation with GARFIELD software has been performed to understand the influence of each pollutant on the multiplication factor of triple-GEM.

As shown in figure 4.18, the gain of triple-GEM decreases when the recirculation fraction goes up due to the increasing of pollutants in the gas mixture. To reproduce the GEM performance obtained in the laboratory, the multiplication factor of triple-GEM has been simulated in the gas mixture $Ar/CO_2/CF_4$ (45/15/40) and then compared to the experimental measurements of gain. For the simulation, the concentrations of pollutants shown in figure 4.18 have been taken into account and the relative ratios among Ar , CO_2 and CF_4 are assumed constant. Moreover 10000 primary electrons, which generate potentially an electron avalanche up to anode, are simulated for each recirculation fraction. The assumptions for primary electrons are:

- to be placed into the drift region (in particular, from $z = -0.3$ cm to $z = -0.2$ cm);

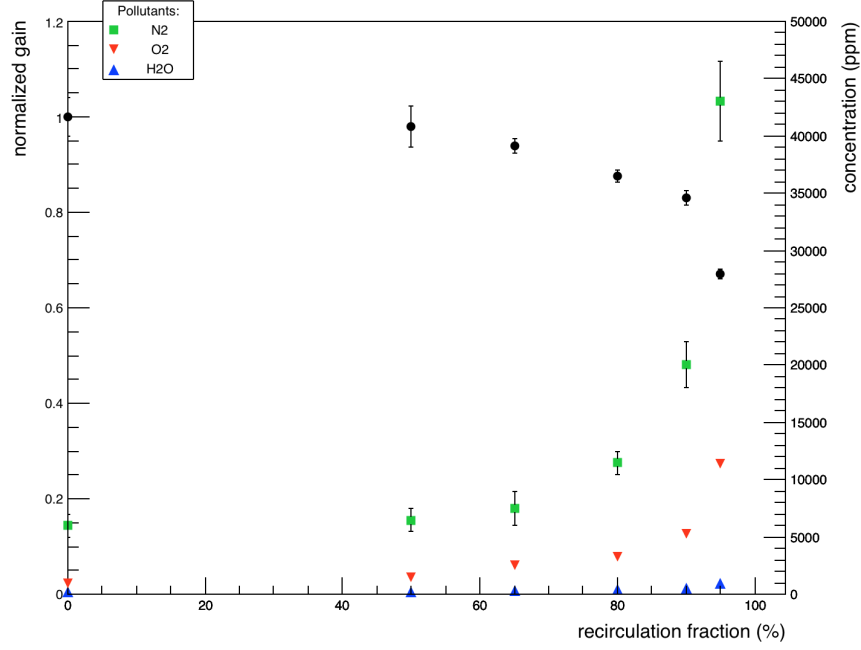


Figure 4.18: Normalized gain of triple-GEM in $Ar/CO_2/CF_4$ (45/15/40) and the concentration of N_2 , O_2 and H_2O vapour at different recirculation fractions. The black dots indicate the normalized gain of GEM detector. Markers cover some error bars, especially for concentration of O_2 and H_2O vapour [21].

- to have a random initial energy between 0.01 eV and 0.5 eV;
- to have a random initial direction.

The multiplication factor is calculated as the number of primary electrons, which originate an avalanche up to anode, in the 10000 simulated events. For instance, in open mode (i.e. with low impurities concentration) the number of primary electrons, which originate an avalanche up to anode, is 7851 over 10000 simulated events while at 80% as recirculation fraction the primary electrons are 7192. The simulation has been repeated ten times for each recirculation fraction.

Figure 4.19 shows the multiplication factor, which is normalized respect to the value at 0% as recirculation fraction, and the normalized gain, directly measured in laboratory: there is a good agreement between the direct measurements and the results of simulation.

In table 4.2 the values of normalized gain and multiplication factor are shown.

So it is possible to compute the expected gain of the triple-GEM in presence of pollutants (N_2 , O_2 and H_2O vapour) by simulation with a good approximation.

The simulation has been repeated by removing one type of pollutant per time. In

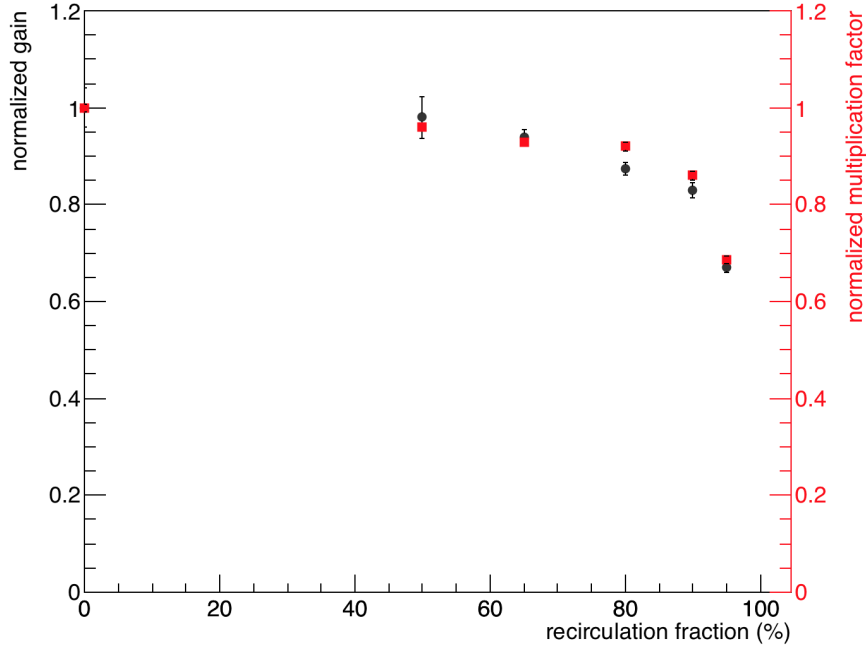


Figure 4.19: Normalized gain (in black) and the normalized multiplication factor (in red) depending on the recirculation fraction. There is a good agreement between the direct measurements on the triple-GEM and the results of simulation.

recirculation fraction	normalized gain	normalized multiplication factor	z-test
0%	1.00 ± 0.04	1.000 ± 0.008	0
50%	0.98 ± 0.04	0.961 ± 0.006	0.5
65%	0.94 ± 0.02	0.930 ± 0.003	0.5
80%	0.889 ± 0.014	0.92 ± 0.01	1.8
90%	0.83 ± 0.02	0.86 ± 0.01	1.3
95%	0.67 ± 0.01	0.685 ± 0.008	1.2

Table 4.2: Normalized gain, measured in laboratory, and normalized multiplication factor, simulated with GARFIELD.

this case, it is possible to verify if the decreasing of the gain is due to one specific pollutant or depends on the mix of the three pollutants taken into account.

The suppression of O_2 in the simulation induces a normalized multiplication factor almost equal to 1 at every recirculation fractions. Figure 4.20 shows the normalized multiplication factor when the three pollutants are present in the gas mixture and when the O_2 is removed. For every recirculation fraction, the ratios among Ar , CO_2 and CF_4 have been kept constant, the concentrations of N_2 and H_2O are the same measured in laboratory (figure 4.18), while the O_2 is removed.

As shown in figure 4.20, the O_2 presence has a high impact on the gain of triple-GEM. Figure 4.21 shows the attachment coefficient per drift unit when the gas mixture is

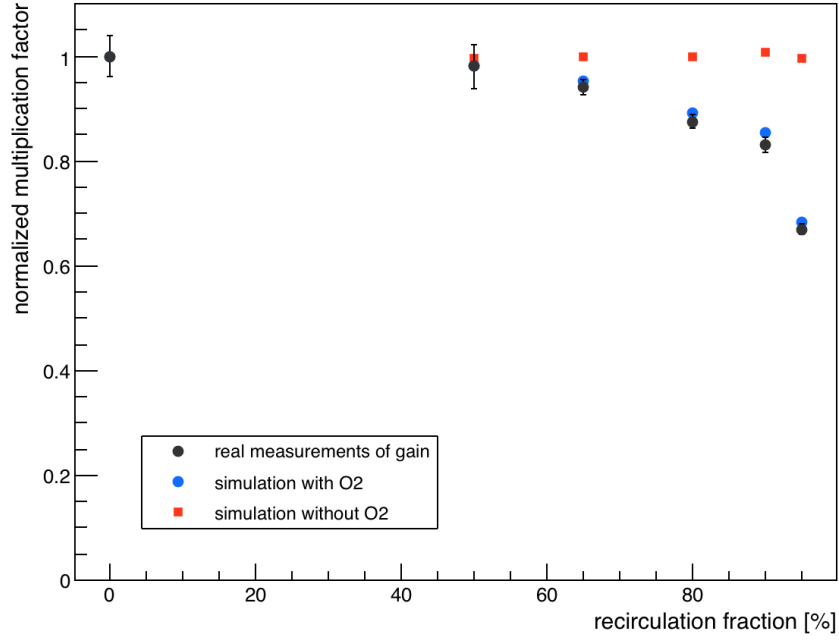


Figure 4.20: Normalized multiplication factor depending on recirculation fraction when the three pollutants are present in the gas mixture and the O_2 is removed. When it is not removed, the concentrations of O_2 , taken into account in the simulation, are shown in figure 4.18: 980 ppm at 0% as recirculation fraction, 1540 ppm at 50%, 2490 ppm at 65%, 3250 ppm at 80%, 5300 ppm at 90% and 11400 ppm at 95%. The markers hide some error bars in the plot.

pure and when it is contaminated by 1% O_2 . Contaminants of O_2 in the gas mixture make greater the attachment coefficient of mixture. Especially at low electric field, the effect of electron capture by O_2 is larger.

The H_2O vapour has the same qualitative effect of the O_2 as well. During measurements in the laboratory, the concentration of H_2O vapour has been really low in comparison to O_2 , so the decreasing of GEM gain due to H_2O vapour is not evident. The effects of O_2 and H_2O vapour are well-known through several studies on gaseous detector mixtures; indeed they are electronegative gases as well as CO_2 , SF_6 , CF_4 . The presence of electronegative gases diminishes severely the electron-ion collection by trapping the electrons before reaching the anode [28, 29, 30].

The effect of N_2 as pollutant is different from effects of O_2 and H_2O vapour: N_2 induces the modification of transport parameters of gas mixture. A dedicated study with different N_2 concentrations has been conducted in a gas mixture of Ar/CO_2 (70/30), where the contamination of this type of gas has the major effects. The drift velocity in Ar/CO_2 (70/30) changes with addition of different N_2 concentrations, as

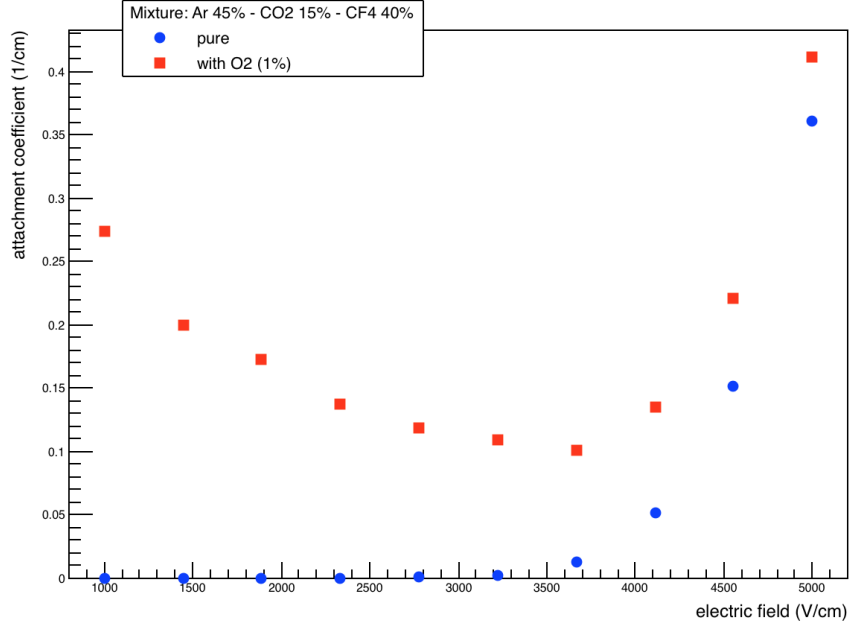


Figure 4.21: Attachment coefficient per drift unit when the gas mixture is pure and contaminated by 1% of O_2 . Effects of electron capture by O_2 are larger at low electric field.

shown in figure 4.22.

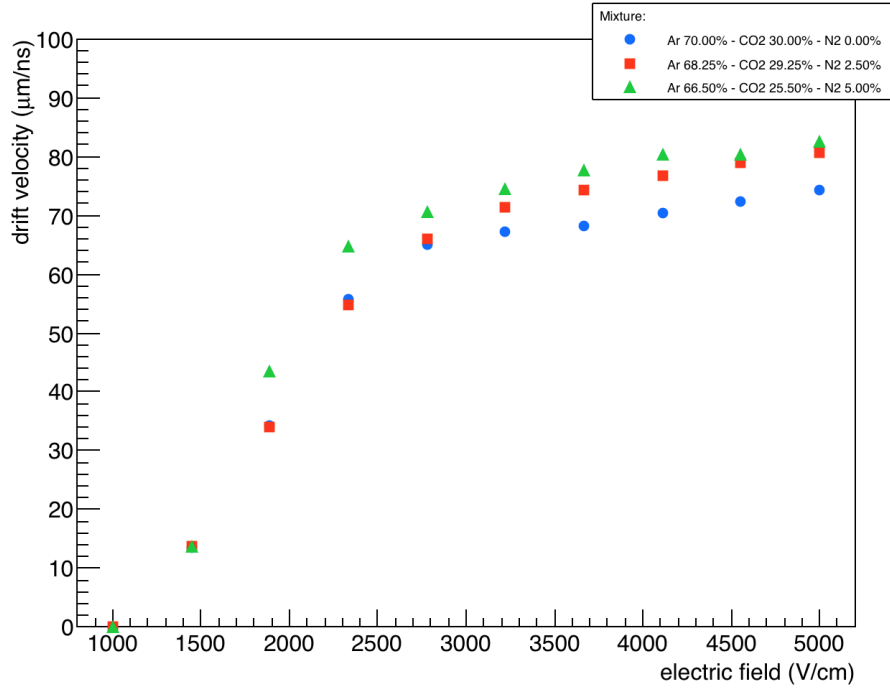


Figure 4.22: The drift velocity in 70% Ar and 30% CO_2 is modified by small concentration of N_2

For the studies of triple-GEM, the simulation might represent a powerful tool to repro-

duce possible effects of pollutants during the tests at GIF++. Indeed the availability of simulation could permit to calculate extensively drift and diffusion properties in presence of pollutants. The characterization and optimization of the recirculation system allows finding a proper recirculation fraction, where the concentrations of pollutants do not affect the performance of triple-GEM so much.

Conclusions

In view of the High-Luminosity LHC upgrade program, the increase of background radiation could affect the gaseous detector performance, as for example in terms of efficiency and ageing processes. The ageing effects on charge multiplication, materials and gas composition in gaseous detectors have been studied for decades, but the future upgrade of LHC will require additional studies on this topic.

The CERN Gamma Irradiation Facility (GIF++) has been built to study the performance of gaseous detectors, exposed to a high radiation environment, as well as to carry out ageing tests to validate the long-term detector operation. Indeed at GIF++, a radioactive source of ^{137}Cs with activity of 14 TBq is used to reproduce in good approximation the expected background radiation at HL-LHC, whereas a muon beam has been made available to study detector performance.

The first part of the work, presented in this thesis, presents the characterization and the installation of the GIF++ beam trigger system, based on scintillators coupled with photomultipliers. The trigger allows the detection of the muon beam passing through the facility. The data acquisition system, based on NIM standard, provides the trigger signal to the users during the beam periods dedicated to GIF++. The beam trigger has been made available to the users during 2016.

In the second part of the present work, R&D studies have been performed to investigate the performance of a triple gas electron multiplier (triple-GEM detector) under gas recirculation in presence of high background radiation at GIF++.

The gas mixture is monitored by two single wire proportional chambers (SWPCs), which give an instantaneous feedback of the gas quality thanks to their high sensitivity.

Before the test at GIF++, a characterization of triple-GEM detector and SWPCs has been carried out in laboratory. In particular the performance of SWPCs was monitored for about one month in the laboratory to validate their stability. The

triple-GEM detector has been characterized in Ar/CO_2 (70/30) and a source scan on the surface was performed to evaluate the uniformity of response.

For the test at GIF++, a custom-made DAQ software has been developed and implemented to control high voltages, monitor environmental conditions of the facility and analyse the data from detectors and others monitoring devices. In addition a gas chromatograph, available at GIF++, has been calibrated and tuned for having the possibility to analyse the gas mixture composition.

The GEM detector under test at GIF++ is irradiated with two radioactive sources: the ^{137}Cs is used for the ageing of triple-GEM, while the irradiation with ^{55}Fe allows monitoring detector performance, thanks to the well-defined peak in the pulse-height distribution. The procedure of test at GIF++ has been validated for the long-term operation.

In the last part of the present work, a simulation of the triple-GEM detector has been carried out with ANSYS and GARFIELD++. The simulation is focused on the understanding of drift and diffusion of electrons in two different gas mixtures (Ar/CO_2 and $Ar/CO_2/CF_4$) under the effect of triple-GEM electric field. Moreover the simulation has been performed in order to understand the contribution of typical pollutants in the gas mixture and compute triple-GEM performance for different concentrations of them. The simulation results are in agreement with experimental measurements. For the studies of triple-GEM, the simulation might represent a powerful tool to reproduce possible effects of pollutants during the tests at GIF++.

Appendix A

Experimental setup at Gamma Irradiation Facility in details

Mass flow controllers (MFCs): working principle

The MFCs are usually made up of a turbulent filter, a laminar flow element, a thermal mass flow sensor and a control valve. The gas, which enters from the inlet, goes through the turbulent filter and then through a laminar flow element: they consist of a series of thin layers with some openings to convert the turbulent flow in input into a laminar flow. The impedance of these elements ensures that the gas goes also into a mass flow sensor. The sensor consists of a capillary tube with a heater, placed between two temperature sensors at the same distance from it (figure A.1).

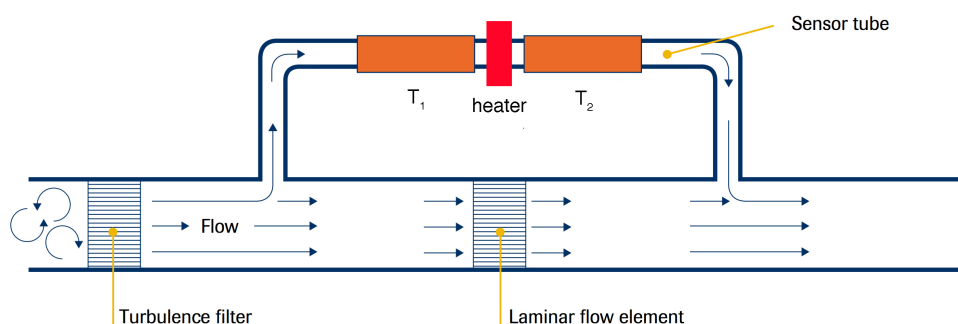


Figure A.1: Schematic view of a mass flow controller (MFC).

If there is no flow in the capillary, the heater warms the tube and the two temperature sensors heat up evenly. In case a gas flow is present in the capillary, the temperature sensor (T_1) before the heater measures a lower temperature in comparison to the second one (T_2), placed after the heater. The temperature difference results to be a direct measurement of the mass flow of the gas. Depending on the temperature

difference measured, a valve is open or close to control the gas flow in the output of the device.

Purifier module

The purifier module under study at GIF++ hosts three cartridges, as shown in figure A.2.

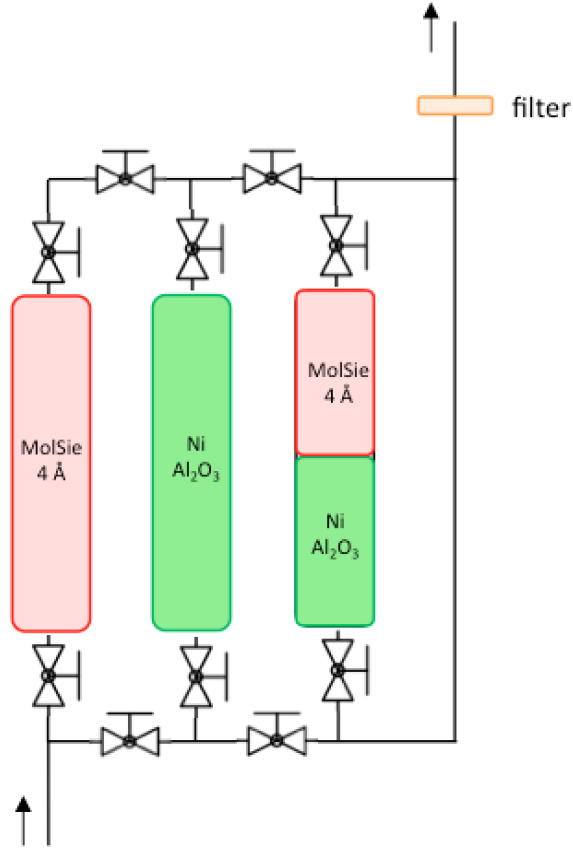


Figure A.2: Purifier module under test at the GIF++, which hosts three independent cartridges: the first one is filled by a molecular sieve 4 Å, the second one is made up of Ni onto a substrate of aluminium oxide (Al_2O_3) and the last one is filled half with a molecular sieve 4 Å and the remaining half with $Ni + Al_2O_3$. A system of valves allows using each line independently. At the end of the purifier, a filter is placed to avoid the release of impurity from the cartridges.

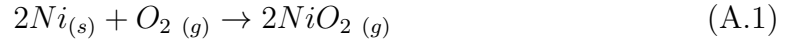
The first cartridge is filled with molecular sieve of 4 Å, the second one is made up of nickel (Ni) onto a substrate of aluminium oxide (Al_2O_3) and the last one is filled half with the molecular sieve of 4 Å and the remaining half with $Ni + Al_2O_3$.

The molecular sieve is a zeolite, provided by the company Zeochem, with pores of uniform size (in this case, the diameter is about 4 \AA). This cartridge is used to absorb H_2O vapour from the gas mixture. In table A.1 the nominal absorption capacity is summarised, depending on the diameters of the pores:

Type	MolSieve 3 \AA	MolSieve 4 \AA	MolSieve 5 \AA
Main component filtered	H_2O	H_2O	H_2O
Diameter of pores	3 \AA	4 \AA	5 \AA
Absorption capacity $[g(H_2O)/kg]$	140	170	130

Table A.1: Nominal absorption capacity depending on different molecular sieve, based on zeolite [21].

The absorber of 4 \AA has been selected for the higher nominal absorption capacity. The second type of absorber acts through chemical reactions with O_2 :



The regeneration is done heating at $220 \text{ }^\circ\text{C}$ for 150 minutes under a constant flow of H_2 .

The purifier system has a complex system of valves in order to have the possibility to use or exclude each line independently by other. This system is really useful when the effects of the saturation of cartridges begin to appear and their regeneration becomes necessary. In the R&D studies at GIF++, the cartridges with a single absorber are used for the purification of the gas mixture, whereas the other type of cartridge is kept as spare. When the regeneration of cartridge becomes needed, the gas mixture is just led into the spare one and the saturated cartridges can be regenerated without any interruption of the test. At the end of the purifier, a filter has been placed to avoid possible release of dust from the cartridges.

Appendix B

Construction and characterization of SWPCs

The configuration of SWPCs at GIF++ foresees a large drift region in order to optimize the sensibility to the pollutants; indeed they acts especially in this region by electron capture, dissociative processes and so on.

The main structural component of a SWPC is in stainless steel 316L. The wire, stretched along the axis of the cylinder, has a $25\ \mu m$ diameter and is in gold-plated tungsten. The order of magnitude of voltage between the external structure and the wire is $10^3\ V$ (a proper characterization has been carried out and is shown in chapter 3). The main structure and the wire are insulated with a high voltage feedthrough in borosilicate glass. The glass caps have a pipe inside in nickel-cobalt alloy pipe, which has a thermal expansion similar to the borosilicate glass, in order to get an optimal mechanical connection. The wire is stretched and fixed by clamping two pins at the extremities. A deposition of epoxy glue (ARALDITE AW 106 Resin with hardener HV953U) around the pins avoids the release of the gas mixture. Both windows of the main structure are covered with aluminium foils and gaskets, optimized for the edges of the main structure. The gas mixture is injected into a side and is evacuated in the diagonally opposite one to avoid regions of stagnation. Figure B.1 shows a picture of a SWPC, built for the experimental setup at GIF++.

For the construction and assembling of the chambers, it is necessary to clean every component and operate in a clean room to avoid deposition of impurities on the surfaces. An ultrasonic washer was used for the cleaning of detector components with an appropriate solvent, based on alcohol, and then rinsed with demineralized water, to avoid presence of inorganic components in the detector. Figure B.2 shows the components, after the washing of surfaces, in the clean room.

For checking the performance of the SWPCs, they are irradiated with radioactive



Figure B.1: Picture of a SWPC built for the experimental setup at GIF++. In the photo, you can see the main structure of the SWPC, the gold-plated tungsten wire and the pins, which will be fixed to the wire by clamping.



Figure B.2: Components of the SWPCs in the clean room.

sources of ^{55}Fe , which have a round shape of 2 *cm* diameter. The radioactive source can be placed in five different positions in order to have the possibility to irradiate the detector along the total wire length (figure B.3).

One extremity of the wire is plugged to a custom-made electric circuit, as shown in figure B.4.

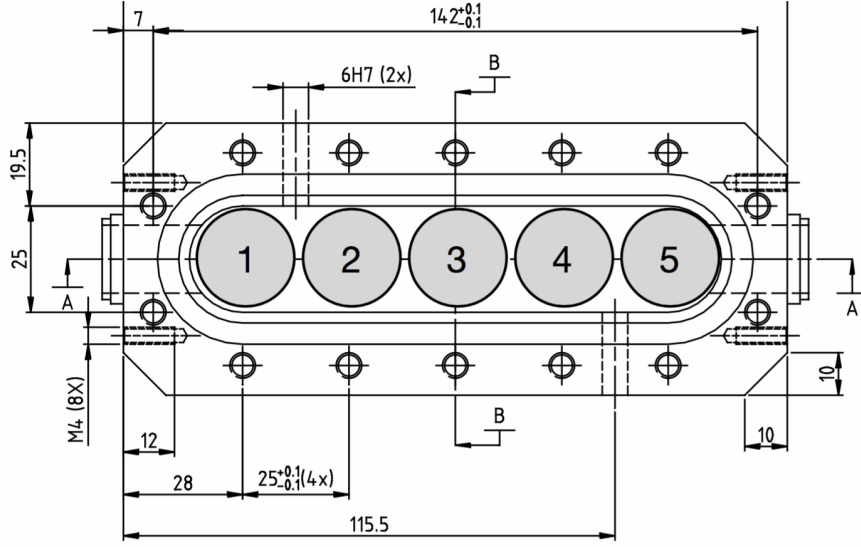


Figure B.3: Technical drawing of the SWPCs, assembled for the experimental set-up at GIF++. Five different positions along the wire length, where the radioactive source may be placed, are shown: position 1 is close to the HV module. The total dimensions of the detector are: 20 cm x 6.5 x 5 cm.

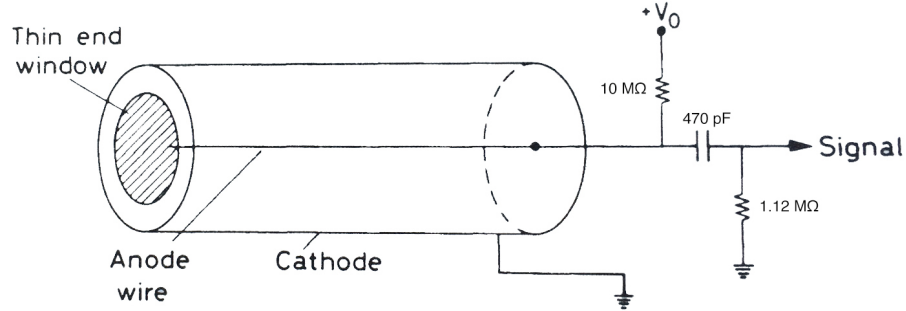


Figure B.4: Sketch of a SWPC with the electric circuit, used to apply the high voltage and take the signal.

After the construction, the SWPCs has been installed in the laboratory for the characterization, as shown in figure B.5.

Figure B.6 shows the gain (expressed in ADC counts) of SWPC1 and SWPC2, depending on the applied voltage on the wire. The main peak in the pulse-height distribution has been fitted by a Gaussian function. The mean value of the fit is direct proportional to the gain of detector, while the standard deviation (Gaussian RMS width) has been assumed as resolution of the gain. The SWPC1 at 1850 V has a similar gain of the SWPC2 at 2025V: these settings will be used for the measurements in this thesis.



Figure B.5: Experimental set-up for the characterization of the SWPCs in the laboratory. In this picture, the radioactive source of ^{55}Fe are placed in the middle of aluminium window (position 3). For convention, the position 1 is close to the HV module. The experimental conditions are specified in chapter 3.

After evaluating the working points for the SWPCs, the uniformity of the electrical field was verified along the wire. Figure B.7 shows the measurements of the gain along the wire for SWPC1 and SWPC2. The data have been taken moving the radioactive source along the length of detectors. In the extremities of detector (in positions 1 and 5, according to notation in figure B.3), the presence of the glass feedthrough deforms the electric field so much that the incoming photons are not detected. The gain of SWPCs can be assumed uniform from the position 2 to the position 4.

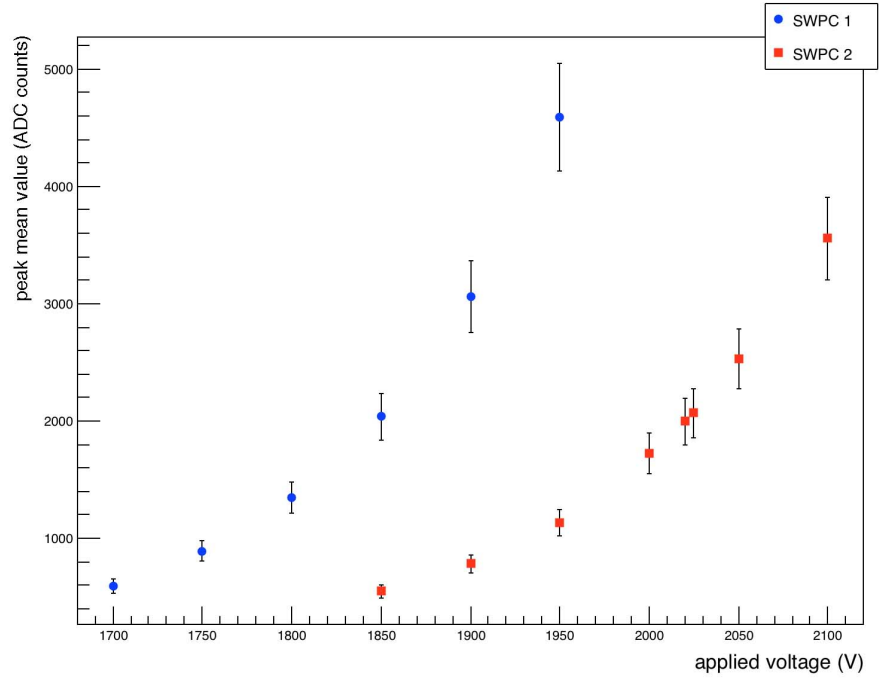


Figure B.6: Gain of SWPC1 and SWPC2 depending on applied voltage on the wire. The SWPCs have similar gain at 1850 V and 2025 V, respectively. The ^{55}Fe sources were placed in the middle of detector length (position 3).

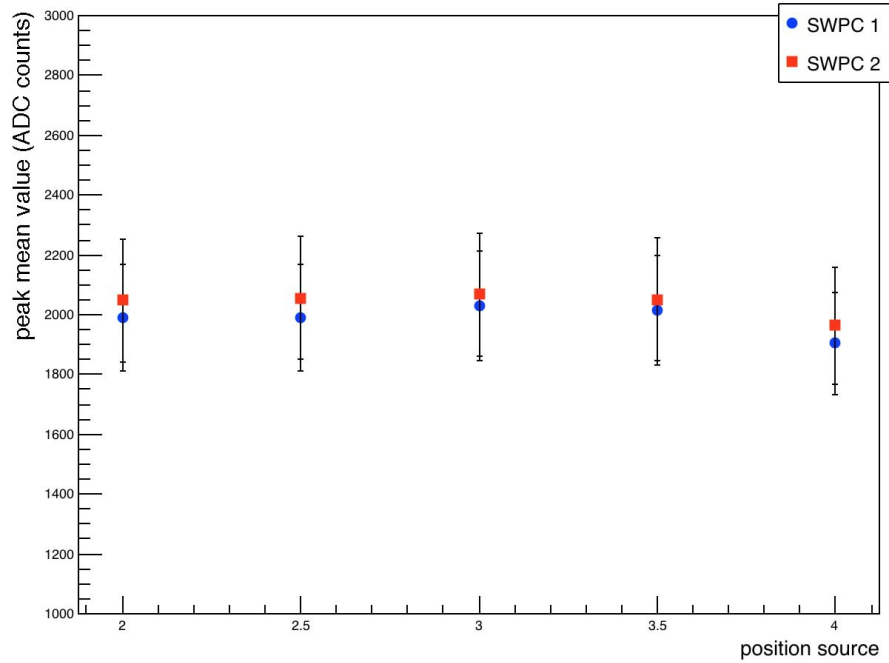


Figure B.7: Mean value of ^{55}Fe peak and argon escape peak along the wire for the SWPC1 and SWPC2 (according to the notation in figure B.3).

Appendix C

Gas chromatography

Gas chromatograph: working principle

The gas chromatography is a technique to separate gas mixture into individual components and measure their concentrations. The gas chromatograph is generally made of several columns coupled with injectors and thermal conductivity detectors (TCD). The gas chromatograph, used at GIF++, is the 3000 Micro Gas Chromatograph, provided by SRA Instruments.

The separation of the mixture occurs in the column; indeed some component results separated in time from the others at the end of column, due to the different reaction with the materials inside. Different types of columns are available, but in general they can be divided in capillary and packed. The choice of them depends on the nature of gas mixture and the desired information, since the columns contain different materials, which can retard only some components. The columns available in the device at GIF++ are:

- MolSieve (MS): 5 Å zeolite molecular sieve, which can separate air and noble gases;
- PPlotU (PPU): Porous Layer Open Tubular column, which can separate hydrocarbons from C_1 to C_4 , CO_2 , CH_4 , SO_2 , N_2O and so on.

The lengths of the column are really important to get a good separation in time. For both columns in the gas chromatograph at GIF++ the length is equal to 8 m.

After the physical separation in time of each component, a TCD device is present at the end of the column, resulting in a chromatogram, where each peak represents a different component of the original sample. Indeed the TCD device, through the

different thermal conductivity of gases, produces a precise electrical signal, which is proportional to the amount of analyte.

Tuning of gas chromatograph with air sample

Before chromatography on the gas mixture from the detectors, several measurements of air have been carried out to optimize a good separation in time of the components of interest. Figure C.1 shows the different retention time of O_2 and N_2 depending on the temperature of the MolSieve column, whereas figure C.2 shows two different gas chromatograms when the temperature is set to $30\text{ }^{\circ}\text{C}$ and $115\text{ }^{\circ}\text{C}$. For every measurements, the temperature of the injection into the column is always equal to $65\text{ }^{\circ}\text{C}$.

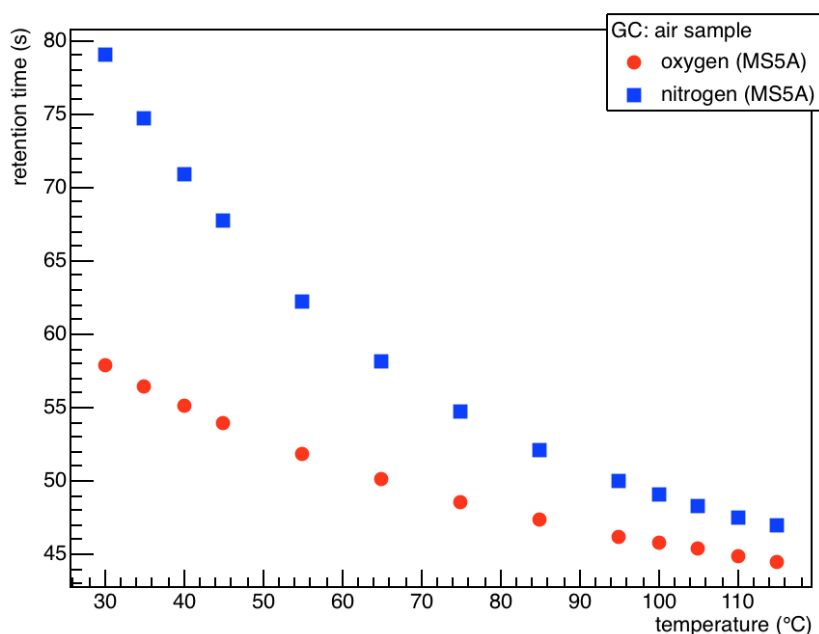


Figure C.1: Retention time of O_2 and N_2 depending on temperature in MolSieve column. The time retention of each component goes up when the temperature of the column is decreased.

For the MolSieve column, it has been decided to set the temperature equal to $115\text{ }^{\circ}\text{C}$ for the column and then proceed with the calibration of O_2 and N_2 with pre-mixed gas bottles: 100 ppm of O_2 and 400 ppm of N_2 in Ar . Several analyses for the same sample are essential in order to have reliable measurements of concentrations. Indeed first chromatograms present significant differences in the retention time and in the

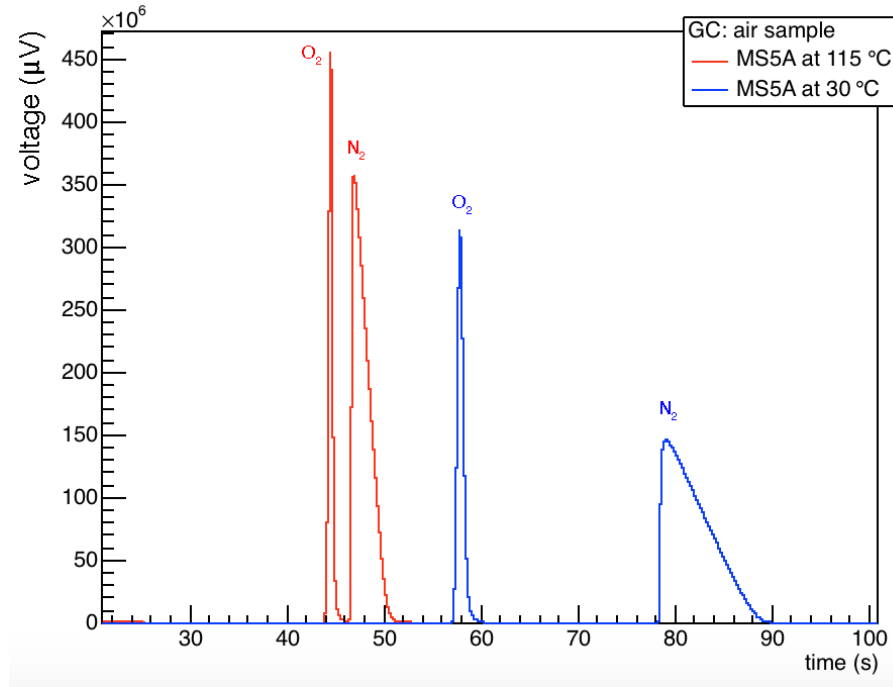


Figure C.2: Two gas chromatograms of air sample are acquired at different temperatures of the column.

area of each peak, because TDC devices need to stabilize. Only after about 20 runs, the gas chromatograph gives correct measurements of concentrations.

Concerning the PPU column, the temperature has been selected to 75 °C in order to discriminate Ar and CO_2 in the gas mixture. Figure C.3 shows the peak of CO_2 in air (about 400 ppm) when the PPU column is at 75 °C.

The calibration for only CO_2 has been only done for CO_2 with a pre-mixed gas bottle (30% of CO_2 in Ar). Concerning the Ar , which is separated in the PPU column, proper measurements of the concentration cannot be carried out, because the concentration is so high that the response of device is not reliable. Indeed the company SRA, which made the gas chromatograph, ensures a proportional response of TCD devices in the range from a few tens of ppm to 50%.

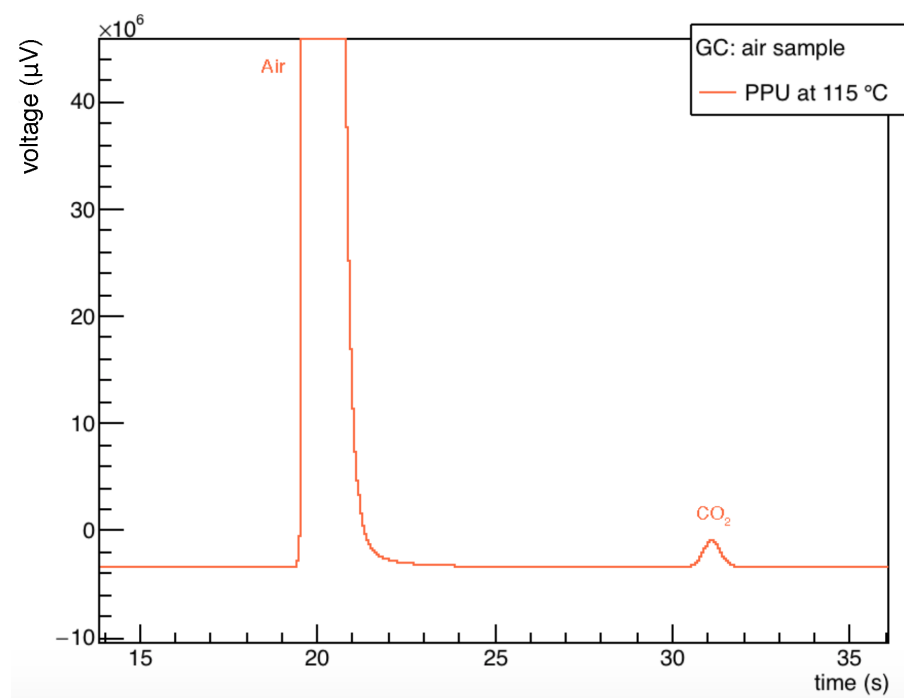


Figure C.3: Gas chromatograph with PPU column at 75 °C. The figure shows the peak of CO_2 in air (about 400 ppm).

Bibliography

- [1] S. Stapnes. Detector challenges at the LHC. *Nature*, 448(7151):290–296, 2007. 4
- [2] B. Schmidt. The High-Luminosity upgrade of the LHC: Physics and Technology Challenges for the Accelerator and the Experiments. *Journal of Physics: Conference Series*, 706(2):022002, 2016. 4
- [3] L. Massa. Proposal of upgrade of the ATLAS muon trigger in the barrel-endcap transition region with RPCs. Technical Report ATL-MUON-PROC-2014-003, CERN, Geneva, Jun 2014. 5, 6
- [4] R. Guida. GIF++: The new CERN Irradiation Facility to Test Large-Area Detectors for HL-LHC. *CERN Detector Seminar*, 2015. 6, 10, 12
- [5] P. Vankov and ATLAS Collaboration. ATLAS Future Upgrade. Technical Report ATL-UPGRADE-PROC-2016-003, CERN, Geneva, Jun 2016. 7
- [6] D. Abbaneo et al. Characterization of GEM Detectors for Application in the CMS Muon Detection System. In *Proceedings, 2010 IEEE Nuclear Science Symposium and Medical Imaging Conference (NSS/MIC 2010): Knoxville, Tennessee, October 30-November 6, 2010*, pages 1416–1422, 2010. 7
- [7] A. Colaleo, A. Safonov, A. Sharma, and M. Tytgat. CMS Technical Design Report for the Muon Endcap GEM Upgrade. Technical Report CERN-LHCC-2015-012. CMS-TDR-013, Jun 2015. 7
- [8] F. Sauli. *Gaseous Radiation Detectors*. Cambridge University Press, Cambridge, 2014. 8, 35, 38, 39, 43, 56, 60, 76, 81
- [9] M. R. Jakel, M. Capeans, I. Efthymiopoulos, A. Fabich, R. Guida, G. Maire, M. Moll, D. Pfeiffer, F. Ravotti, and H. Reithler. CERN GIF++: A new irradiation facility to test large-area particle detectors for the high-luminosity LHC program. *PoS, TIPP2014(AIDA-CONF-2014-018)*:102, 2014. 12, 13

- [10] G. Segura Millan, D. Perrin, L. Scibile. RAMSES: the LHC radiation monitoring system for the environment and safety. *10th ICALEPCS Conf. on Accelerator Large Expt. Physics Control Systems*, 2005. 14
- [11] F. Ravotti, M. Glaser, A. Rosenfeld, M. Lerch, A. Holmes Siedle, G. Sarraयरouse. Radiation Monitoring in Mixed Environments at CERN: From the IR-RAD6 Facility to the LHC Experiments. *IEEE transactions on nuclear science*, 54, 2007. 16
- [12] Super Proton Synchronotron. <https://home.cern/about/accelerators/super-proton-synchrotron>, 2016. [Online; accessed 30-September-2016]. 16
- [13] Super Proton Synchronotron Page-1. <https://op-webtools.web.cern.ch/Vistar/Doc/SPS1.pdf>, 2010. [Online; accessed 30-September-2016]. 16, 17
- [14] M. Capeans, R. Fortin, L. Linssen, M. Moll, C. Rembser. A GIF++ Gamma Irradiation Facility at the SPS H4 Beam Line. *Proposal to the CERN SPSC*, 2009. 16
- [15] CESAR interface for beam controls. <http://sba.web.cern.ch/sba/Documentations/How2controlNAbams.htm>, 2012. [Online; accessed 30-September-2016]. 17
- [16] Data distribution DIP and DIM. <https://wikis.web.cern.ch/wikis/display/EN/DIP+and+DIM>, 2013. [Online; accessed 30-September-2016]. 19
- [17] W. R. Leo. *Techniques for Nuclear and Particle Physics Experiments*. Springer-Verlag, Second Revised Edition, 1994. 23, 36, 56
- [18] CERN archive system TIMBER. https://espace.cern.ch/be-dep/C0/OBSOLETEDataManagementSection/doc/logging/TIMBER/user_guide.html, 2009. [Online; accessed 30-September-2016]. 26
- [19] A. C. Melissinos. *Experiments in modern physics*. WNew York: Academic Press, London, 1966. 36
- [20] Mass flow controllers by Bronkhorst. <http://www.bronkhorst.com/files/downloads/brochures/folder-el-flow.pdf>, 2016. [Online; accessed 30-September-2016]. 48

- [21] B. Mandelli, M. Capeans, R. Guida, O. Rohne, and S. Stapnes. *Detector and System Developments for LHC Detector Upgrades*. PhD thesis, Oslo U., Oslo, Norway, May 2015. Presented 12 May 2015. 52, 53, 71, 82, 84, 85, 86, 95
- [22] XCOM database by NIST. <https://www.nist.gov/pml/xcom-photon-cross-sections-database>, 2010. [Online; accessed 30-September-2016]. 55, 60, 61
- [23] M.C. Altunbas, K. Dehmelt, S. Kappler, B. Ketzer, L. Ropelewski, F. Sauli, and F. Simon. Aging measurements with the Gas Electron Multiplier (GEM) . *Nuclear Instruments and Methods in Physics Research Section A: Accelerators, Spectrometers, Detectors and Associated Equipment*, 515(12):249 – 254, 2003. Proceedings of the International Workshop on Aging Phenomena in Gaseous Detectors. 57
- [24] U. Renz. A TPC with Triple-GEM Gas Amplification and TimePix Readout. *LCTPC Collaboration*, 2009. 75
- [25] V. Palladino and B. Sadoulet. Application of classical theory of electrons in gases to drift proportional chambers. *Nuclear Instruments and Methods*, 128(2):323 – 335, 1975. 76
- [26] The RD51 Collaboration: Development of Micro-Pattern Gas Detectors Technologies. <https://ep-news.web.cern.ch/content/rd51-collaboration-development-micro-pattern-gas-detectors-technologies>, 2013. [Online; accessed 30-September-2016]. 80
- [27] J.A. Merlin, J. Brom, and A. Sharma. *Study of long-term sustained operation of gaseous detectors for the high rate environment in CMS*. PhD thesis, Strasbourg U., Apr 2016. Presented 25 Apr 2016. 83
- [28] L. B. O’Kelly, G. S . Hurst, T. E. Bortner. Measurement of electron attachment in oxygen-methan and oxygen carbon-dioxide mixture. *Internal publication of Oak Ridge National Laboratory*, 1960. 88
- [29] L. G. Christophorou. *Atomic and Molecular Radiation Physics*. Wiley, London, 1971. 88
- [30] N. E. Bradbury and F. Sauli. The formation of negative ions in gases (CO₂, N₂O, SO₂, H₂S). *J. Chem. Physics* 2, 835, 1934. 88

Acknowledgements

Ho avuto il piacere e la fortuna di poter svolgere questo lavoro di tesi al CERN. Durante questo periodo, ho certamente imparato molto, dalla fisica applicata all'ingegneria meccanica, ma soprattutto ho avuto l'opportunità di imparare che il CERN non è soltanto un laboratorio di fisica delle particelle. Il CERN è soprattutto Europa: è l'idea di Unione Europea che voglio. Sebbene tutto indichi il contrario, credo fortemente che la mia generazione debba impegnarsi a costruire e sforzarsi di portare avanti il progetto degli Stati Uniti d'Europa. Ho imparato che il CERN è un magnifico esempio e simbolo di questa unità europea; questa sarà sicuramente l'ispirazione principale che porterò con me.

Voglio ringraziare proprio qui e proprio ora Marco Aglietta, Akira Miyazaki, Pier Giorgio Panata, Maria Fabrizia Belletti, Ferruccio Balestra e i miei tutor e infine con umiltà e profonda gratitudine mio fratello e la mia famiglia.